Simulations of magnetized discs around black holes: Effects of black hole spin, disc thickness and magnetic field geometry

Permanent link

Share Your Story

Simulations of magnetized discs around black holes: effects of black hole spin, disc thickness and magnetic field geometry

Robert F. Penna,[1]★ Jonathan C. McKinney,[2]★† Ramesh Narayan,[1]★
Alexander Tchekhovskoy,[1]★ Rebecca Shafee[3]★ and Jeffrey E. McClintock[1]★

[1]*Harvard-Smithsonian Center for Astrophysics, 60 Garden Street, Cambridge, MA 02138, USA*
[2]*Department of Physics and Kavli Institute for Particle Astrophysics and Cosmology, Stanford University, Stanford, CA 94305-4060, USA*
[3]*Center for Brain Science, Harvard University, 52 Oxford Street, Cambridge, MA 02138, USA*

ABSTRACT

The standard general relativistic model of a razor-thin accretion disc around a black hole, developed by Novikov & Thorne (NT) in 1973, assumes the shear stress vanishes at the radius of the innermost stable circular orbit (ISCO) and that, outside the ISCO, the shear stress is produced by an effective turbulent viscosity. However, astrophysical accretion discs are not razor thin; it is uncertain whether the shear stress necessarily vanishes at the ISCO, and the magnetic field, which is thought to drive turbulence in discs, may contain large-scale structures that do not behave like a simple local scalar viscosity. We describe 3D general relativistic magnetohydrodynamic simulations of accretion discs around black holes with a range of spin parameters, and we use the simulations to assess the validity of the NT model. Our fiducial initial magnetic field consists of multiple (alternating polarity) poloidal field loops whose shape is roughly isotropic in the disc in order to match the isotropic turbulence expected in the poloidal plane. For a thin disc with an aspect ratio $|h/r| \sim 0.07$ around a non-spinning black hole, we find a decrease in the accreted specific angular momentum of 2.9 per cent relative to the NT model and an excess luminosity from inside the ISCO of 3.5 per cent. The deviations in the case of spinning black holes are also of the same order. In addition, the deviations decrease with decreasing $|h/r|$. We therefore conclude that magnetized thin accretion discs in X-ray binaries in the thermal/high-soft spectral state ought to be well described by the NT model, especially at luminosities below 30 per cent of Eddington where we expect a very small disc thickness $|h/r| \lesssim 0.05$. We use our results to determine the spin equilibrium of black hole accretion discs with a range of thicknesses and to determine how electromagnetic stresses within the ISCO depend upon black hole spin and disc thickness. We find that the electromagnetic stress and the luminosity inside the ISCO depend on the assumed initial magnetic field geometry. We consider a second geometry with field lines following density contours, which for thin discs leads to highly radially elongated magnetic field lines. This gives roughly twice larger deviations from NT for both the accreted specific angular momentum and the luminosity inside the ISCO. Lastly, we find that the disc's corona (including any wind or jet) introduces deviations from NT in the specific angular momentum that are comparable to those contributed by the disc component, while the excess luminosity of bound gas from within the ISCO is dominated by only the disc component. Based on these indications, we suggest that differences in results between our work and other similar work are due to differences in the assumed initial magnetic field geometry as well as the inclusion of disc

★E-mail: rpenna@cfa.harvard.edu (RFP); jmckinne@stanford.edu (JCM); rnarayan@cfa.harvard.edu (RN); atchekho@cfa.harvard.edu (AT); shafee@fas.harvard.edu (RS); jmcclintock@cfa.harvard.edu (JEM)
† Chandra Fellow

gas versus all the gas when comparing the specific angular momentum from the simulations with the NT model.

Key words: accretion, accretion discs – black hole physics – gravitation – hydrodynamics – MHD – methods: numerical.

1 INTRODUCTION

Accreting black holes (BHs) are among the most powerful astrophysical objects in the Universe. Although they have been the target of intense research for a long time, many aspects of BH accretion theory remain uncertain to this day. Pioneering work by Bardeen (1970), Shakura & Sunyaev (1973), Novikov & Thorne (1973) (hereafter NT), Page & Thorne (1974) and others indicated that BH accretion through a razor-thin disc can be highly efficient, with up to 42 per cent of the accreted rest-mass-energy being converted into radiation. These authors postulated the existence of a turbulent viscosity in the disc, parametrized via the famous α-prescription (Shakura & Sunyaev 1973). This viscosity causes outwards transport of angular momentum; in the process, it dissipates energy and produces the radiation. The authors also assumed that, within the innermost stable circular orbit (ISCO) of the BH, the viscous torque vanishes and material plunges into the BH with constant energy and angular momentum flux per unit rest-mass flux. This is the so-called 'zero-torque' boundary condition.

Modern viscous hydrodynamical calculations of discs with arbitrary thicknesses suggest that the zero-torque condition is a good approximation when the height (h) to radius (r) ratio of the accreting gas is small: $|h/r| \lesssim 0.1$ (Paczyński 2000; Afshordi & Paczyński 2003; Shafee, Narayan & McClintock 2008b; Sądowski 2009; Abramowicz et al. 2010). Radiatively efficient discs in active galactic nuclei (AGN) and X-ray binaries are expected to have disc thickness $|h/r| < 0.1$ whenever the luminosity is limited to less than about 30 per cent of the Eddington luminosity (McClintock et al. 2006). The above hydrodynamical studies thus suggest that systems in this limit should be described well by the standard relativistic thin disc theory as originally developed by NT.

In parallel with the above work, it has for long been recognized that the magnetic field could be a complicating factor that may significantly modify accretion dynamics near and inside the ISCO (Thorne 1974). This issue has become increasingly important with the realization that angular momentum transport in discs is entirely due to turbulence generated via the magnetorotational instability (MRI) (Balbus & Hawley 1991, 1998). However, the magnetic field does not necessarily behave like a local viscous hydrodynamical stress. Near the BH, the magnetic field may have large-scale structures (MacDonald 1984), which can induce stresses across the ISCO (Krolik 1999; Gammie 1999; Agol & Krolik 2000), leading to changes in, e.g., the density, velocity, and amount of dissipation and emission. Unlike turbulence, the magnetic field can transport angular momentum without dissipation (e.g. Li 2002), or it can dissipate in current sheets without transporting angular momentum. In Agol & Krolik (2000), the additional electromagnetic stresses are treated simply as a freely tunable model parameter on top of an otherwise hydrodynamical model. A more complete magnetohydrodynamical (MHD) model of a magnetized thin disc has been developed by Gammie (1999). In this model, the controlling free parameter is the specific magnetic flux, i.e. magnetic flux per unit rest-mass flux. Larger values of this parameter lead to larger deviations from NT due to electromagnetic stresses, but the exact value of the parameter

for a given accretion disc is unknown. For instance, it is entirely possible that electromagnetic stresses become negligible in the limit when the disc thickness $|h/r| \to 0$. The value of the specific magnetic flux is determined by the non-linear turbulent saturation of the magnetic field, so accretion disc simulations are the best way to establish its magnitude.

The coupling via the magnetic field between a spinning BH and an external disc, or between the hole and the corona, wind and jet (hereafter corona-wind-jet), might also play an important role in modifying the accretion flow near the BH. The wind or jet (hereafter wind-jet) can transport angular momentum and energy away from the accretion disc and BH (Blandford 1976; Blandford & Znajek 1977; McKinney & Gammie 2004; McKinney 2006b; McKinney & Narayan 2007b; Komissarov & McKinney 2007). The wind-jet power depends upon factors such as the BH spin (McKinney 2005; Hawley & Krolik 2006; Komissarov et al. 2007), disc thickness (Meier 2001; Tchekhovskoy, McKinney & Narayan 2008, 2009a; Tchekhovskoy, Narayan & McKinney 2009b, 2010), and the strength and large-scale behaviour of the magnetic field (McKinney & Gammie 2004; Beckwith, Hawley & Krolik 2008a; McKinney & Blandford 2009), and these can affect the angular momentum transport through an accretion disc. In this context, we note that understanding how such factors affect disc structure may be key in interpreting the distinct states and complex behaviours observed for BH X-ray binaries (Fender, Belloni & Gallo 2004; Remillard & McClintock 2006). These factors also affect the BH spin history (Gammie, Shapiro & McKinney 2004), and so must be taken into account when considering the effect of accretion on the cosmological evolution of BH spin (Hughes & Blandford 2003; Gammie et al. 2004; Berti & Volonteri 2008).

Global simulations of accretion discs using general relativistic magnetohydrodynamical (GRMHD) codes (e.g. Gammie, McKinney & Tóth 2003; De Villiers, Hawley & Krolik 2003) currently provide the most complete understanding of how turbulent magnetized accretion flows around BHs work. Most simulations have studied thick ($|h/r| \gtrsim 0.15$) discs without radiative cooling. Such global simulations of the inner accretion flow have shown that fluid crosses the ISCO without any clear evidence that the torque vanishes at the ISCO, i.e. there is no apparent 'stress edge' (McKinney & Gammie 2004; Krolik, Hawley & Hirose 2005; Beckwith, Hawley & Krolik 2008b). Similar results were previously found with a pseudo-Newtonian potential for the BH (Krolik & Hawley 2002). In these studies, a plot of the radial profile of the normalized stress within the ISCO appears to indicate a significant deviation from the NT thin disc theory (Krolik et al. 2005; Beckwith et al. 2008b), and it was thus expected that much thinner discs might also deviate significantly from NT. A complicating factor in drawing firm conclusions from such studies is that the assumed initial global magnetic field geometry and strength can significantly change the magnitude of electromagnetic stresses and associated angular momentum transport inside the ISCO (McKinney & Gammie 2004; Beckwith et al. 2008a).

The implications of the above studies for truly thin discs ($|h/r| \lesssim 0.1$) remain uncertain. Thin discs are difficult to resolve numerically,

and simulations have been attempted only recently. Simulations of thin discs using a pseudo-Newtonian potential for the BH reveal good agreement with standard thin disc theory (Reynolds & Fabian 2008). The first simulation of a thin ($|h/r| \approx 0.05$) disc using a full GRMHD model was by Shafee et al. (2008a, hereafter S08). They considered a non-spinning ($a/M = 0$) BH and an initial field geometry consisting of multiple opposite-polarity bundles of poloidal loops within the disc. They found that, although the stress profile appears to indicate significant torques inside the ISCO, the actual angular momentum flux per unit rest-mass flux through the disc component deviates from the NT prediction by only 2 per cent, corresponding to an estimated deviation in the luminosity of only about 4 per cent. The study by S08 was complemented by Noble, Krolik & Hawley (2009, hereafter N09), who considered a thin ($|h/r| \approx 0.1$) disc around an $a/M = 0.9$ BH and an initial field geometry consisting of a single highly elongated poloidal loop bundle whose field lines follow the density contours of the thin disc. They found 6 per cent more luminosity than predicted by NT. More recently, Noble, Krolik & Hawley (2010, hereafter N10), considered a thin ($|h/r| \approx 0.07$) disc around a non-spinning ($a/M = 0$) BH and reported up to 10 per cent deviations from NT in the specific angular momentum accreted through the accretion flow.

In this paper, we extend the work of S08 by considering a range of BH spins, disc thicknesses, field geometries, box sizes, numerical resolutions, etc. Our primary result is that we confirm S08, viz., geometrically thin discs are well-described by the NT model. We show that there are important differences between the dynamics of the gas in the disc and in the corona-wind-jet. In addition, we find that the torque and luminosity within the ISCO can be significantly affected by the geometry and strength of the initial magnetic field, a result that should be considered when comparing simulation results to thin disc theory. In this context, we discuss likely reasons for the apparently different conclusions reached by N09 and N10.

The equations we solve are given in Section 2, diagnostics are described in Section 3 and our numerical setup is described in Section 4. Results for our fiducial thin disc model for a non-rotating BH are given in Section 5, and we summarize convergence studies in Section 6. Results for a variety of BH spins and disc thicknesses are presented in Section 7 and for thin discs with different magnetic field geometries and strengths in Section 8. We compare our results with previous studies in Section 9, discuss the implications of our results in Section 10 and conclude with a summary of the salient points in Section 11.

2 GOVERNING EQUATIONS

The system of interest to us is a magnetized accretion disc around a rotating BH. We write the BH Kerr metric in Kerr–Schild (KS; horizon-penetrating) coordinates (Font, Ibáñez & Papadopoulos 1998; Papadopoulos & Font 1998), which can be mapped to Boyer–Lindquist (BL) coordinates or an orthonormal basis in any frame (McKinney & Gammie 2004). We work with Heaviside–Lorentz units, set the speed of light and gravitational constant to unity ($c = G = 1$), and let M be the BH mass. We solve the GRMHD equations of motion for rotating BHs (Gammie et al. 2003) with an additional cooling term designed to keep the simulated accretion disc at a desired thickness.

Mass conservation gives

$$\nabla_\mu(\rho_0 u^\mu) = 0, \tag{1}$$

where ρ_0 is the rest-mass density, corresponding to the mass density in the fluid frame, and u^μ is the contravariant four-velocity. Note

that we write the orthonormal three-velocity as v_i (the covariant three-velocity is never used below). Energy-momentum conservation gives

$$\nabla_\mu T^\mu_\nu = S_\nu, \tag{2}$$

where the stress energy tensor T^μ_ν includes both matter and electromagnetic terms,

$$T^\mu_\nu = (\rho_0 + u_g + p_g + b^2)u^\mu u_\nu + (p_g + b^2/2)\delta^\mu_\nu - b^\mu b_\nu, \tag{3}$$

where u_g is the internal energy density and $p_g = (\Gamma - 1)u_g$ is the ideal gas pressure with $\Gamma = 4/3$.[1] The contravariant fluid-frame magnetic four-field is given by b^μ, and is related to the lab-frame three-field via $b^\mu = B^\nu h^\mu_\nu/u^t$ where $h^\mu_\nu = u^\mu u_\nu + \delta^\mu_\nu$ is a projection tensor, and δ^μ_ν is the Kronecker delta function. We write the orthonormal three-field as B_i (the covariant three-field is never used below). The magnetic energy density (u_b) and magnetic pressure (p_b) are then given by $u_b = p_b = b^\mu b_\mu/2 = b^2/2$. Note that the angular velocity of the gas is $\Omega = u^\phi/u^t$. Equation (2) has a source term

$$S_\nu = \left(\frac{dU}{d\tau}\right)u_\nu, \tag{4}$$

which is a radiation four-force corresponding to a simple isotropic comoving cooling term given by $dU/d\tau$. We ignore radiative transport effects such as heat currents, viscous stresses or other effects that would enter as additional momentum sources in the comoving frame. In order to keep the accretion disc thin, we employ the same ad hoc cooling function as in S08:

$$\frac{dU}{d\tau} = -u_g \frac{\log(K/K_c)}{\tau_{cool}} S[\theta], \tag{5}$$

where τ is the fluid proper time, $K = p_g/\rho_0^\Gamma$ is the entropy constant, $K_c = 0.000\,69$ is set to be the same entropy constant as the torus atmosphere and is the entropy constant we cool the disc towards, and $K_0 \gtrsim K_c$ is the entropy constant of the initial torus[2]. The gas cooling time is set to $\tau_{cool} = 2\pi/\Omega_K$, where $\Omega_K = (1/M)/[(a/M) + (R/M)^{3/2}]$ is the Keplerian angular frequency and $R = r \sin\theta$ is the cylindrical radius (We consider variations in the cooling time-scale in section 5.7.). We use a shaping function given by the quantity $S[\theta] = \exp[-(\theta - \pi/2)^2/(2(\theta_{nocool})^2)]$, where we set $\theta_{nocool} = \{0.1, 0.3, 0.45, 0.45\}$ for our sequence of models with target thickness of $|h/r| = \{0.07, 0.1, 0.2, 0.3\}$, although we note that the thickest model with target $|h/r| = 0.3$ has no cooling turned on. The shaping function $S[\theta]$ is used to avoid cooling in the low-density funnel-jet region where the thermodynamics is not accurately evolved and where the gas is mostly unbound (see Fig. 13 in Section 5.7). In addition, we set the cooling function $dU/d\tau = 0$ if (1) the time-step, dt, obeys $dt > \tau_{cool}$, which ensures that the cooling does not create negative entropy gas; or (2) $\log(K/K_c) <$

---

[1] Models with $\Gamma = 5/3$ show some minor differences compared to models with $\Gamma = 4/3$ (McKinney & Gammie 2004; Mignone & McKinney 2007).
[2] We intended to have a constant K everywhere at $t = 0$, but a normalization issue led to $K_c \lesssim K_0$. Because of this condition, the disc cools towards a slightly thinner equilibrium at the start of the simulation, after which the cooling proceeds as originally desired by cooling towards the fiducial value $K = K_c$. Our models with $|h/r| \approx 0.07$ are least affected by this issue. Also, since we do not make use of the cooling-based luminosity near $t = 0$, this issue does not affect any of our results. We confirmed that this change leads to no significant issues for either the magnitude or scaling of quantities with thickness by repeating some simulations with the intended $K_c = K_0$. The otherwise similar simulations have thicker discs as expected (very minor change for our thin disc model as expected), and we find consistent results for a given measured thickness in the saturated state.

0, which ensures the gas is only cooled, never heated. Photon capture by the BH is not included, so the luminosity based upon this cooling function is an upper limit for radiation from the disc. The above cooling function drives the specific entropy of the gas towards the reference specific entropy K_c. Since specific entropy always increases due to dissipation, this cooling function explicitly tracks dissipation. Hence, the luminosity generated from the cooling function should not be considered as the true luminosity, but instead should be considered as representing the emission rate in the limit that all dissipated energy is lost as radiation. Any other arbitrary cooling function that does not track dissipation would require full radiative transfer to obtain the true luminosity.

Magnetic flux conservation is given by the induction equation

$$\partial_t(\sqrt{-g}B^i) = -\partial_j[\sqrt{-g}(B^i v^j - B^j v^i)], \tag{6}$$

where $v^i = u^i/u^t$, and $g = \text{Det}\,(g_{\mu\nu})$ is the determinant of the metric. In steady state, the cooling is balanced by heating from shocks, grid-scale reconnection and grid-scale viscosity. No explicit resistivity or viscosity is included.

3 DIAGNOSTICS

In this section, we describe several important diagnostics that we have found useful in this study. First, since we regulate the disc height via an ad hoc cooling function, we check the scaleheight of the simulated disc as a function of time and radius to ensure that our cooling function operates properly. Secondly, the equations we solve consist of seven time-dependent ideal MHD equations, corresponding to four relevant conserved quantities.[3] Using these quantities we construct three dimensionless flux ratios corresponding to the accreted specific energy, specific angular momentum and specific magnetic flux. Thirdly, we check what the duration of the simulations should be in order to reach a quasi-steady-state ('inflow equilibrium') at any given radius. Finally, we describe how we compute the luminosity.

When the specific fluxes are computed as a spatial or temporal average/integral, we always take the ratio of averages/integrals of fluxes (i.e. $\int dx\, F_1 / \int dx\, F_2$) rather than the average/integral of the ratio of fluxes (i.e. $\int dx (F_1/F_2)$). The former is more appropriate for capturing the mean behaviour, while the latter can be more appropriate when investigating fluxes with significant phase-shifted correlations between each other. As relevant for this study, the accretion disc has significant vertical stratification and the local value of the ratio of fluxes can vary considerably without any effect on the bulk accretion flow. Similarly, potentially one flux can (e.g.) nearly vanish over short periods, while the other flux does not, which leads to unbounded values for the ratio of fluxes. However, the time-averaged behaviour of the flow is not greatly affected by such short periods of time. These cases demonstrate why the ratio of averages/integrals is always performed for both spatial and temporal averages/integrals.

When comparing the flux ratios or luminosities from the simulations against the NT model, we evaluate the per cent relative difference $D[f]$ between a quantity f and its NT value as follows:

$$D[f] \equiv 100\frac{f - f[\text{NT}]}{f[\text{NT}]}. \tag{7}$$

For a density-weighted time-averaged value of f, we compute

$$\langle f \rangle_{\rho_0} \equiv \frac{\iiint f\, \rho_0(r, \theta, \phi)\mathrm{d}A_{\theta\phi}\mathrm{d}t}{\iiint \rho_0(r, \theta, \phi)\mathrm{d}A_{\theta\phi}\mathrm{d}t}, \tag{8}$$

where $\mathrm{d}A_{\theta\phi} \equiv \sqrt{-g}\mathrm{d}\theta\mathrm{d}\phi$ is an area element in the $\theta - \phi$ plane, and the integral over $\mathrm{d}t$ is a time average over the duration of interest, which corresponds to the period when the disc is in steady state. For a surface-averaged value of f, we compute

$$\langle f \rangle \equiv \frac{\iint f\mathrm{d}A_{\theta\phi}}{\iint \mathrm{d}A_{\theta\phi}}. \tag{9}$$

3.1 Disc thickness measurement

We define the dimensionless disc thickness per unit radius, $|h/r|$, as the density-weighted mean angular deviation of the gas from the midplane,

$$\left|\frac{h}{r}\right| \equiv \left\langle \left|\theta - \frac{\pi}{2}\right| \right\rangle_{\rho_0}. \tag{10}$$

(This quantity was called $\Delta\theta_{\text{abs}}$ in S08.) Notice that we assume the accretion disc plane is on the equator (i.e. we assume $\langle\theta\rangle_{\rho_0} = \pi/2$). As defined above, $|h/r|$ is a function of r. When we wish to characterize the disc by means of a single estimate of its thickness, we use the value of $|h/r|$ at $r = 2r_{\text{ISCO}}$, where r_{ISCO} is the ISCO radius ($r_{\text{ISCO}} = 6M$ for a non-spinning BH and $r_{\text{ISCO}} = M$ for a maximally spinning BH; Shapiro & Teukolsky 1983). As we show in Section 5.4, this choice is quite reasonable. An alternative thickness measure, given by the root-mean-square thickness $(h/r)_{\text{rms}}$, allows us to estimate how accurate we can be about our definition of thickness. This quantity is defined by

$$\left(\frac{h}{r}\right)_{\text{rms}} \equiv \left\langle \left(\theta - \frac{\pi}{2}\right)^2 \right\rangle_{\rho_0}^{1/2}. \tag{11}$$

The range of θ for the disc thickness integrals in the above equations is from 0 to π.

3.2 Fluxes of mass, energy and angular momentum

The mass, energy and angular momentum conservation equations give the following fluxes:

$$\dot{M}(r, t) = -\int_\theta \int_\phi \rho_0 u^r \mathrm{d}A_{\theta\phi}, \tag{12}$$

$$\mathrm{e} \equiv \frac{\dot{E}(r, t)}{\dot{M}(r, t)} = \frac{\int_\theta \int_\phi T^r_t \mathrm{d}A_{\theta\phi}}{\dot{M}(r, t)}, \tag{13}$$

$$\jmath \equiv \frac{\dot{J}(r, t)}{\dot{M}(r, t)} = -\frac{\int_\theta \int_\phi T^r_\phi \mathrm{d}A_{\theta\phi}}{\dot{M}(r, t)}. \tag{14}$$

The above relations define the rest-mass accretion rate (sometimes just referred to as the mass accretion rate), $\dot{M}$; the accreted energy flux per unit rest-mass flux, or *specific energy*, e; and the accreted angular momentum flux per unit rest-mass flux, or *specific angular momentum*, $\jmath$. Positive values of these quantities correspond to an inward flux through the BH horizon.

The BH spin evolves due to the accretion of mass, energy and angular momentum, which can be described by the dimensionless spin-up parameter s,

$$s \equiv \frac{\mathrm{d}(a/M)}{\mathrm{d}t}\frac{M}{\dot{M}} = \jmath - 2\frac{a}{M}\mathrm{e}, \tag{15}$$

---

[3] The energy momentum of the fluid is not strictly conserved because of radiative cooling; however, the fluid component of the energy-momentum equations still proves to be useful. Only energy conservation of the fluid is strongly affected for our types of models.

where the angular integrals used to compute $\jmath$ and e include all θ and ϕ angles (Gammie et al. 2004). For $s = 0$ the BH is in so-called 'spin equilibrium', corresponding to when the dimensionless BH spin, a/M, does not change in time.

The 'nominal' efficiency, corresponding to the total loss of specific energy from the fluid, is obtained by removing the rest-mass term from the accreted specific energy:

$$\tilde{e} \equiv 1 - e. \qquad (16)$$

The time-averaged value of $\tilde{e}$ at the horizon $(r = r_H)$ gives the total nominal efficiency: $\langle \tilde{e}(r_H) \rangle$, which is an upper bound on the total photon radiative efficiency.

The range of θ over which the flux density integrals in the above equations are computed depends on the situation. In S08, we limited the θ range to $\delta\theta = \pm 0.2$ corresponding to 2–3 density scaleheights in order to focus on the disc and to avoid including the disc wind or BH jet. In this paper, we are interested in studying how the contributions to the fluxes vary as a function of height above the equatorial plane. Our expectation is that the disc and corona-wind-jet contribute differently to these fluxes. Thus, we consider different ranges of θ in the integrals, e.g. from $(\pi/2) - 2|h/r|$ to $(\pi/2) + 2|h/r|$, $(\pi/2) - 4|h/r|$ to $(\pi/2) + 4|h/r|$, or 0 to π. The first and third are most often used in later sections.

3.3 Splitting angular momentum flux into ingoing and outgoing components

For a more detailed comparison of the simulation results with the NT model, we decompose the flux of angular momentum into an ingoing ('in') term which is related to the advection of mass-energy into the BH and an outgoing ('out') term which is related to the forces and stresses that transport angular momentum radially outward. These ingoing and outgoing components of the specific angular momentum are defined by

$$\jmath_{in}(r, t) \equiv \frac{\langle(\rho_0 + u_g + b^2/2)u^r\rangle \langle u_\phi \rangle}{\langle -\rho_0 u^r \rangle}, \qquad (17)$$

$$\jmath_{out}(r, t) \equiv \jmath - \jmath_{in}(r, t). \qquad (18)$$

By this definition, the 'in' quantities correspond to inward transport of the comoving mass-energy density of the disc, $u^\mu u^\nu T_{\mu\nu} = \rho_0 + u_g + b^2/2$. Note that 'in' quantities are products of the mean velocity fields $\langle u^r \rangle$ and $\langle u_\mu \rangle$ and not the combination $\langle u^r u_\mu \rangle$; the latter includes a contribution from correlated fluctuations in u^r and u_μ, which corresponds to the Reynolds stress. The residual of the total flux minus the 'in' flux gives the outward, mechanical transport by Reynolds stresses and electromagnetic stresses. One could also consider a similar splitting for the specific energy. The above decomposition most closely matches our expectation that the inward flux should agree with the NT result as $|h/r| \to 0$. Note, however, that our conclusions in this paper do not require any particular decomposition. This decomposition is different from S08 and N10 where the entire magnetic term $(b^2 u^r u_\phi - b^r b_\phi)$ is designated as the 'out' term. Their choice overestimates the effect of electromagnetic stresses, since some magnetic energy is simply advected into the BH. Also, the splitting used in S08 gives non-monotonic $\jmath_{in}$ versus radius for some BH spins, while the splitting we use gives monotonic values for all BH spins.

3.4 The magnetic flux

The no-monopoles constraint implies that the total magnetic flux $(\Phi = \int_S \boldsymbol{B} \cdot \boldsymbol{dA})$ vanishes through any closed surface or any open surface penetrating a bounded flux bundle. The magnetic flux conservation equations require that magnetic flux can only be transported to the BH or through the equatorial plane by advection. The absolute magnetic flux $(\int_S |\boldsymbol{B} \cdot \boldsymbol{dA}|)$ has no such restrictions and can grow arbitrarily due to the MRI. However, the absolute magnetic flux can saturate when the electromagnetic field comes into force balance with the matter. We are interested in such a saturated state of the magnetic field within the accretion flow and threading the BH.

We consider the absolute magnetic flux penetrating a spherical surface and an equatorial surface given, respectively, by

$$\Phi_r(r, \theta, t) = \int_\theta \int_\phi |B^r| dA_{\theta'\phi}, \qquad (19)$$

$$\Phi_\theta(r, \theta, t) = \int_{r'=r_H}^{r'=r} \int_\phi |B^\theta| dA_{r'\phi}. \qquad (20)$$

Nominally, Φ_r has an integration range of $\theta' = 0$ to $\theta' = \theta$ when measured on the BH horizon, while when computing quantities around the equatorial plane θ' has the range $\langle\theta\rangle \pm \theta$. One useful normalization of the magnetic fluxes is by the total flux through one hemisphere of the BH plus through the equator

$$\Phi_{tot}(r, t) \equiv \Phi_r(r' = r_H, \theta' = 0 \ldots \pi/2, t) + \Phi_\theta(r, \theta' = \pi/2, t), \qquad (21)$$

which gives the normalized absolute radial magnetic flux

$$\tilde{\Phi}_r(r, \theta, t) \equiv \frac{\Phi_r(r, \theta, t)}{\Phi_{tot}(r = R_{out}, t = 0)}, \qquad (22)$$

where R_{out} is the outer radius of the computational box. The normalized absolute magnetic flux measures the absolute magnetic flux on the BH horizon or radially through the equatorial disc per unit absolute flux that is initially available.

The Gammie (1999) model of a magnetized thin accretion flow suggests another useful normalization of the magnetic flux is by the absolute mass accretion rate

$$\dot{M}_G(r, t) \equiv \int_\theta \int_\phi \rho_0 |u^r| dA_{\theta\phi}, \qquad (23)$$

which gives the normalized specific absolute magnetic fluxes

$$\Xi(r, t) = \frac{\Phi_r(r, t)}{\dot{M}_G(r, t)}, \qquad (24)$$

$$\Upsilon(r, t) \equiv \sqrt{2} \left| \frac{\Xi(r, t)}{M} \right| \sqrt{\left| \frac{\dot{M}_G(r = r_H, t)}{SA_H} \right|}, \qquad (25)$$

where $SA = (1/r^2) \int_\theta \int_\phi dA_{\theta\phi}$ is the local solid angle, $SA_H = SA(r = r_H)$ is the local solid angle on the horizon, $\Xi(r, t)$ is the radial magnetic flux per unit rest-mass flux (usually specific magnetic flux) and $\Upsilon(r, t)c^{3/2}/G$ is a particular dimensionless normalization of the specific magnetic flux that appears in the MHD accretion model developed by Gammie (1999). Since the units used for the magnetic field are arbitrary, any constant factor can be applied to Ξ and one would still identify the quantity as the specific magnetic flux. So to simplify the discussion we henceforth call Υ the specific magnetic flux. To obtain equation (25), all involved integrals should have a common θ range around the equator. These quantities all have absolute magnitudes because a sign change does not change the physical effect. The quantities $\jmath$, e, $\tilde{e}$, Ξ and Υ are each conserved along poloidal field-flow lines for stationary ideal MHD solutions (Bekenstein & Oron 1978; Takahashi et al. 1990).

Gammie's (1999) model of a magnetized accretion flow within the ISCO assumes: (1) a thin equatorial flow; (2) a radial poloidal field geometry (i.e. $|B_\theta| \ll |B_r|$); (3) a boundary condition at the ISCO corresponding to zero radial velocity and (4) no thermal contribution. The model reduces to the NT solution within the ISCO for $\Upsilon \to 0$, and deviations from NT's solution are typically small (less than 12 per cent for $_J$ across all BH spins; see Appendix A) for $\Upsilon \lesssim 1$. We have defined the quantity Υ in equation (24) with the $\sqrt{2}$ factor, the square root of the total mass accretion rate through the horizon per unit solid angle and Heaviside–Lorentz units for B^r so that the numerical value of Υ at the horizon is identically equal to the numerical value of the free parameter in Gammie (1999), i.e. their $F_{\theta\phi}$ normalized by $F_M = -1$. As shown in that paper, Υ directly controls deviations of the specific angular momentum and specific energy away from the non-magnetized thin disc theory values of the NT model. Even for discs of finite thickness, the parameter shows how electromagnetic stresses control deviations between the horizon and the ISCO. Note that the flow can deviate from NT at the ISCO simply due to finite thermal pressure (McKinney & Gammie 2004). In Appendix (Table A1), we list numerical values of $_J$ and $\tilde{e}$ for Gammie's (1999) model, and show how these quantities deviate from NT for a given BH spin and Υ.

We find Υ to be more useful as a measure of the importance of the magnetic field within the ISCO than our previous measurement in S08 of the α-viscosity parameter,

$$\alpha = \frac{T^{\hat{\phi}\hat{r}}}{p_g + p_b}, \tag{26}$$

where $T^{\hat{\phi}\hat{r}} = e^{\hat{\phi}}_\mu e^{\hat{r}}_\nu T^{\mu\nu}$ is the orthonormal stress-energy tensor components in the comoving frame, and $e^{\hat{\nu}}_\mu$ is the orthonormal contravariant tetrad system in the local fluid-frame. This is related to the normalized stress by

$$\frac{W}{\dot{M}} = \frac{\int\int T^{\hat{\phi}\hat{r}} dA'_{\theta\phi}}{\dot{M} \int_\phi dL'_\phi}, \tag{27}$$

where $dA'_{\theta\phi} = e^{\hat{\theta}}_\mu e^{\hat{\phi}}_\nu d\theta^\mu d\phi^\nu$ is the comoving area element, $dL'_\phi = e^{\hat{\phi}}_\nu d\phi^\nu$ evaluated at $\theta = \pi/2$ is the comoving ϕ length element, $\theta^\mu = \{0, 0, 1, 0\}$ and $\phi^\nu = \{0, 0, 0, 1\}$. This form for W is a simple generalization of equation (5.6.1b) in NT73, and note that the NT solution for $W/\dot{M}$ is given by equation (5.6.14a) in NT73. In S08, W was integrated over fluid satisfying $-u_t(\rho_0 + u_g + p_g + b^2)/\rho_0 < 1$ (i.e. only approximately gravitationally bound fluid and no wind-jet). We use the same definition of bound in this paper. As shown in S08, a plot of the radial profile of $W/\dot{M}$ or α within the ISCO does not necessarily quantify how much the magnetic field affects the accretion flow properties, since even apparently large values of this quantity within the ISCO do not cause a significant deviation from NT in the specific angular momentum accreted. On the other hand, the Gammie (1999) parameter Υ does directly relate to the electromagnetic stresses within the ISCO and is an ideal MHD invariant (so constant versus radius) for a stationary radial flow. One expects that appropriately time-averaged simulation data could be framed in the context of this stationary model in order to measure the effects of electromagnetic stresses.

3.5 Inflow equilibrium

When the accretion flow has achieved steady state inside a given radius, the quantity $\dot{M}(r, t)$ will (apart from normal fluctuations due to turbulence) be independent of time, and if it is integrated over

all θ angles will be constant within the given radius.[4] The energy and angular momentum fluxes have a non-conservative contribution due to the cooling function and therefore are not strictly constant. However, the cooling is generally a minor contribution (especially in the case of the angular momentum flux), and so we may still measure the non-radiative terms to verify inflow equilibrium.

The radius out to which inflow equilibrium can be achieved in a given time can be estimated by calculating the mean radial velocity v_r and then deriving from it a viscous time-scale $-r/v_r$. From standard accretion disc theory and using the definition of α given in equation (27), the mean radial velocity is given by

$$v_r \sim -\alpha \left|\frac{h}{r}\right|^2 v_K, \tag{28}$$

where $v_K \approx (r/M)^{-1/2}$ is the Keplerian speed at radius r and α is the standard viscosity parameter given by equation (26) (Frank, King & Raine 1992). Although the viscous time-scale is the nominal time needed to achieve steady state, in practice it takes several viscous times before the flow really settles down, e.g. see the calculations reported in Shapiro (2010). In the present paper, we assume that inflow equilibrium is reached after two viscous times, and hence we estimate the inflow equilibrium time, t_{ie}, to be

$$t_{ie} \sim -2\frac{r}{v_r} \sim 2\left(\frac{r}{M}\right)^{3/2}\left(\frac{1}{\alpha|h/r|^2}\right) \sim 5000\left(\frac{r}{M}\right)^{3/2}, \tag{29}$$

where, in the right-most relation, we have taken a typical value of $\alpha \sim 0.1$ for the gas in the disc proper (i.e. outside the ISCO) and we have set $|h/r| \approx 0.064$, as appropriate for our thinnest disc models.

A simulation must run until $t \sim t_{ie}$ before we can expect inflow equilibrium at radius r. According to the above Newtonian estimate, a thin disc simulation with $|h/r| \sim 0.064$ that has been run for a time of $30000M$ will achieve steady state out to a radius of only $\sim 3M$. However, this estimate is inaccurate since it does not allow for the boundary condition on the flow at the ISCO. Both the boundary condition and the effects of GR are included in the formula for the radial velocity given in equation (5.9.8) of NT, which we present for completeness in Appendix B. That more accurate result, which is what we use for all our plots and numerical estimates, shows that our thin disc simulations should reach inflow equilibrium within $r/M = 9, 7, 5.5, 5$, respectively, for $a/M = 0, 0.7, 0.9, 0.98$. These estimates are roughly consistent with the radii out to which we have a constant $_J$ versus radius in the simulations discussed in Section 7.

3.6 Luminosity measurement

We measure the radiative luminosity of the accreting gas directly from the cooling function $dU/d\tau$. At a given radius, r, in the steady region of the flow, the luminosity per unit rest-mass accretion rate interior to that radius is given by

$$\frac{L(<r)}{\dot{M}(r, t)} = \frac{1}{\dot{M}(r, t)(t_f - t_i)} \int_{t=t_i}^{t_f} \int_{r'=r_H}^{r} \int_{\theta=0}^{\pi} \int_\phi \left(\frac{dU}{d\tau}\right) u_t \, dV_{tr'\theta\phi}, \tag{30}$$

where $dV_{tr'\theta\phi} = \sqrt{-g} dt \, dr' \, d\theta \, d\phi$ and the 4D integral goes from the initial time t_i to the final time t_f over which the simulation

---

[4] If we integrate over a restricted range of θ, then there could be additional mass flow through the boundaries in the θ direction and $\dot{M}(r, t)$ will no longer be independent of r, though it would still be independent of t.

results are time-averaged, from the radius r_H of the horizon to the radius r of interest, and usually over all θ and ϕ. We find it useful to compare the simulations with thin disc theory by computing the ratio of the luminosity emitted inside the ISCO (per unit rest-mass accretion rate) to the total radiative efficiency of the NT model:

$$\tilde{L}_{in} \equiv \frac{L(< r_{ISCO})}{\dot{M}\tilde{e}[NT]}. \qquad (31)$$

This ratio measures the excess radiative luminosity from inside the ISCO in the simulation relative to the total luminosity in the NT model (which predicts zero luminosity here). We also consider the excess luminosity over the entire inflow equilibrium region

$$\tilde{L}_{eq} \equiv \frac{L(r < r_{eq}) - L(r < r_{eq})[NT]}{\dot{M}\tilde{e}[NT]}, \qquad (32)$$

which corresponds to the luminosity (per unit mass accretion rate) inside the inflow equilibrium region (i.e. $r < r_{eq}$, where r_{eq} is the radius out to which inflow equilibrium has been established) subtracted by the NT luminosity all divided by the total NT efficiency. Large per cent values of $\tilde{L}_{in}$ or $\tilde{L}_{eq}$ would indicate large per cent deviations from NT.

4 PHYSICAL MODELS AND NUMERICAL METHODS

This section describes our physical models and numerical methods. Table 1 provides a list of all our simulations and shows the physical and numerical parameters that we vary. Our primary models are labelled by names of the form AxHRy, where x is the value of the BH spin parameter and y is approximately equal to the disc thickness $|h/r|$. For instance, our fiducial model A0HR07 has a non-spinning BH ($a/M = 0$) and a geometrically thin disc with

$|h/r| \sim 0.07$. We discuss this particular model in detail in Section 5. Table 1 also shows the time span (from T_i/M to T_f/M) used to perform the time-averaging, and the last column shows the actual value of $|h/r|$ in the simulated model as measured during inflow equilibrium, e.g. $|h/r| = 0.064$ for model A0HR07.

4.1 Physical models

This study considers BH accretion disc systems with a range of BH spins: $a/M = 0, 0.7, 0.9, 0.98$ and a range of disc thicknesses: $|h/r| = 0.07, 0.13, 0.2, 0.3$. The initial mass distribution is an isentropic equilibrium torus (Chakrabarti 1985a,b; De Villiers et al. 2003). All models have an initial inner torus edge at $r_{in} = 20M$, while the torus pressure maximum for each model is located between $R_{max} = 35M$ and $R_{max} = 65M$. We chose this relatively large radius for the initial torus because S08 found that placing the torus at smaller radii caused the results to be sensitive to the initial mass distribution. We initialize the solution so that $\rho_0 = 1$ is the maximum rest-mass density. In S08, we set $q = 1.65$ ($\Omega \propto r^{-q}$ in non-relativistic limit) and $K = 0.00034$ with $\Gamma = 4/3$, while in this paper we adjust the initial angular momentum profile such that the initial torus has the target value of $|h/r|$ at the pressure maximum. For models with $|h/r| = 0.07, 0.13, 0.2, 0.3$, we fix the specific entropy of the torus by setting, respectively, $K = K_0 \equiv \{0.00034, 0.0035, 0.009, 0.009\}$ in the initial polytropic equation of state given by $p = K_0 \rho_0^\Gamma$. The initial atmosphere surrounding the torus has the same polytropic equation of state with nearly the same entropy constant of $K = 0.00069$, but with an initial rest-mass density of $\rho_0 = 10^{-6}(r/M)^{-3/2}$, corresponding to a Bondi-like atmosphere.

Recent GRMHD simulations of thick discs indicate that the results for the disc (but not the wind-jet) are roughly independent of the initial field geometry (McKinney & Narayan 2007a,b; Beckwith

Table 1. Simulation parameters.

Model name	$T_i/M - T_f/M$	$\frac{a}{M}$	N_r	N_θ	N_ϕ	$\frac{R_{in}}{r_H}$	Y	$\Delta\phi$	$\frac{R_{max}}{M}$	$\frac{R_{out}}{M}$	q	Cooling	$\frac{\lambda_{field}}{2\pi r}$	$\frac{h}{r}$
A0HR07	12500–27350	0	256	64	32	0.9	0.13	$\pi/2$	35	50	1.65	Yes	0.065	0.064
A7HR07	12500–20950	0.7	256	64	32	0.92	0.13	$\pi/2$	35	50	1.65	Yes	0.065	0.065
A9HR07	14000–23050	0.9	256	64	32	0.92	0.13	$\pi/2$	35	50	1.65	Yes	0.065	0.054
A98HR07	14000–19450	0.98	256	64	32	0.92	0.13	$\pi/2$	35	50	1.65	Yes	0.065	0.059
A0HR1	5050–14150	0	256	64	32	0.9	0.37	$3\pi/4$	45	120	1.94	Yes	0.25	0.12
A7HR1	5050–12550	0.7	256	64	32	0.9	0.37	$3\pi/4$	45	120	1.92	Yes	0.25	0.09
A9HR1	5050–10000	0.9	256	64	32	0.9	0.37	$3\pi/4$	45	120	1.91	Yes	0.25	0.13
A98HR1	12000–13600	0.98	256	64	32	0.9	0.37	$3\pi/4$	45	120	1.91	Yes	0.25	0.099
A0HR2	6000–13750	0	256	64	32	0.9	0.65	π	65	200	1.97	Yes	0.28	0.18
A7HR2	12000–17900	0.7	256	64	32	0.9	0.65	π	65	200	1.97	Yes	0.28	0.16
A9HR2	12000–15200	0.9	256	64	32	0.88	0.65	π	65	200	1.97	Yes	0.28	0.21
A98HR2	6100–7100	0.98	256	64	32	0.9	0.65	π	65	200	1.97	Yes	0.28	0.18
A0HR3	4700–7900	0	256	64	32	0.9	0.65	π	65	200	1.97	No	0.28	0.35
A7HR3	10000–11900	0.7	256	64	32	0.9	0.65	π	65	200	1.97	No	0.28	0.34
A9HR3	4700–7900	0.9	256	64	32	0.88	0.65	π	65	200	1.97	No	0.28	0.341
A98HR3	4700–7900	0.98	256	64	32	0.9	0.65	π	65	200	1.97	No	0.28	0.307
C0	6000–10000	0	512	128	32	0.9	0.15	$\pi/4$	35	50	1.65	Yes	0.16	0.052
C1	12500–18900	0	256	64	16	0.9	0.13	$\pi/4$	35	50	1.65	Yes	0.065	0.063
C2	12500–22500	0	256	64	64	0.9	0.13	π	35	50	1.65	Yes	0.065	0.062
C3	12500–19500	0	256	64	16	0.9	0.13	$\pi/2$	35	50	1.65	Yes	0.065	0.061
C4	12500–21700	0	256	64	64	0.9	0.13	$\pi/2$	35	50	1.65	Yes	0.065	0.061
C5	12500–20000	0	256	32	32	0.9	0.13	$\pi/2$	35	50	1.65	Yes	0.065	0.052
C6	12500–20800	0	256	128	32	0.9	0.13	$\pi/2$	35	50	1.65	Yes	0.065	0.065
A0HR07LOOP1	17000–22100	0	256	64	32	0.9	0.13	$\pi/2$	35	50	1.65	Yes	0.25	0.048
A0HR3LOOP1	3000–8000	0	256	64	32	0.9	0.65	π	65	200	1.97	No	0.5	0.377

et al. 2008a). However, a detailed study for thin discs is yet to be performed.

We consider a range of magnetic field geometries described by the vector potential A_μ which is related to the Faraday tensor by $F_{\mu\nu} = A_{\nu,\mu} - A_{\mu,\nu}$. As in S08, we consider a general multiple-loop field geometry corresponding to N separate loop bundles stacked radially within the initial disc. The vector potential we use is given by

$$A_{\phi,\mathrm{N}} \propto Q^2 \sin\left(\frac{\log(r/S)}{\lambda_{\mathrm{field}}/(2\pi r)}\right) [1 + w(\mathrm{ranc} - 0.5)], \qquad (33)$$

where ranc is a random number generator for the domain 0 to 1 (see below for a discussion of perturbations.). All other A_μ are initially zero. All our multi-loop and one-loop simulations have $S = 22M$, and the values of $\lambda_{\mathrm{field}}/(2\pi r)$ are listed in Table 1. For multi-loop models, each additional field loop bundle has opposite polarity. We use $Q = (u_{\mathrm{g}}/u_{\mathrm{g,max}} - 0.2)(r/M)^{3/4}$, and set $Q = 0$ if either $r < S$ or $Q < 0$, and $u_{\mathrm{g,max}}$ is the maximum value of the internal energy density in the torus. By comparison, in S08, we set $S = 1.1r_{\mathrm{in}}$, $r_{\mathrm{in}} = 20M$, $\lambda_{\mathrm{field}}/(2\pi r) = 0.16$, such that there were two loops centred at $r = 28M$ and $38M$. The intention of introducing multiple-loop bundles is to keep the aspect ratio of the bundles roughly 1:1 in the poloidal plane, rather than loop(s) that are highly elongated in the radial direction. For each disc thickness, we tune $\lambda_{\mathrm{field}}/(2\pi r)$ in order to obtain initial poloidal loops that are roughly isotropic.

As in S08, the magnetic field strength is set such that the plasma β parameter satisfies $\beta_{\mathrm{maxes}} \equiv p_{\mathrm{g,max}}/p_{b,\mathrm{max}} = 100$, where $p_{\mathrm{g,max}}$ is the maximum thermal pressure and $p_{b,\mathrm{max}}$ is the maximum magnetic pressure in the entire torus. Since the two maxima never occur at the same location, $\beta = p_{\mathrm{g}}/p_b$ varies over a wide range of values within the disc. This approach is similar to how the magnetic field was normalized in other studies (Gammie et al. 2003; McKinney & Gammie 2004; McKinney 2006b; McKinney & Narayan 2007b; Komissarov & McKinney 2007). It ensures that the magnetic field is weak throughout the disc. Care must be taken with how one normalizes any given initial magnetic field geometry. For example, for the one-loop field geometry used by McKinney & Gammie (2004), if one initializes the field with a *mean* (volume-averaged) $\bar\beta = 100$, then the inner edge of the initial torus has $\beta \sim 1$ and the initial disc is not weakly magnetized.

For most models, the vector potential at all grid points was randomly perturbed by 2 per cent (w in equation 33) and the internal energy density at all grid points was randomly perturbed by 10 per cent.[5] If the simulation starts with perturbations of the vector potential, then we compute Φ_{tot} (used to obtain $\tilde\Phi_{\mathrm{r}}$) using the pre-perturbed magnetic flux in order to gauge how much flux is dissipated due to the perturbations. Perturbations should be large enough to excite the non-axisymmetric MRI in order to avoid the axisymmetric channel solution, while they should not be so large as to induce significant dissipation of the magnetic energy due to grid-scale magnetic dissipation just after the evolution begins. For some models, we studied different amplitudes for the initial perturbation in order to ensure that the amplitude does not significantly affect our results. For a model with $|h/r| \sim 0.07$, $a/M = 0$, and a single polarity field loop, one simulation was initialized with 2 per cent vector potential perturbations and 10 per cent internal energy perturbations, while another otherwise similar simulation was given no

seed perturbations. Both become turbulent at about the same time $t \sim 1500M$. The magnetic field energy at that time is negligibly different, and there is no evidence for significant differences in any quantities during inflow equilibrium.

4.2 Numerical methods

We perform simulations using the GRMHD code HARM that is based upon a conservative shock-capturing Godunov scheme. One key feature of our code is that we use horizon-penetrating KS coordinates for the Kerr metric (Gammie, McKinney & Tóth 2003; McKinney & Gammie 2004; McKinney 2006a; Noble et al. 2006; Mignone & McKinney 2007; Tchekhovskoy, McKinney & Narayan 2007), which avoids any issues with the coordinate singularity in BL coordinates. Even with KS coordinates, one must ensure that the inner-radial boundary of the computational domain is outside the so-called inner horizon (at $r/M \equiv 1 - \sqrt{1 - (a/M)^2}$) so that the equations remain hyperbolic, and one must ensure that there are plenty of grid cells spanning the region near the horizon in order to avoid numerical diffusion out of the horizon.

Another key feature of our code is the use of a third-order accurate (fourth-order error) PPM scheme for the interpolation of primitive quantities (i.e. rest-mass density, four-velocity relative to a ZAMO observer and lab-frame three-magnetic field) (McKinney 2006b). The interpolation is similar to that described in Colella & Woodward (1984), but we modified it to be consistent with interpolating through point values of primitives rather than average values. We do not use the PPM steepener, but we do use the PPM flattener that only activates in strong shocks (e.g. in the initial bow shock off the torus surface, but rarely elsewhere). The PPM scheme attempts to fit a monotonic third-order polynomial directly through the grid face where the dissipative flux enters in the Godunov scheme. Only if the polynomial is non-monotonic does the interpolation reduce order and create discontinuities at the cell face, and so only then does it introduce dissipative fluxes. It therefore leads to extremely small dissipation compared to the original schemes used in HARM, such as the first-order accurate (second-order error) minmod or monotonized central (MC) limiter type schemes that always create discontinuities (and so dissipative fluxes) at the cell face regardless of the monotonicity for any primitive quantity that is not linear in space.

Simulations of fully 3D models of accreting BHs producing jets using our 3D GRMHD code show that this PPM scheme leads to an improvement in effective resolution by at least factors of roughly 2 per dimension as compared to the original HARM MC limiter scheme for models with resolution $256 \times 128 \times 32$ (McKinney & Blandford 2009). The PPM method is particularly well-suited for resolving turbulent flows since they rarely have strong discontinuities and have most of the turbulent power in long wavelength modes. Even moving discontinuities are much more accurately resolved by PPM than minmod or MC. For example, even without a steepener, a simple moving contact or moving magnetic rotational discontinuity is sharply resolved within about four cells using the PPM scheme as compared to being diffusively resolved within about 8–15 cells by the MC limiter scheme.

A second-order Runge–Kutta method-of-lines scheme is used to step forward in time, and the time-step is set by using the fast magnetosonic wavespeed with a Courant factor of 0.8. We found that a fourth-order Runge–Kutta scheme does not significantly improve accuracy, since most of the flow is far beyond the grid cells inside the horizon that determine the time-step. The standard HARM HLL

---

[5] In S08, we had a typo saying we perturbed the field by 50 per cent, while it was actually perturbed the same as these models, i.e.: 2 per cent vector potential perturbations and 10 per cent internal energy perturbations.

scheme is used for the dissipative fluxes, and the standard HARM Tóth scheme is used for the magnetic field evolution.

4.3 Numerical model setup

The code uses uniform internal coordinates $(t, x^{(1)}, x^{(2)}, x^{(3)})$ mapped to the physical coordinates (t, r, θ, ϕ). The radial grid mapping is

$$r(x^{(1)}) = R_0 + \exp(x^{(1)}), \tag{34}$$

which spans from R_{in} to R_{out}. The parameter $R_0 = 0.3M$ controls the resolution near the horizon. Absorbing (outflow, no inflow allowed) boundary conditions are used. The θ-grid mapping is

$$\theta(x^{(2)}) = [Y(2x^{(2)} - 1) + (1 - Y)(2x^{(2)} - 1)^7 + 1](\pi/2), \tag{35}$$

where $x^{(2)}$ ranges from 0 to 1 (i.e. no cut-out at the poles) and Y is an adjustable parameter that can be used to concentrate grid zones toward the equator as Y is decreased from 1 to 0. Roughly half of the θ resolution is concentrated in the disc region within $\pm 2|h/r|$ of the midplane. The HR07 and HR2 models listed in Table 1 have 11 cells per $|h/r|$, while the HR1 and HR3 models have seven cells per $|h/r|$. The high-resolution run, C6, has 22 cells per $|h/r|$, while the low-resolution model, C5, has five cells per $|h/r|$. For $Y = 0.15$ this grid gives roughly six times more angular resolution compared to the grid used in McKinney & Gammie (2004) given by equation (8) with $h = 0.3$. Reflecting boundary conditions are used at the polar axes.

The ϕ-grid mapping is given by $\phi(x^{(3)}) = 2\pi x^{(3)}$, such that $x^{(3)}$ varies from 0 to 1/8, 1/4, 3/8, 1/2 for boxes with $\Delta\phi = \pi/4, \pi/2, 3\pi/4, \pi$, respectively. Periodic boundary conditions are used in the ϕ-direction. In all cases, the spatial integrals are renormalized to refer to the full 2π range in ϕ, even if our computational box size is limited in the ϕ-direction. We consider various $\Delta\phi$ in order to check whether this changes our results. Previous GRMHD simulations with the full $\Delta\phi = 2\pi$ extent suggest that $\Delta\phi = \pi/2$ is sufficient since coherent structures only extend for about one radian (see fig. 12 in Schnittman, Krolik & Hawley 2006). However, in other GRMHD studies with $\Delta\phi = 2\pi$, the $m = 1$ mode was found to be dominant, so this requires further consideration (McKinney & Blandford 2009). Note that S08 used $\Delta\phi = \pi/4$, while both N09 and N10 used $\Delta\phi = \pi/2$.

The duration of our simulations with the thinnest discs varies from approximately $20000M$ to $30000M$ in order to reach inflow equilibrium and to minimize fluctuations in time-averaged quantities. We ensure that each simulation runs for a couple of viscous times in order to reach inflow equilibrium over a reasonable range of radius. Note that the simulations cannot be run for a duration longer than $t_{acc} \sim M_{disc}(t = 0)/\dot{M} \sim 10^5 M$, corresponding to the time-scale for accreting a significant fraction of the initial torus. We are always well below this limit.

Given finite computational resources, there is a competition between duration and resolution of a simulation. Our simulations run for relatively long durations, and we use a numerical resolution of $N_r \times N_\theta \times N_\phi = 256 \times 64 \times 32$ for all models (except those used for convergence testing). In S08 we found this resolution to be sufficient to obtain convergence compared to a similar $512 \times 128 \times 32$ model with $\Delta\phi = \pi/4$. In this paper, we explicitly confirm that our resolution is sufficient by convergence testing our results (see section 6). Near the equatorial plane at the ISCO, the grid aspect ratio in $dr : rd\theta : r\sin\theta \, d\phi$ is 2:1:7, 1:1:4, 1:1:3 and 1:1:3, respectively, for our HR07, HR1, HR2 and HR3 models. The 2:1:7 grid aspect ratio for the HR07 model was found to be sufficient in S08. A grid aspect ratio of 1:1:1 would be preferable in order to ensure the dissipation

is isotropic in Cartesian coordinates, since in Nature one would not expect highly anisotropic dissipation on the scale resolved by our grid cells. However, finite computational resources require a balance between a minimum required resolution, grid aspect ratio and duration of the simulation.

As described below, we ensure that the MRI is resolved in each simulation both as a function of space and as a function of time by measuring the number of grid cells per fastest growing MRI mode:

$$Q_{MRI} \equiv \frac{\lambda_{MRI}}{\Delta_{\hat{\theta}}} \approx 2\pi \frac{|v_A^{\hat{\theta}}|/|\Omega(r, \theta)|}{\Delta_{\hat{\theta}}}, \tag{36}$$

where $\Delta_{\hat{\theta}} \equiv |e^{\hat{\theta}}_{\ \mu} dx^\mu|$ is the comoving orthonormal θ-directed grid cell length, $e^{\hat{\theta}}_{\ \mu}$ is the orthonormal contravariant tetrad system in the local fluid-frame, $|v_A^{\hat{\theta}}| = \sqrt{b_{\hat{\theta}} b^{\hat{\theta}}/(b^2 + \rho_0 + u_g + p_g)}$ is the Alfvén speed, $b^{\hat{\theta}} \equiv e^{\hat{\theta}}_{\ \mu} b^\mu$ is the comoving orthonormal θ-directed four-field and $|\Omega(r, \theta)|$ is the temporally and azimuthally averaged absolute value of the orbital frequency.

During the simulation, the rest-mass density and internal energy densities can become quite low beyond the corona, but the code only remains accurate and stable for a finite value of b^2/ρ_0, b^2/u_g, and u_g/ρ_0 for any given resolution. We enforce $b^2/\rho_0 \lesssim 10^4$, $b^2/u_g \lesssim 10^4$ and $u_g/\rho_0 \lesssim 10^4$ by injecting a sufficient amount of mass or internal energy into a fixed zero angular momentum observer (ZAMO) frame with four-velocity $u_\mu = \{-\alpha, 0, 0, 0\}$, where $\alpha = 1/\sqrt{-g^{tt}}$ is the lapse. In some simulations, we have to use stronger limits given by $b^2/\rho_0 \lesssim 10$, $b^2/u_g \lesssim 10^2$ and $u_g/\rho_0 \lesssim 10$, in order to maintain stability and accuracy. Compared to our older method of injecting mass-energy into the comoving frame, the new method avoids run-away injection of energy momentum in the low-density regions. We have confirmed that this procedure of injecting mass-energy does not contaminate our results for the accretion rates and other diagnostics.

5 FIDUCIAL MODEL OF A THIN DISC AROUND A NON-ROTATING BLACK HOLE

Our fiducial model, A0HR07, consists of a magnetized thin accretion disc around a non-rotating ($a/M = 0$) BH. This is similar to the model described in S08; however, here we consider a larger suite of diagnostics, a resolution of $256 \times 64 \times 32$, and a computational box with $\Delta\phi = \pi/2$. As mentioned in Section 4.1, the initial torus parameters are set so that the inner edge is at $r = 20M$, the pressure maximum is at $r = 35M$ and $|h/r| \lesssim 0.1$ at the pressure maximum (see Fig. 1).

The initial torus is threaded with magnetic field in the multi-loop geometry as described in Section 4.1. For this model, we use four loops in order to ensure that the loops are roughly circular in the poloidal plane. Once the simulation begins, the MRI leads to MHD turbulence which causes angular momentum transport and drives the accretion flow to a quasi-steady-state.

The fiducial model is evolved for a total time of $27350M$. We consider the period of steady state to be from $T_i = 12500M$ to $T_f = 27350M$ and of duration $\Delta T = 14850M$. All the steady state results described below are obtained by time-averaging quantities over this steady-state period, which corresponds to about 160 orbital periods at the ISCO, 26 orbits at the inner edge of the initial torus ($r = 20M$) and 11 orbits at the pressure maximum of the initial torus ($r = 35M$).
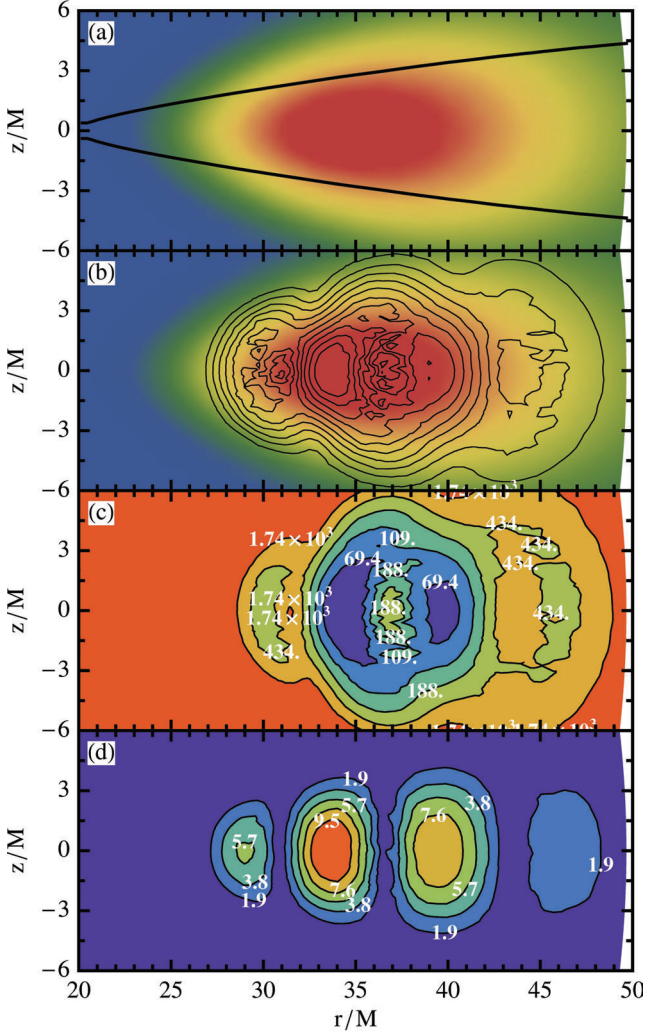
Figure 1. The initial state of the fiducial model (A0HR07) consists of weakly magnetized gas in a geometrically thin torus around a non-spinning ($a/M = 0$) BH. Colour maps have red as the highest values and blue as the lowest values. Panel (a): linear colour map of rest-mass density, with solid lines showing the thickness $|h/r|$ of the initial torus. Note that the BH horizon is at $r = 2M$, far to the left of the plot, so the torus is clearly geometrically thin. Near the pressure maximum $|h/r| \lesssim 0.1$, and elsewhere $|h/r|$ is even smaller. Panel (b): contour plot of b^2 overlaid on linear colour map of rest-mass density shows that the initial field consists of four poloidal loops centred at $r/M = 29, 34, 39, 45$. The wiggles in b^2 are due to the initial perturbations. Panel (c): linear colour map of the plasma β shows that the disc is weakly magnetized throughout the initial torus. Panel (d): linear colour map of the number of grid cells per fastest growing MRI wavelength, Q_{MRI}, shows that the MRI is properly resolved for the primary two loops at the centre of the disc.

5.1 Initial and evolved disc structure

Fig. 1 shows contour plots of various quantities in the initial solution projected on the $(R, z) = (r \sin \theta, r \cos \theta)$-plane. Notice the relatively small vertical extent of the torus. The disc has a thickness of $|h/r| \sim$ 0.06–0.09 over the radius range containing the bulk of the mass. The four magnetic loops are clearly delineated. The plot of Q_{MRI} indicates that the MRI is well-resolved within the two primary loops. The left-most and right-most loops are marginally underresolved, so a slightly slower-growing MRI mode is expected to control the
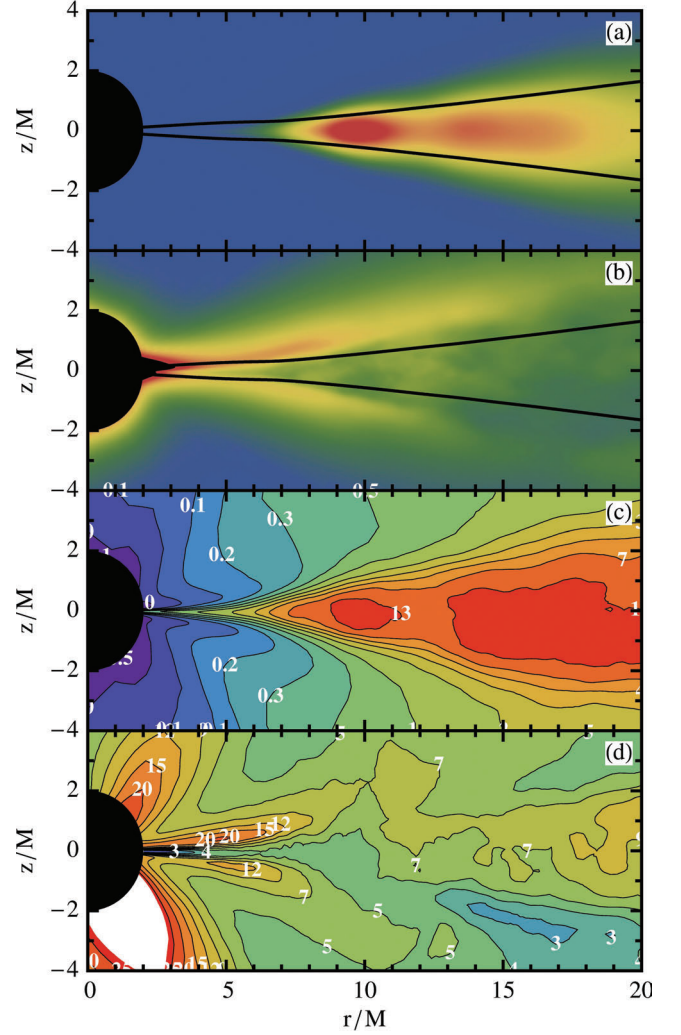
Figure 2. The evolved state of the fiducial model (A0HR07) consists of a weakly magnetized thin disc surrounded by a strongly magnetized corona. All plots show quantities that have been time-averaged over the period $12500M$ to $27350M$. Colour maps have red as highest values and blue as lowest values. Panel (a): linear colour map of rest-mass density, with solid lines showing the disc thickness $|h/r|$. Note that the rest-mass density drops off rapidly inside the ISCO. Panel (b): linear colour map of b^2 shows that a strong magnetic field is present in the corona above the equatorial disc. Panel (c): linear colour map of plasma β shows that the β values are much lower than in the initial torus. This indicates that considerable field amplification has occurred via the MRI. The gas near the equatorial plane has $\beta \sim 10$ far outside the ISCO and approaches $\beta \sim 1$ near the BH. Panel (d): linear colour map of the number of grid cells per fastest growing MRI wavelength, Q_{MRI}, shows that the MRI is properly resolved within most of the accretion flow. Note that Q_{MRI} (determined by the vertical magnetic field strength) is not expected to be large inside the plunging region where the field is forced to become mostly radial or above the disc within the corona where the field is mostly toroidal.

dynamics in this region. However, the two primary loops tend to dominate the overall evolution of the gas.

Fig. 2 shows the time-averaged solution during the quasi-steady-state period from $T_i = 12500M$ to $T_f = 27350M$. We refer to the disc during this period as being 'evolved' or 'saturated'. The evolved disc is in steady state up to $r \sim 9M$, as expected for the duration of our simulation. The rest-mass density is concentrated in the disc midplane within $\pm 2|h/r|$, while the magnetic energy
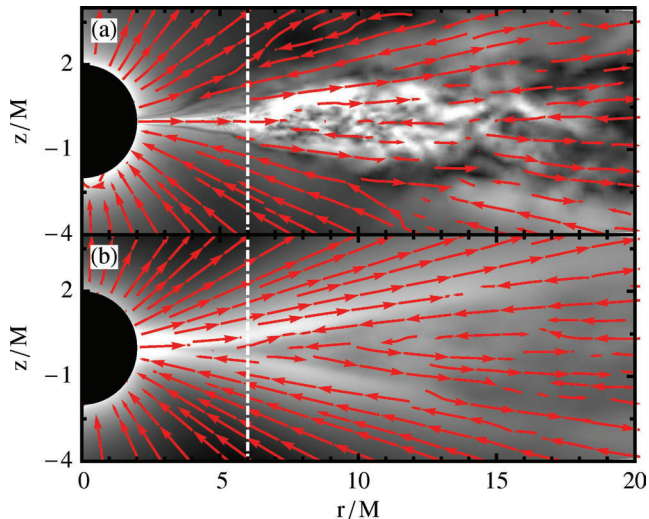
Figure 3. Magnetic field lines (red vectors) and magnetic energy density (grey-scale map) are shown for the fiducial model (A0HR07). Panel (a): snapshot of the magnetic field structure at time $27200M$ shows that the disc is highly turbulent for $r > r_{ISCO} = 6M$ and laminar for $r < r_{ISCO}$. Panel (b): time-averaged magnetic field in the saturated state shows that for $r \lesssim 9M$, viz., the region of the flow that we expect to have achieved inflow equilibrium, the geometry of the time-averaged magnetic field closely resembles that of a split-monopole. The dashed, vertical line marks the position of the ISCO.
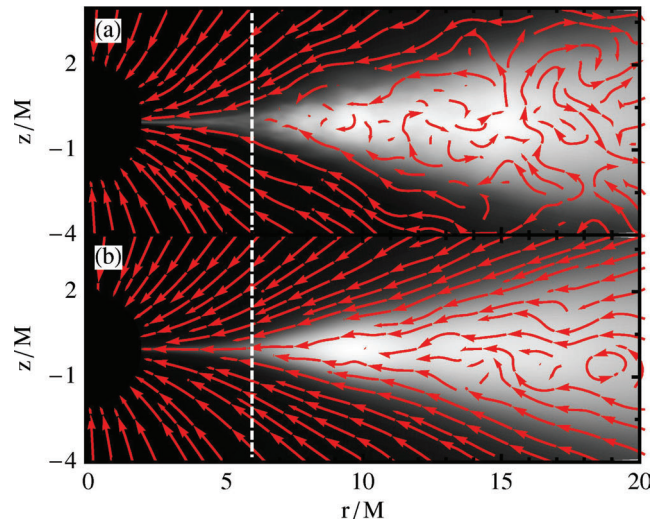

Figure 4. Flow stream lines (red vectors) and rest-mass density (grey-scale map) are shown for the fiducial model (A0HR07). Panel (a): snapshot of the velocity structure and rest-mass density at time $27200M$ clearly show MRI-driven turbulence in the interior of the disc. The rest-mass density appears more diffusively distributed than the magnetic energy density shown in Fig. 3(a). Panel (b): time-averaged streamlines and rest-mass density show that for $r \lesssim 9M$ the velocity field is mostly radial with no indication of a steady outflow. Time-averaging smooths out the turbulent fluctuations in the velocity. The dashed, vertical line marks the position of the ISCO.

density is concentrated above the disc in a corona. The MRI is properly resolved with $Q_{MRI} \approx 6$ in the disc midplane.[6] The gas in the midplane has plasma $\beta \sim 10$ outside the ISCO and $\beta \sim 1$ near the BH, indicating that the magnetic field has been amplified beyond the initial minimum of $\beta \sim 100$.

Fig. 3 shows the time-averaged structure of the magnetic field during the quasi-steady-state period. The field has a smooth split-monopole structure near and inside the ISCO. Beyond $r \sim 9M$, however, the field becomes irregular, reversing direction more than once. At these radii, the simulation has not reached inflow equilibrium.
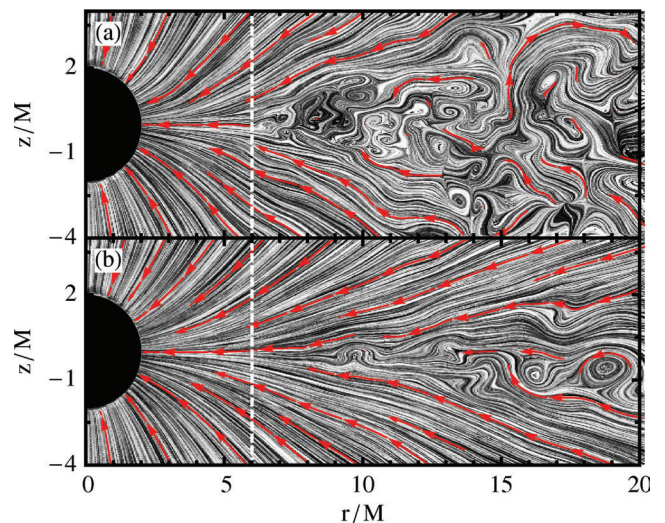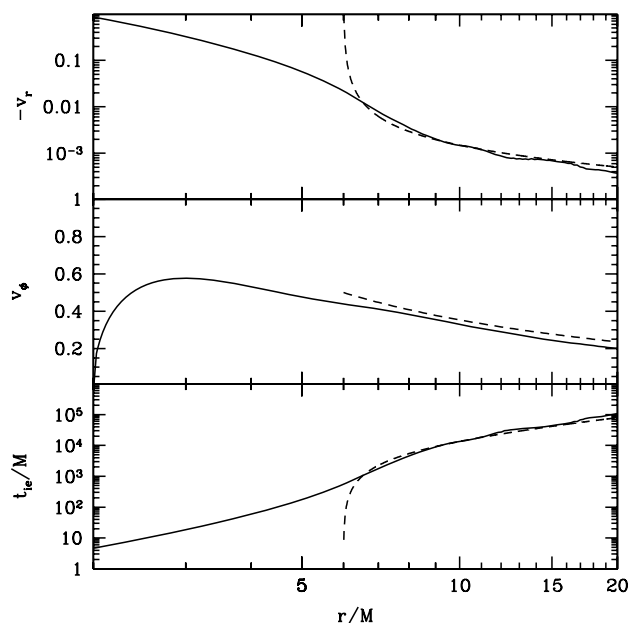
5.2 Velocities and the viscous time-scale

Fig. 4 shows the velocity structure in the evolved model. The snapshot indicates well-developed turbulence in the interior of the disc at radii beyond the ISCO ($r > 6M$), but laminar flow inside the ISCO and over most of the corona. The sudden transition from turbulent to laminar behaviour at the ISCO, which is seen also in the magnetic field (Fig. 3a), is a clear sign that the flow dynamics are quite

---

[6] Sano et al. (2004) found that having about six grid cells per wavelength of the fastest growing MRI mode during saturation leads to convergent behaviour for the electromagnetic stresses, although their determination of six cells was based upon a second-order van Leer scheme that is significantly more diffusive than our PPM scheme. Also, the (time-averaged or single time value of) vertical field is already (at any random spatial position) partially sheared by the axisymmetric MRI, and so may be less relevant than the (e.g.) maximum vertical field per unit orbital time at any given point that is not yet sheared and so represents the vertical component one must resolve. These issues imply we may only need about four cells per wavelength of the fastest growing mode (as defined by using the time-averaged absolute vertical field strength).

Figure 5. Flow stream lines are shown for the fiducial model (A0HR07). Panel (a): snapshot of the velocity structure at time $27200M$ clearly shows MRI-driven turbulence in the interior of the disc. Panel (b): time-averaged streamlines show that for $r \lesssim 9M$ the velocity field is mostly radial. The dashed, vertical line marks the position of the ISCO.

different in the two regions. Thus the ISCO clearly has an effect on the accreting gas. The time-averaged flow shows that turbulent fluctuations are smoothed out within $r \sim 9M$. Fig. 5 shows the velocity stream lines using the line integral convolution method to illustrate vector fields. This figure again confirms that the accretion flow is turbulent at radii larger than r_{ISCO} but it becomes laminar inside the ISCO, and it again shows that time-averaging smooths out turbulent fluctuations out to $r \sim 9M$.

Figure 6. The time-averaged, angle-averaged, rest-mass density-weighted three-velocities and viscous time-scale in the fiducial model (A0HR07) are compared with the NT model. Angle-averaging is performed over the disc gas lying within $\pm 2|h/r|$ of the midplane. Top panel: the orthonormal radial three-velocity (solid line), and the analytical GR estimate given in equation (B7) of Appendix B (dashed line). Agreement for $r > r_{\rm ISCO}$ between the simulation and NT model is found when we set $\alpha|h/r|^2 \approx 0.00033$. At smaller radii, the gas dynamics is no longer determined by viscosity and hence the two curves deviate. Middle panel: the orthonormal azimuthal three-velocity v_ϕ (solid line) and the corresponding Keplerian three-velocity (dashed line). Bottom panel: the inflow equilibrium time-scale $t_{\rm ie} \sim -2r/v_{\rm r}$ (solid line) of the disc gas is compared to the analytical GR thin disc estimate (dashed line). At $r \sim 9M$, we see that $t_{\rm ie} \sim 2 \times 10^4 M$. Therefore, the simulation needs to be run for this time period (which we do) before we can reach inflow equilibrium at this radius.

Fig. 6 shows components of the time-averaged velocity that are angle-averaged over $\pm 2|h/r|$ around the midplane (thick dashed lines in Fig. 8). By limiting the range of the θ integral, we focus on the gas in the disc, leaving out the corona-wind-jet. Outside the ISCO, the radial velocity from the simulation agrees well with the analytical GR estimate (equation B7 in Appendix B). By making this comparison, we found $\alpha|h/r|^2 \approx 0.00033$. For our disc thickness $|h/r| = 0.064$, this corresponds to $\alpha \approx 0.08$, which is slightly smaller than the nominal estimate $\alpha \sim 0.1$ we assumed in Section 3.5. As the gas approaches the ISCO, it accelerates rapidly in the radial direction and finally free falls into the BH. This region of the flow is not driven by viscosity and hence the dynamics here are not captured by the analytical formula.

Fig. 6 also shows the inflow equilibrium time $t_{\rm ie}$, which we take to be twice the GR version of the viscous time: $t_{\rm ie} = -2r/v_r$. This is our estimate of the time it will take for the gas at a given radius to reach the steady state. We see that, in a time of $\sim 27350M$, the total duration of our simulation, the solution can be in steady state only inside a radius of $\sim 9M$. Therefore, in the time-averaged results described below, we consider the results to be reliable only over this range of radius.

5.3 Fluxes versus time

Fig. 7 shows various fluxes versus time that should be roughly constant once inflow equilibrium has been reached. The figure shows
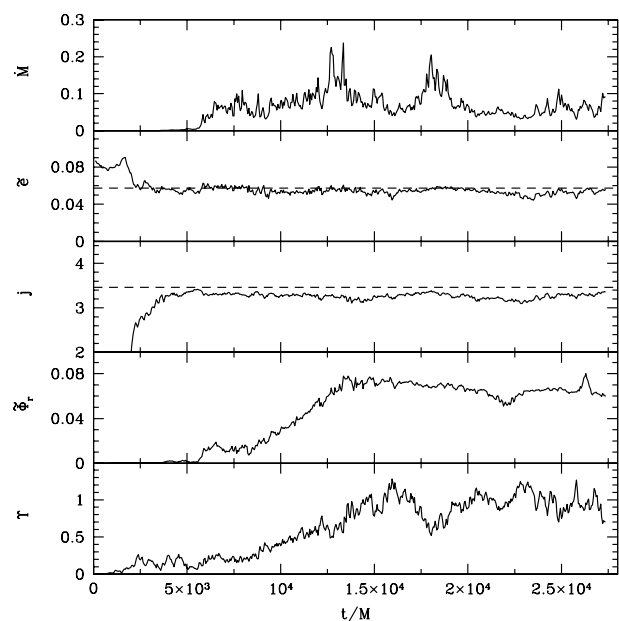
Figure 7. The figure shows for the fiducial model (A0HR07) the time-dependence at the horizon of the mass accretion rate, $\dot{M}$ (top panel); nominal efficiency, $\tilde{e}$, with dashed line showing the NT value (next panel); accreted specific angular momentum, $\jmath$, with dashed line showing the NT value (next panel); absolute magnetic flux relative to the initial absolute magnetic flux, $\tilde{\Phi}_{\rm r}$ (next panel); and dimensionless specific magnetic flux, Υ (bottom panel). All quantities have been integrated over all angles. The mass accretion rate varies by factors of up to 4 during the quasi-steady-state phase. The nominal efficiency is close to, but on average slightly lower than, the NT value. This means that the net energy loss through photons, winds and jets is below the radiative efficiency of the NT model. The specific angular momentum is clearly lower than the NT value, which implies that some stresses are present inside the ISCO. The absolute magnetic flux at the BH horizon grows until it saturates due to local force balance. The specific magnetic flux $\Upsilon \lesssim 1$, indicating that electromagnetic stresses inside the ISCO are weak and cause less than 7 per cent deviations from NT in $\jmath$.

the mass flux, $\dot{M}(r_{\rm H}, t)$, nominal efficiency, $\tilde{e}(r_{\rm H}, t)$, specific angular momentum, $\jmath(r_{\rm H}, t)$, normalized absolute magnetic flux, $\tilde{\Phi}_{\rm r}(r_{\rm H}, t)$ (normalized using the unperturbed initial total flux) and specific magnetic flux, $\Upsilon(r_{\rm H}, t)$, all measured at the event horizon ($r = r_{\rm H}$). These fluxes have been integrated over the entire range of θ from 0 to π. The quantities $\dot{M}$, $\tilde{e}$ and $\jmath$ appear to saturate already at $t \sim 7000M$. However, the magnetic field parameters saturate only at $\sim 12500M$. We consider the steady-state period of the disc to begin only after all these quantities reach their saturated values.

The mass accretion rate is quite variable, with root-mean-square (rms) fluctuations of the order of 2. The nominal efficiency $\tilde{e}$ is fairly close to the NT efficiency, while the specific angular momentum $\jmath$ is clearly below the NT value. The results indicate that torques are present within the ISCO, but do not dissipate much energy or cause significant energy to be transported out of the ISCO. The absolute magnetic flux per unit initial absolute flux, $\tilde{\Phi}_{\rm r}$, threading the BH grows to about 1 per cent, which indicates that the magnetic field strength near the BH is not just set by the amount of magnetic flux in the initial torus. This suggests our results are insensitive to the total absolute magnetic flux in the initial torus. The specific magnetic flux is $\Upsilon \approx 0.86$ on average. Magnetic stresses are relatively weak since $\Upsilon \lesssim 1$, which implies the magnetic field contributes no more than 7 per cent to deviations from NT in $\jmath$ (Gammie 1999) (see Appendix A). During the quasi-steady-state period, the small
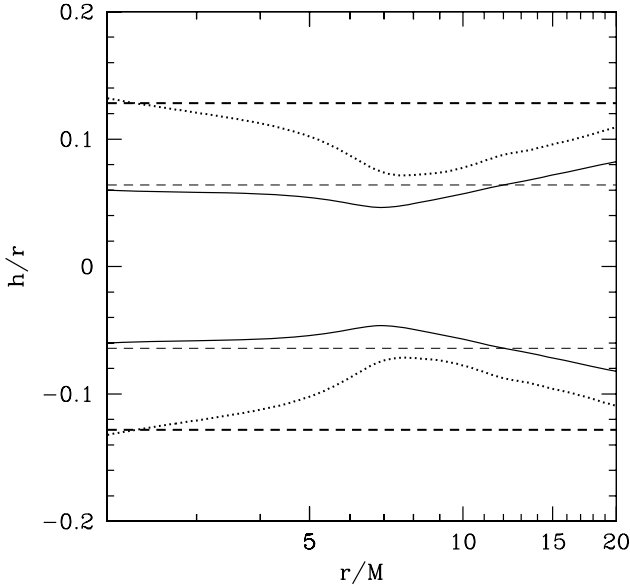
deviations from NT in $_J$ are correlated in time with the magnitude of Υ. This is consistent with the fact that the specific magnetic flux controls these deviations. Also note that $\tilde{\Phi}_r$ is roughly constant in time while Υ varies in time. This is clearly because $\dot{M}$ is varying in time and also consistent with the fact that Υ and $\dot{M}$ are anti-correlated in time.
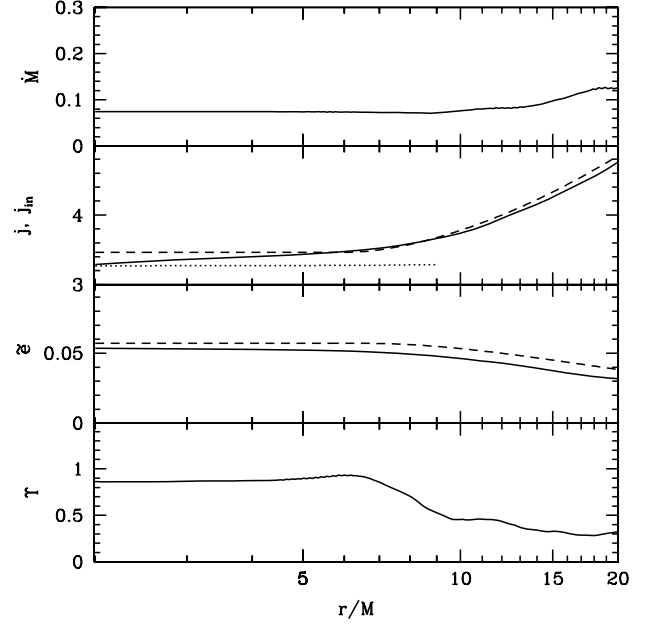
5.4 Disc thickness and fluxes versus radius

Fig. 8 shows the time-averaged disc thickness of the fiducial model as a function of radius. Both measures of thickness defined in Section 3.1 are shown; they track each other. As expected, our primary thickness measure, $|h/r|$, is the smaller of the two. This thickness measure varies by a small amount across the disc, but it is generally consistent with the following fiducial value, viz., the value $|h/r| = 0.064$ at $r = 2r_{\rm ISCO} = 12M$.

Fig. 9 shows the behaviour of various fluxes versus radius for the full θ integration range (0 to π). We see that the mass accretion rate, $\dot{M}$, and the specific angular momentum flux, $_J$, are constant up to a radius $r \sim 9M$. This is exactly the distance out to which we expect inflow equilibrium to have been established, given the inflow velocity and viscous time-scale results discussed in Section 5.2. The consistency of these two measurements gives us confidence that the simulation has truly achieved steady-state conditions inside $r = 9M$. Equally clearly, and as also expected, the simulation is not in steady state at larger radii.

The second panel in Fig. 9 shows that the inward angular momentum flux, $_{J_{\rm in}}$, agrees reasonably well with the NT prediction. It falls below the NT curve at large radii, i.e. the gas there is sub-Keplerian. This is not surprising since we have included the contribution of the corona-wind-jet gas which, being at high latitude, does not rotate at the Keplerian rate. Other quantities, described below, show a sim-

Figure 9. Mass accretion rate and specific fluxes are shown as a function of radius for the fiducial model (A0HR07). From top to bottom the panels show the following. Top panel: mass accretion rate. Second panel: the accreted specific angular momentum, $_J$ (dotted line), $_{J_{\rm in}}$ (solid line) and the NT profile (dashed line). Third panel: the nominal efficiency $\tilde{e}$ (solid line) and the NT profile (dashed line). Bottom panel: the specific magnetic flux Υ. For all quantities the integration range includes all θ. The mass accretion rate and $_J$ are roughly constant out to $r \sim 9M$, as we would expect for inflow equilibrium. The profile of $_{J_{\rm in}}$ lies below the NT value at large radii because we include gas in the slowly rotating corona. At the horizon, $_J$ and $\tilde{e}$ are modestly below the corresponding NT values. The quantity $\Upsilon \sim 0.86$ and is roughly constant out to $r \sim 6M$, indicating that electromagnetic stresses are weak inside the ISCO.

ilar effect due to the corona. At the horizon, $_{J_{\rm in}} = 3.286$, which is 5 per cent lower than the NT value. This deviation is larger than that found by S08. Once again, it is because we have included the gas in the corona-wind-jet, whereas S08 did not.

The third panel in Fig. 9 shows that the nominal efficiency $\tilde{e}$ at the horizon lies below the NT prediction. This implies that the full accretion flow (disc+corona+wind+jet) is radiatively less efficient than the NT model. However, the overall shape of the curve as a function of r is similar to the NT curve. The final panel in Fig. 9 shows the value of Υ versus radius. We see that $\Upsilon \approx 0.86$ is constant out to $r \sim 6M$. A value of $\Upsilon \sim 1$ would have led to 7 per cent deviations from NT in $_J$, and only for $\Upsilon \sim 6.0$ would deviations become 50 per cent (see Appendix A). The fact that $\Upsilon \sim 0.86 \lesssim 1$ indicates that electromagnetic stresses are weak and cause less than 7 per cent deviations from NT in $_J$. Note that one does not expect Υ to be constant[7] outside the ISCO where the magnetic field is dissipating due to MHD turbulence and the gas is forced to be nearly Keplerian despite a sheared magnetic field.

As we have hinted above, we expect large differences between the properties of the gas that accretes in the disc proper, close to the

Figure 8. The time-averaged scaleheight, $|h/r|$, versus radius in the fiducial model (A0HR07) is shown by the solid lines. The above-equator and below-equator values of the disc thickness are $|h/r| \sim 0.04$–0.06 in the inflow equilibrium region $r < 9M$. We use the specific value of $|h/r| = 0.064$ as measured at $r = 2r_{\rm ISCO}$ (light dashed lines) as a representative thickness for the entire flow. Twice this representative thickness (thick dashed lines) is used to fix the θ range of integration for averaging when we wish to focus only on the gas in the disc instead of the gas in the corona-wind-jet. The root mean square thickness $(h/r)_{\rm rms} \sim 0.07$–0.13 is shown by the dotted lines.

---

[7] We also find that the ideal MHD invariant related to the 'isorotation law' of field lines, $\Omega_{\rm F}(r) \equiv \left(\iint {\rm d}\theta {\rm d}\phi \sqrt{-g} |v^r B^\phi - v^\phi B^r| \right) / \left(\iint {\rm d}\theta {\rm d}\phi \sqrt{-g} |B^r| \right)$, is nearly Keplerian outside the ISCO and is (as predicted by the Gammie 1999 model) roughly constant from the ISCO to the horizon (see also McKinney & Gammie 2004; McKinney & Narayan 2007a).
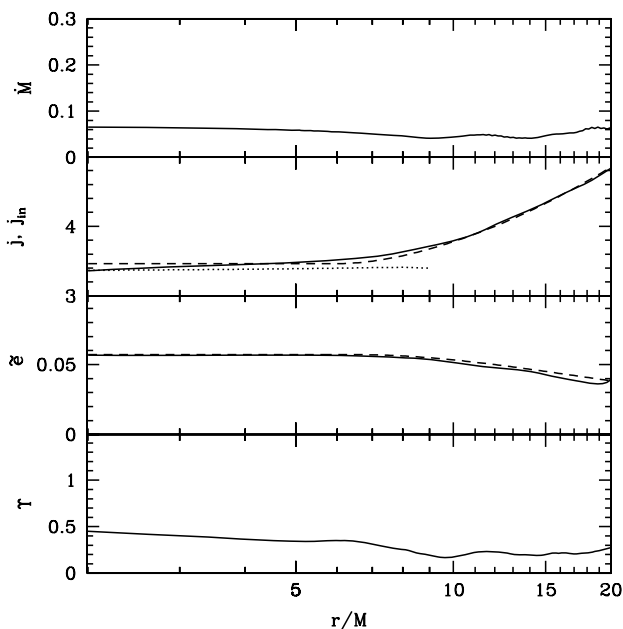
Figure 10. Similar to Fig. 9, but here the integration range only includes angles within $\pm 2|h/r| = \pm 0.128$ radians of the midplane. This allows us to focus on the disc gas. The mass accretion rate is no longer constant because streamlines are not precisely radial. The quantities shown in the second and third panels are not affected by the non-constancy of $\dot{M}$ because they are ratios of time-averaged fluxes within the equatorial region and are related to ideal MHD invariants. As compared to Fig. 9, here we find that J, J_{in} and $\tilde{e}$ closely follow the NT model. For example, $J(r_H) = 3.363$ is only 2.9 per cent less than NT. This indicates that the disc and coronal regions behave quite differently. As one might expect, the disc region behaves like the NT model, while the corona-wind-jet does not. The specific magnetic flux is even smaller than in Fig. 9 and is $\Upsilon \sim 0.45$, which indicates that electromagnetic stresses are quite weak inside the disc near the midplane.

midplane, and that which flows in the corona-wind-jet region. To focus just on the disc gas, we show in Fig. 10 the same fluxes as in Fig. 9, except that we have restricted the θ range to $\pi/2 \pm 2|h/r|$. The mass accretion rate is no longer perfectly constant for $r < 9M$. This is simply a consequence of the fact that the flow streamlines do not perfectly follow the particular constant $2|h/r|$ disc boundary we have chosen. The non-constancy of $\dot{M}$ does not significantly affect the other quantities plotted in this figure since they are all normalized by the local $\dot{M}$.

The specific angular momentum, specific energy and specific magnetic flux are clearly shifted closer to the NT values when we restrict the angular integration range. Compared to the NT value, viz., $J_{NT}(r_H) = 3.464$, the fiducial model gives $J(r_H) = 3.363$ (2.9 per cent less than NT) when integrating over $\pm 2|h/r|$ around the midplane (i.e. only over the disc gas) and gives $J(r_H) = 3.266$ (5.7 per cent less than NT) when integrating over all θ (i.e. including the corona-wind-jet). Even though the mass accretion rate through the corona-wind-jet is much lower than in the disc, still this gas contributes essentially as much to the deviation of the specific angular momentum as the disc gas does. In the case of the specific magnetic flux, integrating over $\pm 2|h/r|$ around the midplane we find $\Upsilon \approx 0.45$, while when we integrate over all angles $\Upsilon \approx 0.86$. The Gammie (1999) model of an equatorial (thin) magnetized flow within the ISCO shows that deviations in the specific angular momentum are determined by the value of Υ. We find that the measured values of Υ are able to roughly predict the measured deviations from NT in J.

In summary, a comparison of Figs 9 and 10 shows that all aspects of the accretion flow in the fiducial simulation agree much better with the NT prediction when we restrict our attention to regions close to the midplane. In other words, the gas in the disc proper, defined here as the region lying within $\pm 2|h/r|$ of the midplane, is well described by the NT model. The deviation of the angular momentum flux J_{in} or J at the horizon relative to NT is $\lesssim 3$ per cent, similar to the deviation found by S08[8], while the nominal efficiency $\tilde{e}$ agrees to within ~ 1 per cent.
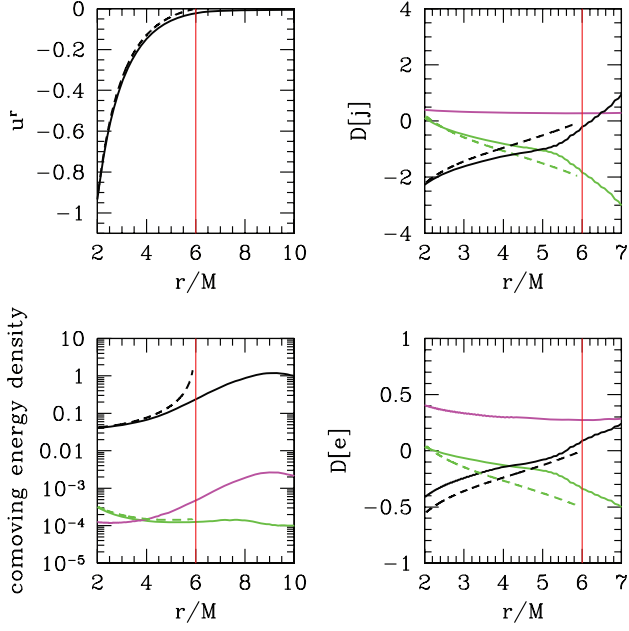
5.5 Comparison with Gammie (1999) model

Fig. 11 shows a comparison between the fiducial model and the Gammie (1999) model of a magnetized thin accretion flow within the ISCO (see also Appendix A). Quantities have been integrated within $\pm 2|h/r|$ of the midplane and time-averaged over a short period from $t = 17400M$ to $t = 18400M$. Note that time-averaging b^2, ρ_0, etc. over long periods can lead to no consistent comparable solution if the value of Υ varies considerably during the period used for averaging. Also, note that the presence of vertical stratification, seen in Figs 9 and 10 showing that Υ depends upon height, means the vertical-averaging used to obtain Υ can sometimes make it difficult to compare the simulations with the Gammie (1999) model which has no vertical stratification. In particular, using equation (24) over this time period, we find that $\Upsilon \approx 0.2\,0.3$, 0.44, 0.7, 0.8 for integrations around the midplane of, respectively, ± 0.01, ± 0.05, $\pm 2|h/r|$, $\pm \pi/4$, $\pm \pi/2$, with best matches to the Gammie model (i.e. $b^2/2$ and other quantities match) using an actual value of $\Upsilon = 0.2$, 0.33, 0.47, 0.8, 0.92. This indicates that stratification likely causes our diagnostic to underestimate the best match with the Gammie model once the integration is performed over highly stratified regions. However, the consistency is fairly good considering how much Υ varies with height.

Overall, Fig. 11 shows how electromagnetic stresses control the deviations from NT within the ISCO. The panels with $D[J]$ and $D[e]$ show how the electromagnetic flux starts out large at the ISCO and drops to nearly zero on the horizon. This indicates the electromagnetic flux has been converted into particle flux within the ISCO by ideal (non-dissipative) electromagnetic stresses.[9] The simulated magnetized thin disc agrees quite well with the Gammie solution, in contrast to the relatively poor agreement found for thick discs (McKinney & Gammie 2004). Only the single parameter Υ determines the Gammie solution, so the agreement with the value and radial dependence among multiple independent terms is a strong validation that the Gammie model is working well. Nevertheless, there are some residual deviations near the ISCO where the thermal pressure dominates the magnetic pressure. Even if deviations from NT are present right at the ISCO, the total deviation of the particle flux between the ISCO and horizon equals the deviation predicted by the Gammie (1999) model, as also found in McKinney & Gammie (2004) for thick discs. This indicates that the Gammie (1999) model accurately predicts the effects of electromagnetic stresses inward of the ISCO.

---

[8] The quantities J_{in} and J are nearly equal at the horizon in the calculations reported here whereas they were different in S08. This is because S08 used an alternate definition of J_{in}. If we had used that definition here, we would have found a deviation of ~ 2 per cent in J_{in}, just as in S08.

[9] This behaviour is just like that seen in ideal MHD jet solutions, but inverted with radius.

Figure 11. Comparison between the accretion flow (within $\pm 2|h/r|$ around the midplane) in the fiducial model (A0HR07), shown by solid lines, and the model of a magnetized thin accretion disc (inflow solution) within the ISCO by Gammie (1999), shown by dashed lines. In all cases the red vertical line shows the location of the ISCO. Top-left panel shows the radial four-velocity, where the Gammie solution assumes $u^r = 0$ at the ISCO. Finite thermal effects lead to non-zero u^r at the ISCO for the simulated disc. Bottom-left panel shows the rest-mass density (ρ_0, black line), the internal energy density (u_g, magenta line) and magnetic energy density ($b^2/2$, green line). Top-right and bottom-right panels show the per cent deviations from NT for the simulations and Gammie solution for the specific particle kinetic flux (u_μ, black line), specific enthalpy flux ($(u_g + p_g) u_\mu/\rho_0$, magenta line) and specific electromagnetic flux [$(b^2 u^r u_\mu - b^r b_\mu)/(\rho_0 u^r)$, green line], where for *j* we use $\mu = \phi$ and for e we use $\mu = t$. As usual, the simulation result for the specific fluxes is obtained by a ratio of flux integrals instead of the direct ratio of flux densities. The total specific flux is constant versus radius and is a sum of the particle, enthalpy and electromagnetic terms. This figure is comparable to fig. 10 for a thick ($|h/r| \sim 0.2$–0.25) disc in McKinney & Gammie (2004). Finite thermal pressure effects cause the fiducial model to deviate from the inflow solution near the ISCO, but the solutions rapidly converge inside the ISCO and the differences between the simulation result and the Gammie model (relative to the total specific angular momentum or energy) are less than 0.5 per cent.

Finally, note that the electromagnetic stresses within the ISCO are ideal and non-dissipative in the Gammie model. Since the flow within the ISCO in the simulation is mostly laminar leading to weak non-ideal (resistive or viscous) effects, the dissipative contribution (which could lead to radiation) can be quite small. An exception to this is the presence of extended current sheets, present near the equator within the ISCO in the simulations, whose dissipation requires a model of the (as of yet, poorly understood) rate of relativistic reconnection.

5.6 Luminosity versus radius

Fig. 12 shows radial profiles of two measures of the disc luminosity: $L(< r)/\dot{M}$, which is the cumulative luminosity inside radius *r*, and $d(L/\dot{M})/d \ln r$, which gives the local luminosity at *r*. We see that the profiles from the simulation are quite close to the NT prediction, especially in the steady-state region. As a way of measuring the
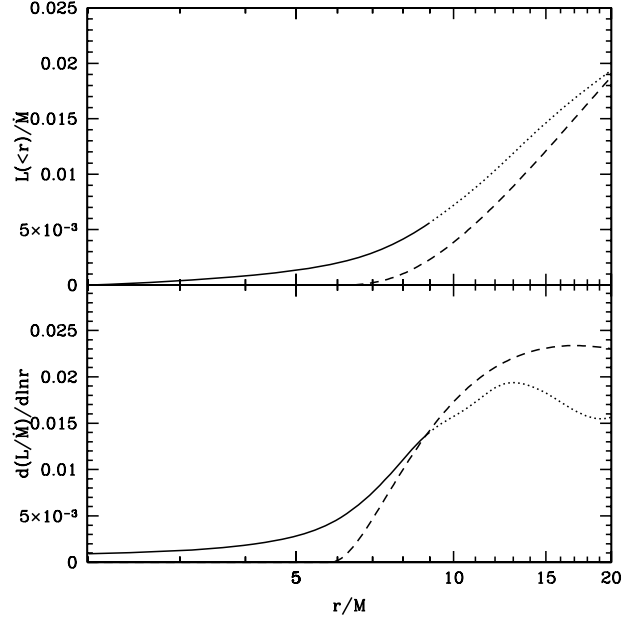

Figure 12. Luminosity per unit rest-mass accretion rate versus radius (top panel) and the logarithmic derivative of this quantity (bottom panel) are shown for the fiducial model (A0HR07). The integration includes all θ angles. The simulation result (solid lines, truncated into dotted lines outside the radius of inflow equilibrium) shows that the accretion flow emits more radiation than the NT prediction (dashed lines) at small radii. However, the excess luminosity within the ISCO is only $\tilde{L}_{\text{in}} \approx 3.5$ per cent, where $\tilde{e}[\text{NT}]$ is the NT efficiency at the horizon (or equivalently at the ISCO).

deviation of the simulation results from the NT model, we estimate what fraction of the disc luminosity is emitted inside the ISCO; recall that the NT model predicts zero luminosity here. The fiducial simulation gives $L(< r_{\text{ISCO}})/\dot{M} = 0.0021$, which is 3.5 per cent of the nominal efficiency $\tilde{e}[\text{NT}] = 0.058$ of a thin NT disc around a non-spinning BH. This shows that the excess luminosity radiated within the ISCO is quite small. The relative luminosity within the ISCO is $\tilde{L}_{\text{in}} = 3.5$ per cent and the relative luminosity within the inflow equilibrium region is $\tilde{L}_{\text{out}} = 8.0$ per cent. Hence, we conclude that, for accretion discs which are as thin as our fiducial model, viz., $|h/r| \sim 0.07$, the NT model provides a good description of the luminosity profile.

5.7 Luminosity from disc versus corona-wind-jet

The fiducial model described so far includes a tapering of the cooling rate as a function of height above the midplane, given by the function $S[\theta]$ (see equation 5). We introduced this taper in order to only cool bound [$-u_t(\rho_0 + u_g + p_g + b^2)/\rho_0 < 1$] gas and to avoid including the emission from the part of the corona-wind-jet that is prone to excessive numerical dissipation due to the low resolution used high above the accretion disc. This is a common approach that others have also taken when performing GRMHD simulations of thin discs (N09; N10). However, since our tapering function does not explicitly refer to how bound the gas is, we need to check that it is consistent with cooling only bound gas. We have explored this question by re-running the fiducial model with all parameters the same except that we turned off the tapering function altogether, i.e. we set $S[\theta] = 1$. This is the only model for which the tapering function is turned off.
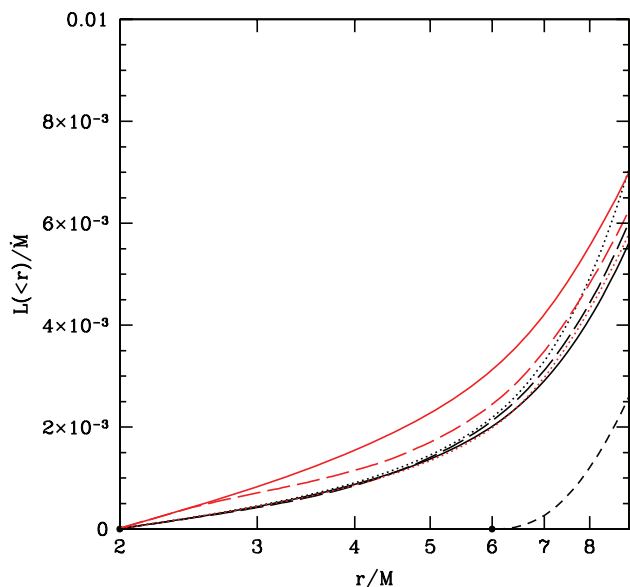
Figure 13. Enclosed luminosity versus radius for models with different cooling prescriptions and θ integration ranges. The black dashed line corresponds to the NT model. The luminosity for the fiducial model A0HR07, which includes a tapering of the cooling with disc height as described in Section 2, is shown integrated over $\pm 2|h/r|$ from the midplane (black dotted line), integrated over all bound gas (black long dashed line), and integrated over all fluid (black solid line). Essentially all the gas is bound and so the black solid and long dashed lines are indistinguishable. The red lines are for a model that is identical to the fiducial run, except that no tapering is applied to the cooling. For this model the lines are: red solid line: all angles, all fluid; red dotted line: $\pm 2|h/r|$ around the midplane; red long dashed line: all bound gas. The main result is that the luminosity from bound gas is nearly the same (especially at the ISCO) whether or not we include tapering (compare the red long dashed line and the black long dashed line).

Fig. 13 shows a number of luminosity profiles for the fiducial model and the no-tapering model. This comparison shows that, whether or not we include a taper, the results for the luminosity from all the bound gas is nearly the same. Without a tapering, there is some luminosity at high latitudes above $\pm 8|h/r|$ corresponding to emission from the low-density jet region (black solid line). This region is unbound and numerically inaccurate, and it is properly excluded when we use the tapering function. Another conclusion from the above test is that, as far as the luminosity is concerned, it does not matter much whether we focus on the midplane gas $((\pi/2) \pm 2|h/r|)$ or include all the bound gas. The deviations of the luminosity from NT in the two cases are similar – *changes* in the deviation are less than 1 per cent.

An important question to ask is whether the excess luminosity from within the ISCO is correlated with, e.g. deviations from NT in $_J$, since $D[_J]$ could then be used as a proxy for the excess luminosity. We investigate this in the context of the simulation with no tapering. For an integration over $\pm 2|h/r|$ around the midplane (which we identify with the disc component), or over all bound gas, or over all the gas (bound and unbound), the excess luminosity inside the ISCO is $\tilde{L}_{in} = 3.3$ per cent, 4.4 per cent, 5.4 per cent, and the deviation from NT in $_J$ is $D[_J] = -3.6$ per cent, -6.7 per cent, -6.7 per cent, respectively. We ignore the luminosity from unbound gas since this is mostly due to material in a very low density region of the simulation where thermodynamics is not evolved accurately. Considering the rest of the results, we see that

$D[_J]$ is 100 per cent larger when we include bound gas outside the disc compared to when we consider only the disc gas, whereas the excess luminosity increases by only 32 per cent. Therefore, when we compute $_J$ by integrating over all bound gas and then assess the deviation of the simulated accretion flow from the NT model, we strongly overestimate the excess luminosity of the bound gas relative to NT. A better proxy for the latter is the deviations from NT in $_J$ integrated only over the disc component (i.e. over $\pm 2|h/r|$ around the midplane).

Furthermore, we note that the gas that lies beyond $\pm 2|h/r|$ from the disc midplane consists of coronal gas, which is expected to be optically thin and to emit a power-law spectrum of photons. For many applications, we are not interested in this component but rather care only about the thermal blackbody-like emission from the optically thick region of the disc. For such studies, the most appropriate diagnostic from the simulations is the radiation emitted within $\pm 2|h/r|$ of the midplane. According to this diagnostic, the excess emission inside the ISCO is only $\tilde{L}_{in} = 3.4$ per cent in the model without tapering, and 3.5 per cent in the fiducial model that includes tapering.

Lastly, we consider variations in the cooling time-scale, τ_{cool}, which is another free parameter of our cooling model that we generally set to $2\pi/\Omega_K$. However, we consider one model that is otherwise identical to the fiducial model except we set τ_{cool} to be five times shorter so that the cooling rate is five times faster. We find that $\tilde{L}_{in} = 4.2$ per cent, which is slightly larger than the fiducial model with $\tilde{L}_{in} = 3.5$ per cent. Even though the cooling rate is five times faster than an orbital rate, there is only 20 per cent more luminosity from within the ISCO. This is likely due to the flow within the ISCO being mostly laminar with little remaining turbulence to drive dissipation and radiation.

6 CONVERGENCE WITH RESOLUTION AND BOX SIZE

The fiducial model described earlier was computed with a numerical resolution of $256 \times 64 \times 32$, using an azimuthal wedge of $\pi/2$. This is to be compared with the simulation described in S08, which made use of a $512 \times 128 \times 32$ grid and used a $\pi/4$ wedge. These two runs give very similar results, suggesting that the details of the resolution and wedge size are not very important. To confirm this, we have run a number of simulations with different resolutions and wedge angles. The complete list of runs is: $256 \times 64 \times 32$ with $\Delta\phi = \pi/2$ (fiducial run, model A0HR07)), $512 \times 128 \times 32$ with $\Delta\phi = \pi/4$ (S08, model C0), $256 \times 128 \times 32$ with $\Delta\phi = \pi/2$ (model C6), $256 \times 32 \times 32$ with $\Delta\phi = \pi/2$ (model C5), $256 \times 64 \times 64$ with $\Delta\phi = \pi/2$ (model C4), $256 \times 64 \times 64$ with $\Delta\phi = \pi$ (model C2), $256 \times 64 \times 16$ with $\Delta\phi = \pi/2$ (model C3) and $256 \times 64 \times 16$ with $\Delta\phi = \pi/4$ (model C1).

Fig. 14 shows the accreted specific angular momentum, $_J$, ingoing component of the specific angular momentum, $_{Jin}$, and the nominal efficiency $\tilde{e}$ as functions of radius for all the models used for convergence testing. Fig. 15 similarly shows the cumulative luminosity $L(< r)/\dot{M}$ and differential luminosity $d(L/\dot{M})/d \ln r$ as functions of radius. The overwhelming impression from these plots is that the sequence of convergence simulations agrees with one another quite well. Also, the average of all the runs matches the NT model very well; this is especially true for the steady-state region of the flow, $r < 9M$. Thus, qualitatively, we conclude that our results are well-converged.

For more quantitative comparison, Fig. 16 shows the profile of $_J$ versus r for the various models, this time with each model separately
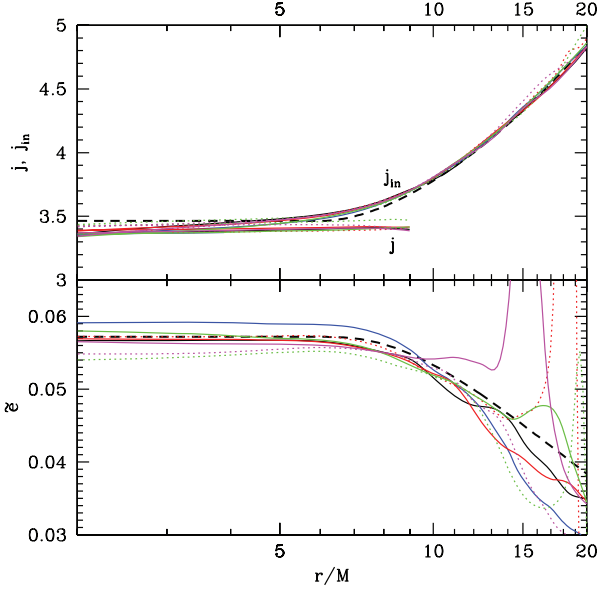
Figure 14. This plot shows J, J_{in} and $\tilde{e}$ for a sequence of simulations that are similar to the fiducial run (A0HR07), viz., $|h/r| \approx 0.07$, $a/M = 0$, but use different radial resolutions, or θ resolutions, or box sizes. The integration range in θ is over $\pm 2|h/r|$ around the midplane. Only the region of the flow in inflow equilibrium, $2M < r < 9M$, is shown in the case of J. The different lines are as follows: black dashed line: NT model; black solid line: fiducial model A0HR07; blue solid line: model C0 (S08); magenta dotted line: model C1; magenta solid line: model C2; red dotted line: model C3; red solid line: model C4; green dotted line: model C5; green solid line: model C6. Note that changes in the numerical resolution or other computational parameters lead to negligible changes in the values of J, J_{in} and $\tilde{e}$ in the region of the flow that is in inflow equilibrium, $r < 9M$. For $r \gtrsim 9M$, the flow has not achieved steady state, which explains the large deviations in $\tilde{e}$. Only the lowest resolution models are outliers.

identified. It is clear that J has converged, since there are very minor deviations from our highest resolution/largest box size to our next highest resolution/next largest box size. All other quantities, including $\tilde{e}$, J_{in} and Υ are similarly converged. The model with $N_\phi = 64$ shows slightly *less* deviations from NT in J than our other models. However, it also shows slightly higher luminosity than our other models. This behaviour is likely due to the stochastic temporal behaviour of all quantities versus time, but this could also be due to the higher ϕ-resolution causing a weaker ordered magnetic field to be present leading to weaker ideal electromagnetic stresses, smaller deviations from NT in J within the ISCO, but with the remaining turbulent field being dissipated giving a higher luminosity. The N_ϕ resolution appears to be the limit on our accuracy.

Further quantitative details are given in Table 2, where we list numerical results for all the convergence test models, with the θ integration performed over both $\pm 2|h/r|$ around the midplane and over all angles. We see that there are some trends as a function of resolution and/or $\Delta\phi$. Having only 32 cells in θ or 16 cells in ϕ gives somewhat poor results, so these runs are underresolved. However, even for these runs, the differences are not large. Note that Υ reaches a steady state much later than all other quantities, and our C? (where ? is 0 through 6) models did not run as long as the fiducial model. This explains why Υ is a bit lower for the C? models. Overall, we conclude that our choice of resolution $256 \times 64 \times 32$ for the fiducial run (A0HR07) is adequate to reach convergence.
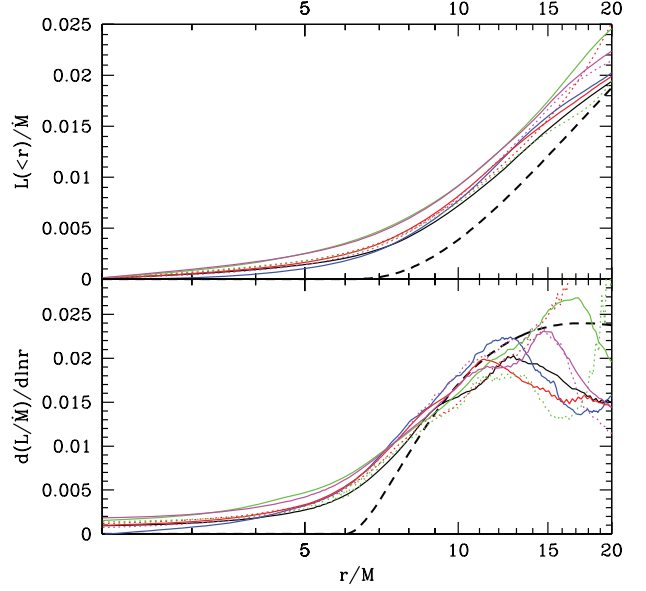
Figure 15. Similar to Fig. 14, but for the normalized luminosity, $L(< r)/\dot{M}$, and its logarithmic derivative, $d(L/\dot{M})/d \ln r$, both shown versus radius. We see that all the models used to test convergence show consistent luminosity profiles over the region that is in inflow equilibrium, $r < 9M$. The well-converged models have $\tilde{L}_{in} \lesssim 4$ per cent, which indicates only a low level of luminosity inside the ISCO.
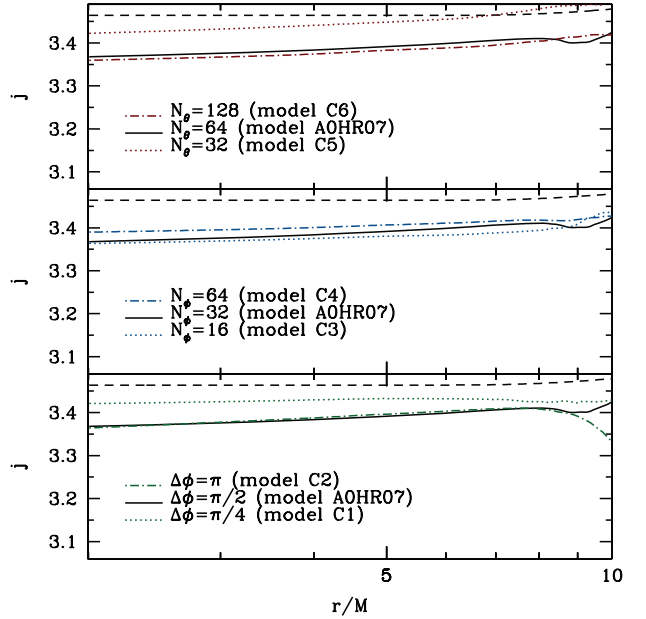
Figure 16. This is a more detailed version of Fig. 14, showing J versus r for individually labelled models. The models correspond to the fiducial resolution (solid lines), a higher resolution run (dot–dashed lines) and a lower resolution run (dotted lines). Generally, there are only minor differences between the fiducial and higher resolution models.

7 DEPENDENCE ON BLACK HOLE SPIN AND DISC THICKNESS

In addition to the fiducial model and the convergence runs described in previous sections, we have run a number of other simulations to explore the effect of the BH spin parameter a/M and the disc thickness $|h/r|$ on our various diagnostics: J, J_{in}, $\tilde{e}$, the luminosity

Table 2. Convergence study.

| Model name	$|h/r|$	$\dot{M}$	$\tilde{e}$	$D[\tilde{e}]$	J	$D[J]$	$J_{\rm in}$	$D[J_{\rm in}]$	s	$\tilde{L}_{\rm in}$	$\tilde{L}_{\rm eq}$	$100\tilde{\Phi}_{\rm r}$	Υ
$\pm 2|h/r|$													
A0HR07	0.064	0.066	0.058	−0.829	3.363	−2.913	3.355	−3.153	3.363	0.035	0.080	1.355	0.450
C0	0.052	0.064	0.059	−2.708	3.363	−2.905	3.351	−3.259	3.363	0.019	0.042	0.399	0.359
C1	0.063	0.041	0.056	2.204	3.415	−1.406	3.408	−1.621	3.415	0.034	0.072	0.584	0.223
C2	0.062	0.063	0.058	−0.699	3.360	−3.016	3.333	−3.789	3.360	0.047	0.109	0.925	0.323
C3	0.061	0.026	0.058	−1.969	3.358	−3.060	3.339	−3.610	3.358	0.039	0.087	0.727	0.449
C4	0.061	0.054	0.058	−1.406	3.385	−2.286	3.378	−2.489	3.385	0.019	0.018	0.714	0.296
C5	0.052	0.008	0.055	3.955	3.417	−1.364	3.427	−1.067	3.417	0.034	0.070	0.315	0.322
C6	0.065	0.088	0.059	−3.355	3.355	−3.155	3.333	−3.778	3.355	0.054	0.103	0.933	0.256
All θ													
A0HR07	0.064	0.074	0.054	4.723	3.266	−5.717	3.281	−5.275	3.266	0.035	0.053	6.677	0.863
C0	0.052	0.071	0.057	0.738	3.312	−4.392	3.291	−5.002	3.312	0.032	0.049	2.18	0.480
C1	0.063	0.042	0.055	3.680	3.398	−1.894	3.389	−2.178	3.398	0.037	0.062	0.940	0.142
C2	0.062	0.069	0.056	1.664	3.307	−4.541	3.262	−5.846	3.307	0.053	0.080	5.757	0.710
C3	0.061	0.029	0.057	0.893	3.325	−4.008	3.305	−4.580	3.325	0.042	0.064	1.401	0.309
C4	0.061	0.057	0.057	0.811	3.358	−3.075	3.351	−3.255	3.358	0.020	0.009	2.690	0.359
C5	0.052	0.009	0.053	7.687	3.338	−3.636	3.353	−3.218	3.338	0.039	0.059	0.726	0.243
C6	0.065	0.092	0.058	−1.813	3.334	−3.761	3.306	−4.560	3.334	0.057	0.086	5.091	0.534

and Υ. We consider four values of the BH spin parameter, viz., $a/M = 0$, 0.7, 0.9, 0.98, and four disc thicknesses, viz., $|h/r| = 0.07$, 0.1, 0.2, 0.3. We summarize here our results for this 4×4 grid of models.

Geometrically thick discs are expected on quite general grounds to deviate from the standard thin disc model. The inner edge of the disc, as measured for instance by the location of the sonic point, is expected to deviate from the ISCO, the shift scaling roughly as $|r_{\rm in} - r_{\rm ISCO}| \propto (c_{\rm s}/v_{\rm K})^2$ [$c_{\rm s}$ is sound speed, where $c_{\rm s}^2 = \Gamma p_{\rm g}/(\rho_0 + u_{\rm g} + p_{\rm g})$]. This effect is seen in hydrodynamic models of thick discs, e.g. Narayan, Kato & Honma (1997) and Abramowicz et al. (2010), where it is shown that $r_{\rm in}$ can move either inside or outside the ISCO; it moves inside when α is small and outside when α is large. In either case, these hydrodynamic models clearly show that, as $|h/r| \to 0$, i.e. as $c_{\rm s}/v_{\rm K} \to 0$, the solution always tends towards the NT model (Shafee et al. 2008b).

While the hydrodynamic studies mentioned above have driven much of our intuition on the behaviour of thick and thin discs, it is an open question whether or not the magnetic field plays a significant role. In principle, magnetic effects may cause the solution to deviate significantly from the NT model even in the limit $|h/r| \to 0$ (Krolik 1999; Gammie 1999). One of the major goals of the present paper is to investigate this question. We show in this section that, as $|h/r| \to 0$, magnetized discs do tend towards the NT model. This statement appears to be true for a range of BH spins. We also show that the specific magnetic flux Υ inside the ISCO decreases with decreasing $|h/r|$ and remains quite small. This explains why the magnetic field does not cause significant deviations from NT in thin discs.

Fig. 17 shows the specific angular momentum, J, and the ingoing component of this quantity, $J_{\rm in}$, versus radius for the 4×4 grid of models. The θ integral has been taken over $\pm 2|h/r|$ around the midplane in order to focus on the equatorial disc properties. The value of J is roughly constant out to a radius well outside the ISCO, indicating that we have converged solutions in inflow equilibrium extending over a useful range of radius. As discussed in Section 3.5, inflow equilibrium is expected within $r/M = 9, 7, 5.5, 5$, respectively, for $a/M = 0, 0.7, 0.9, 0.98$. This is roughly consistent with the radius out to which the quantity J (integrated over all angles) is constant, and this motivates why in all such plots we only show J over the region where the flow is in inflow equilibrium. The
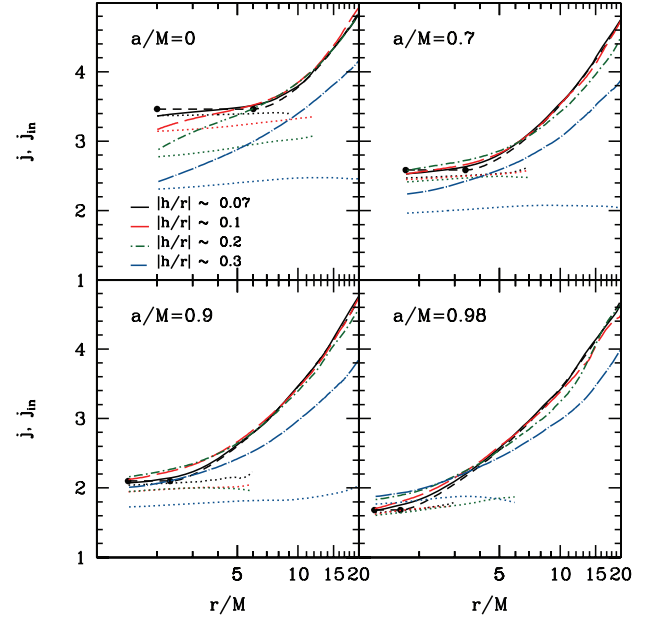
Figure 17. The net accreted specific angular momentum, J (the nearly horizontal dotted lines), and the ingoing component of this quantity, $J_{\rm in}$ (the sloping curved lines), as a function of radius for the 4×4 grid of models. Each panel corresponds to a single BH spin, $a/M = 0, 0.7, 0.9$ or 0.98, and shows models with four disc thicknesses, $|h/r| \approx 0.07, 0.1, 0.2, 0.3$ (see legend). The θ integral has been taken over $\pm 2|h/r|$ around the midplane. In each panel, the thin dashed black line, marked by two circles which indicate the location of the horizon and the ISCO, shows the NT solution for $J_{\rm in}$. As expected, we see that thicker discs exhibit larger deviations from NT. However, as a function of spin, there is no indication that deviations from NT become any larger for larger spins. In the case of the thinnest models with $|h/r| \approx 0.07$, the NT model works well for gas close to the midplane for all spins.

four panels in Fig. 17 show a clear trend, viz., deviations from NT are larger for thicker discs, as expected. Interestingly, for higher BH spins, the relative deviations from NT actually decrease.

Fig. 18 shows the nominal efficiency, $\tilde{e}$, as a function of radius for the 4×4 grid of models. Our thickest disc models ($|h/r| \approx$
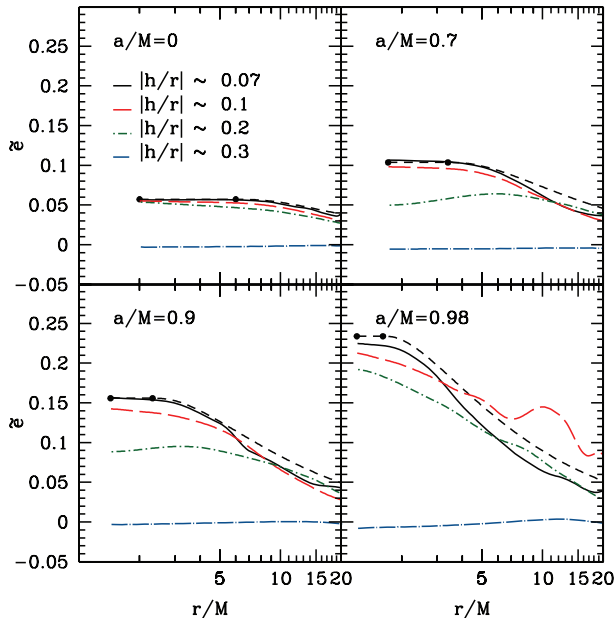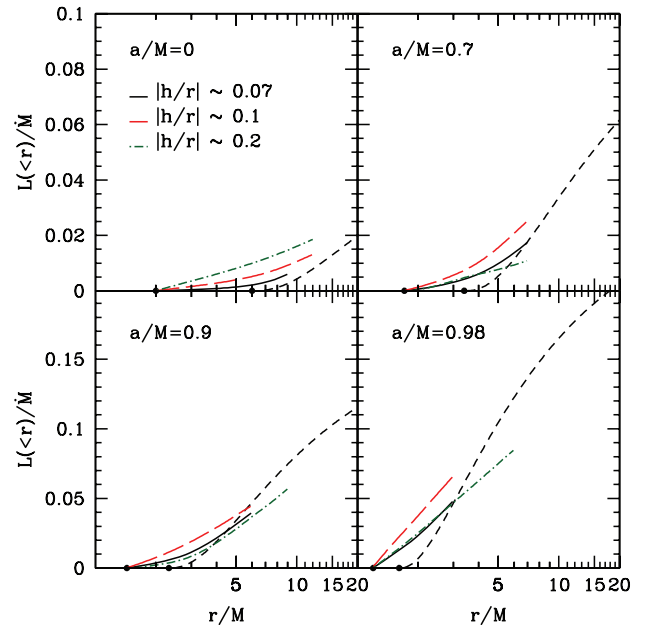
Figure 18. Similar to Fig. 17, but for the nominal efficiency, $\tilde{e}$. For thin ($|h/r| \lesssim 0.1$) discs, the results are close to NT for all BH spins. As expected, the thicker models deviate significantly from NT. In part this is because the ad hoc cooling function we use in the simulations is less accurate for thick discs, and in part because the models with $|h/r| \approx 0.3$ have no cooling and start with marginally bound/unbound gas that implies $\tilde{e} \sim 0$. The $a/M = 0.98$ models show erratic behaviour at large radii where the flow has not achieved inflow equilibrium.

0.3) do not include cooling, so the efficiency shown is only due to losses by a wind-jet. We see that the efficiency is fairly close to the NT value for all four thin disc simulations with $|h/r| \sim 0.07$; even in the worst case, viz., $a/M = 0.98$, the deviation from NT is only ~5 per cent. In the case of thicker discs, the efficiency shows larger deviations from NT and the profile as a function of radius also looks different. For models with $|h/r| \approx 0.3$, there is no cooling so large deviations are expected.

Fig. 19 shows the luminosity, $L(< r)/\dot{M}$, versus radius for our 4×4 grid of models, focusing just on the region that has reached inflow equilibrium. The luminosity is estimated by integrating over all θ angles. Our thickest disc models ($|h/r| \approx 0.3$) do not include cooling and so are not plotted. The various panels show that, as $|h/r| \rightarrow 0$, the luminosity becomes progressively closer to the NT result in the steady-state region of the flow near and inside the ISCO. Thus, once again, we conclude that the NT luminosity profile is valid for geometrically thin discs even when the accreting gas is magnetized.

A figure (not shown) that is similar to Fig. 17 but for the specific magnetic flux indicates that $\Upsilon \leq 1$ within $\pm 2|h/r|$ near the ISCO for all BH spins and disc thicknesses. For our thinnest models, $\Upsilon \leq 0.45$, for which the model of Gammie (1999) predicts that the specific angular momentum will deviate from NT by less than 1.9 per cent, 3.0 per cent, 3.8 per cent, 4.2 per cent for BH spins $a/M = 0, 0.7, 0.9, 0.98$, respectively (see Appendix A). The numerical results from the simulations show deviations from NT that are similar to these values. Thus, overall, our results indicate that electromagnetic stresses are weak inside the ISCO for geometrically thin discs.

Finally, for all models we look at plots (not shown) of $M(< r)$ (mass enclosed within radius), $\dot{M}(r)$ (total mass accretion

Figure 19. Similar to Fig. 17, but for the normalized luminosity, $L(< r)/\dot{M}$. For thin discs, the luminosity deviates only slightly from NT near and inside the ISCO. There is no strong evidence for any dependence on the BH spin. The region at large radii has not reached inflow equilibrium and is not shown.

rate versus radius) and $[h/r](r)$ (disc scaleheight versus radius). We find that these are consistently flat to the same degree and to the same radius as the quantity $_J(r)$ is constant as shown in Fig. 17. This further indicates that our models are in inflow equilibrium out to the expected radius.

7.1 Scaling laws versus a/M and $|h/r|$

We now consider how the magnitude of $_J$, $\tilde{e}$, $L(< r_{\rm ISCO})$ and Υ scales with disc thickness and BH spin. Table 3 lists numerical results corresponding to θ integrations over $\pm 2|h/r|$ around the midplane and over all angles.[10] Fig. 20 shows selected results corresponding to models with a non-rotating BH for quantities integrated over $\pm 2|h/r|$. We see that the deviations of various diagnostics from the NT values scale roughly as $|h/r|$. In general, the deviations are quite small for the thinnest model with $|h/r| \approx 0.07$.

Next, we consider fits of our simulation data as a function of BH spin and disc thickness to reveal if, at all, these two parameters control how much the flow deviates from NT. In some cases we directly fit the simulation results instead of their deviations from NT, since for thick discs the actual measurement values can saturate independent of thickness leading to large non-linear deviations from NT. Before making the fits, we ask how quantities might scale with a/M and $|h/r|$. With no disc present, the rotational symmetry forces any scaling to be an even power of BH spin (McKinney & Gammie 2004). However, the presence of a rotating disc breaks this symmetry, and any accretion flow properties, such as deviations from NT's model, could depend linearly upon a/M (at least for small spins). This motivates performing a linear fit in a/M. Similarly, the

---

[10] Some thicker disc models without cooling show small or slightly negative efficiencies, $\tilde{e}$, which signifies the accretion of weakly unbound gas. This can occur when a magnetic field is inserted into a weakly bound gas in hydrostatic equilibrium.

Table 3. BH spin and disc thickness study.

| Model name	$|h/r|$	$\dot{M}$	$\tilde{e}$	$D[\tilde{e}]$	J	$D[J]$	$J_{\rm in}$	$D[J_{\rm in}]$	s	$\tilde{L}_{\rm in}$	$\tilde{L}_{\rm eq}$	$100\tilde{\Phi}_{\rm r}$	Υ
$\pm 2|h/r|$													
A0HR07	0.064	0.066	0.058	−0.829	3.363	−2.913	3.355	−3.153	3.363	0.035	0.080	1.355	0.450
A7HR07	0.065	0.050	0.107	−2.899	2.471	−4.465	2.527	−2.294	1.220	0.048	0.084	0.919	0.393
A9HR07	0.054	0.045	0.156	−0.157	2.042	−2.762	2.074	−1.213	0.523	0.041	0.082	0.455	0.218
A98HR07	0.059	0.013	0.225	3.897	1.643	−2.335	1.679	−0.199	0.124	0.069	0.127	0.276	0.228
A0HR1	0.12	4.973	0.056	1.470	3.138	−9.424	3.162	−8.724	3.138	0.084	0.134	2.976	0.871
A7HR1	0.09	2.443	0.099	4.808	2.446	−5.447	2.524	−2.409	1.184	0.060	0.108	0.909	0.406
A9HR1	0.13	2.133	0.142	9.014	1.947	−7.261	2.124	1.157	0.402	0.068	0.107	1.064	0.466
A98HR1	0.099	2.372	0.213	8.810	1.626	−3.393	1.703	1.200	0.084	0.062	0.112	0.451	0.254
A0HR2	0.18	48.286	0.055	4.134	2.774	−19.916	2.872	−17.098	2.774	0.167	0.235	2.518	1.235
A7HR2	0.16	31.665	0.049	52.330	2.412	−6.736	2.576	−0.425	1.081	0.050	0.034	0.919	0.631
A9HR2	0.21	40.603	0.090	41.922	1.946	−7.315	2.155	2.624	0.309	0.011	−0.026	0.795	0.557
A98HR2	0.18	29.410	0.191	18.496	1.588	−5.650	1.870	11.117	0.001	0.052	0.068	0.651	0.459
A0HR3	0.350	44.066	−0.003	104.582	2.309	−33.331	2.408	−30.473	2.309	0.000	−0.049	3.039	1.182
A7HR3	0.34	41.045	−0.007	106.384	1.967	−23.970	2.236	−13.549	0.557	0.000	−0.060	1.956	0.746
A9HR3	0.341	35.852	−0.001	100.582	1.722	−17.999	1.998	−4.832	−0.080	0.000	−0.073	1.437	0.543
A98HR3	0.307	24.486	−0.015	106.206	1.783	5.987	1.886	12.102	−0.205	0.000	−0.104	0.369	0.246
All θ													
A0HR07	0.064	0.074	0.054	4.723	3.266	−5.717	3.281	−5.275	3.266	0.035	0.053	6.677	0.863
A7HR07	0.065	0.065	0.093	10.132	2.282	−11.776	2.511	−2.933	1.012	0.040	0.040	8.496	1.156
A9HR07	0.054	0.060	0.135	13.294	1.860	−11.404	2.209	5.222	0.303	0.035	0.031	8.945	1.299
A98HR07	0.059	0.021	0.171	26.735	1.559	−7.348	1.799	6.905	−0.065	0.048	0.039	2.460	0.626
A0HR1	0.12	6.036	0.053	6.579	2.908	−16.046	2.980	−13.961	2.908	0.087	0.110	8.880	1.247
A7HR1	0.09	2.907	0.093	10.343	2.344	−9.376	2.457	−4.988	1.074	0.068	0.093	2.295	0.525
A9HR1	0.13	2.777	0.128	17.577	1.823	−13.164	2.069	−1.449	0.254	0.066	0.075	4.256	0.735
A98HR1	0.099	3.235	0.197	15.950	1.425	−15.291	1.880	11.744	−0.149	0.078	0.094	6.599	1.349
A0HR2	0.18	59.025	0.050	12.631	2.465	−28.830	2.596	−25.067	2.465	0.164	0.197	5.798	1.771
A7HR2	0.16	41.327	0.046	55.244	2.186	−15.499	2.394	−7.453	0.851	0.045	0.015	2.679	0.923
A9HR2	0.21	53.746	0.085	45.564	1.739	−17.164	2.058	−2.001	0.092	0.012	−0.031	3.799	1.093
A98HR2	0.18	43.815	0.154	34.174	1.411	−16.120	1.876	11.497	−0.247	0.045	0.033	2.072	0.887
A0HR3	0.350	49.207	−0.004	106.180	2.128	−38.572	2.220	−35.919	2.128	0.000	−0.049	4.724	1.331
A7HR3	0.34	47.146	−0.007	107.191	1.788	−30.878	2.065	−20.166	0.377	0.000	−0.060	3.433	0.952
A9HR3	0.341	42.733	−0.004	102.370	1.530	−27.117	1.869	−10.977	−0.276	0.000	−0.073	2.652	0.914
A98HR3	0.307	30.293	−0.014	105.873	1.597	−5.105	1.655	−1.624	−0.390	0.000	−0.104	0.668	0.273

thickness relates to a dimensionless speed: $c_{\rm s}/v_{\rm K} \sim |h/r|$, while there are several different speeds in the accretion problem that could force quantities to have an arbitrary dependence on $|h/r|$. Although, in principle, deviations might scale as some power of $|h/r|$, we assume here a linear scaling $\propto |h/r|$. This choice is driven partly by simplicity and partly by Fig. 20 which shows that the simulation results agree well with this scaling.

These rough arguments motivate obtaining explicit scaling laws for a quantity's deviations from NT as a function of a/M and $|h/r|$. For all quantities we use the full 4×4 set of models, except for the luminosity and efficiency we exclude the two thickest models in order to focus on the luminosity for thin discs with cooling. We perform a linear least-squares fit in both a/M and $|h/r|$, and we report the absolute per cent difference between the upper 95 per cent confidence limit (C_+) and the best-fitting parameter value (f) given by $E = 100|C_+ - f|/|f|$. Note that if $E > 100$ per cent, then the best-fitting value is no different from zero to 95 per cent confidence (such parameter values are not reported). After the linear fit is provided, the value of E is given for each parameter in order of appearance in the fit. Only the statistically significant digits are shown.

First, we consider how electromagnetic stresses depend upon a/M and $|h/r|$. Gammie (1999) has shown that the effects of electromagnetic stresses are tied to the specific magnetic flux, Υ, and that for $\Upsilon \lesssim 1$ there are weak electromagnetic stresses causing only

minor deviations (less than 12 per cent for J across all BH spins) from NT. Let us consider how Υ should scale with $|h/r|$, where $\Upsilon = \sqrt{2}(r/M)^2 B^r/(\sqrt{-(r/M)^2 \rho_0 u^r})$ in the equatorial plane and is assumed to be constant from the ISCO to the horizon. For simplicity, let us study the case of a rapidly rotating BH. First, consider the boundary conditions near the ISCO provided by the disc, where $c_{\rm s}/v_{\rm K} \sim |h/r|$ and the Keplerian rotation speed reaches $v_{\rm K} \sim 0.5$. This implies $c_{\rm s} \sim 0.5|h/r|$. Secondly, consider the flow that connects the ISCO and the horizon. The gas in the disc beyond the ISCO has $\beta \sim (c_{\rm s}/v_{\rm A})^2 \sim 10$, but reaches $\beta \sim 1$ inside the ISCO in any GRMHD simulations of turbulent magnetized discs, which gives that $c_{\rm s} \sim v_{\rm A}$. Thus, $v_{\rm A} \sim 0.5|h/r|$. Finally, notice that $\Upsilon \sim 1.4 B^r/\sqrt{\rho_0}$ at the horizon where $u^r \sim -1$ and $r = M$. The Keplerian rotation at the ISCO leads to a magnetic field with orthonormal radial ($|B_r| \sim |B^r|$) and toroidal ($|B_\phi|$) components with similar values near the ISCO and horizon, giving $|B^r| \sim |B_r| \sim |B_\phi| \sim |b|$ and so $\Upsilon \sim 1.4|b|/\sqrt{\rho_0}$. Further, the Alfvén three-speed is $v_{\rm A} = |b|/\sqrt{b^2 + \rho_0 + u_{\rm g} + p_{\rm g}} \sim |b|/\sqrt{\rho_0}$ in any massive disc, so that $\Upsilon \sim 1.4 \, v_{\rm A} \sim 0.7|h/r|$ for a rapidly rotating BH. Extending these rough arguments to all BH spins at a fixed disc thickness also gives that $\Upsilon \propto -0.8(a/M)$ for $a/M \lesssim 0.7$. These arguments demonstrate three points: (1) $\Upsilon \gg 1$ gives $b^2/\rho_0 \gg 1$, implying a force-free magnetosphere instead of a massive accretion disc; (2) $\Upsilon \propto |h/r|$ and (3) $\Upsilon \propto -(a/M)$. Since the local condition for the magnetic field ejecting mass is $b^2/\rho_0 \gg 1$ (see
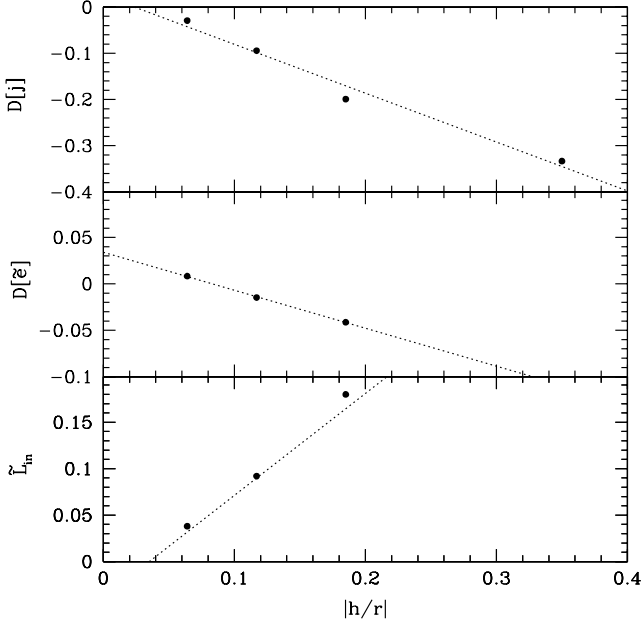
Figure 20. The relative difference between $_J$ in the simulation and in the NT model (top panel), the relative difference between the nominal efficiency, $\tilde{e}$, and the NT value (middle panel), and the luminosity inside the ISCO normalized by the net radiative efficiency of the NT model, $\tilde{L}_{\rm in}$ (bottom panel), where $\tilde{e}$[NT] has been evaluated at the horizon (equivalently at the ISCO). There is a rough linear dependence on $|h/r|$ for all quantities, where a linear fit is shown as a dotted line in each panel. Note that the thicker disc models are not expected to behave like NT, and actually have $_J$ roughly similar across all spins. For $|h/r| \approx 0.07$, the excess luminosity from within the ISCO is less than 4 per cent of the total NT efficiency.

e.g. Komissarov & Barkov 2009), this shows that $\Upsilon \sim 1$ defines a boundary that the disc component of the flow cannot significantly pass beyond without eventually incurring disruption by the strong magnetic field within the disc.

We now obtain the actual fit, which for an integration over $\pm 2|h/r|$ gives

$$\Upsilon \approx 0.7 + \left|\frac{h}{r}\right| - 0.6\frac{a}{M}, \qquad (37)$$

with $E = 33$ per cent, 70 per cent, 40 per cent, indicating a reasonable fit. There is essentially 100 per cent confidence in the sign of the first and third parameters and 98 per cent confidence in the sign of the second parameter. This fit is consistent with our basic analytical estimate for the scaling. Since most likely $\Upsilon \leq 0.9$ in the limit that $|h/r| \to 0$ across all BH spins, the electromagnetic stresses are weak and cause less than 12 per cent deviation from NT in $_J$. This means that the NT solution is essentially recovered for magnetized thin discs. For an integration over all angles, $\Upsilon \approx 1$ with $E = 35$ per cent, and there is no statistically significant trend with disc thickness or BH spin. The value of $\Upsilon \sim 1$ is consistent with the presence of the highly magnetized corona-wind-jet above the disc component (McKinney & Gammie 2004).

Next, we consider whether our simulations can determine the equilibrium value of the BH spin as a function of $|h/r|$. The spin evolves as the BH accretes mass, energy and angular momentum, and it can stop evolving when these come into a certain balance leading to $d(a/M)/dt = 0$ (see equation 15). In spin equilibrium, the spin-up parameter $s = _J - 2(a/M)e$ has $s = 0$ and solving for a gives the equilibrium spin $a_{\rm eq}/M = _J/(2e)$. For the NT solution, s is fairly linear for $a/M > 0$ and $a_{\rm eq}/M = 1$. In Appendix A, we

note that for $\Upsilon \sim 0.2$–1 that the deviations from NT roughly scale as Υ. Since $\Upsilon \propto |h/r|$, one expects s to also roughly scale with $|h/r|$. This implies that deviations from NT in the spin equilibrium should scale as $|h/r|$. Hence, one should have $1 - a_{\rm eq}/M \propto |h/r|$.

Now we obtain the actual fit. We consider two types of fits. In one case, we fit s (with fluxes integrated over all angles) and solve $s = 0$ for $a_{\rm eq}/M$. This gives

$$s \approx 3.2 - 2.5\left|\frac{h}{r}\right| - 2.9\frac{a}{M}, \qquad (38)$$

with $E = 8$ per cent, 36 per cent, 8 per cent, indicating quite a good fit. There is an essentially 100 per cent confidence for the sign of all parameters, indicating the presence of well-defined trends. Solving the equation $s = 0$ for a/M shows that the spin equilibrium value, $a_{\rm eq}/M$, is given by

$$1 - \frac{a_{\rm eq}}{M} \approx -0.08 + 0.8\left|\frac{h}{r}\right|. \qquad (39)$$

In the other case, we fit $_J/(2e)$ and re-solve for $a_{\rm eq}/M$, which gives directly

$$1 - \frac{a_{\rm eq}}{M} \approx -0.10 + 0.9\left|\frac{h}{r}\right|, \qquad (40)$$

with $E = 9$ per cent, 38 per cent with a 99.99 per cent confidence in the sign of the $|h/r|$ term. Both of these procedures give a similar fit (the first fit is statistically better) and agree within statistical errors, which indicates a linear fit is reasonable. For either fit, one should set $a_{\rm eq}/M = 1$ when the above formula gives $a_{\rm eq}/M > 1$ to be consistent with our statistical errors and the correct physics. Note that the overshoot $a_{\rm eq}/M > 1$ in the fit is consistent with a linear extrapolation of the NT dependence of s for $a/M > 0$, which also overshoots in the same way due to the progressively non-linear behaviour of s above $a/M \approx 0.95$.

These spin equilibrium fits imply that, within our statistical errors, the spin can reach $a_{\rm eq}/M \to 1$ as $|h/r| \to 0$. Thus, our results are consistent with NT by allowing maximal BH spin for thin discs.[11] Our results are also roughly consistent with the thick disc one-loop field geometry study by Gammie et al. (2004). Using our definition of disc thickness, their model had $|h/r| \sim 0.2$–0.25 and they found $a_{\rm eq}/M \sim 0.9$, which is roughly consistent with our scaling law. The fit is also consistent with results for even thicker discs ($|h/r| \sim 0.4$ near the horizon) with $a_{\rm eq}/M \sim 0.8$ (Abramowicz, Jaroszynski & Sikora 1978; Popham & Gammie 1998).

Overall, the precise scaling relations given for Υ and $a_{\rm eq}$ should be considered as suggestive and preliminary. More work is required to test the convergence and generality of the actual coefficients. While we explicitly tested convergence for the $a/M = 0$ fiducial model, the other a/M were not tested as rigorously. A potential issue is that we find the saturated state has fewer cells per (vertical magnetic field) fastest growing mode for the axisymmetric MRI in models with $a/M = 0.9, 0.98$ than in models with $a/M = 0, 0.7$ due to the relative weakness of the vertical field in the saturated state for the high spin models. However, both the rough analytical arguments and the numerical solutions imply that electromagnetic stresses scale somewhat linearly with BH spin. This consistency suggests that many measurements for the simulations, such as Υ and $a_{\rm eq}$, may be independent of smallness of the vertical field. This fact could be due to these quantities being only directly related to the radial and toroidal magnetic field strengths rather than the vertical

---

[11] Here, we do not include BH spin changes by photon capture, which gives a limit of $a_{\rm eq}/M = 0.998$ (Thorne 1974).

magnetic field strength. Further, our thick disc models resolve the axisymmetric MRI better than the thinnest disc model. This suggests that the scaling of Υ and $a_{\rm eq}$ with disc thickness may be a robust result.

Lastly, we consider how the specific angular momentum, nominal efficiency and luminosity from within the ISCO deviate from NT as functions of spin and thickness. Overall, fitting these quantities does not give very strong constraints on the actual parameter values, but we can state the confidence level of any trends. For each of $\tilde{e}$, $_{J}$, $_{J{\rm in}}$ and $\tilde{L}_{\rm in}$, the deviation from NT as $|h/r| \rightarrow 0$ is less than 5 per cent with a confidence of 95 per cent. For $_{J}$ integrated over $\pm 2|h/r|$, $D[_{J}]$ decreases with $|h/r|$ and increases with a/M both with 99 per cent confidence. When integrating $_{J}$ over all angles, $D[_{J}]$ only decreases with $|h/r|$ to 99 per cent confidence. For $_{J{\rm in}}$ integrated over $\pm 2|h/r|$, $D[_{J{\rm in}}]$ only increases with a/M with 99.8 per cent confidence and only decreases with $|h/r|$ with 97 per cent confidence. When integrating $_{J{\rm in}}$ over all angles, $D[_{J{\rm in}}]$ only increases with a/M to essentially 100 per cent confidence and only decreases with $|h/r|$ to 99.8 per cent confidence. For $\tilde{e}$ integrated over $\pm 2|h/r|$, $D[\tilde{e}]$ only increases with $|h/r|$ with 98 per cent confidence with no significant trend with a/M. When integrating $\tilde{e}$ over all angles, $D[\tilde{e}]$ only increases with a/M with 95 per cent confidence with no significant trend with $|h/r|$. For $\tilde{L}_{\rm in}$, there is a 98 per cent confidence for this to increase with $|h/r|$ with no significant trend with a/M. Overall, the most certain statement that can be made is that our results are strongly consistent with all deviations from NT becoming less than a few per cent in the limit that $|h/r| \rightarrow 0$ across the full range of BH spins.

8 THIN DISCS WITH VARYING MAGNETIC FIELD GEOMETRY

We now consider the effects of varying the initial field geometry. Since the magnetic field can develop large-scale structures that do not act like a local scalar viscosity, there could in principle be long-lasting effects on the accretion flow properties as a result of the initial field geometry. This is especially a concern for geometrically thin discs, where the one-loop field geometry corresponds to a severely squashed and highly organized field loop bundle with long-range coherence in the radial direction, whereas our fiducial four-loop model corresponds to nearly circular loops which impose much less radial order on the MRI-driven turbulence. To investigate this question we have simulated a model similar to our fiducial run except that we initialized the gas torus with a one-loop type field geometry instead of our usual multi-loop geometry.

Fig. 21 shows the radial dependence of $_{J}$, $_{J{\rm in}}$, $\tilde{e}$ and Υ for the two field geometries under consideration, and Table 4 reports numerical estimates of various quantities at the horizon. Consider first the solid lines (four-loop fiducial run) and dotted lines (one-loop run) in Fig. 21, both of which correspond to integrations in θ over $\pm 2|h/r|$ around the midplane. The simulation with four-loops is clearly more consistent with NT than the one-loop simulation. The value of $_{J}$ at the horizon in the four-loop model deviates from NT by -2.9 per cent. Between the times of $12900M$ and $17300M$, the one-loop model deviates by -5.6 per cent, while at late time over the saturated period the one-loop model deviates by -7.2 per cent. The long-dashed lines show the effect of integrating over all θ for the one-loop model. This introduces yet another systematic deviation from NT (as already noted in Section 5.7); now the net deviation of $_{J}$ becomes -10.7 per cent for times $12900M$ to $17300M$ and becomes -15.8 per cent for the saturated state. Overall, this implies that the assumed initial field geometry has a considerable
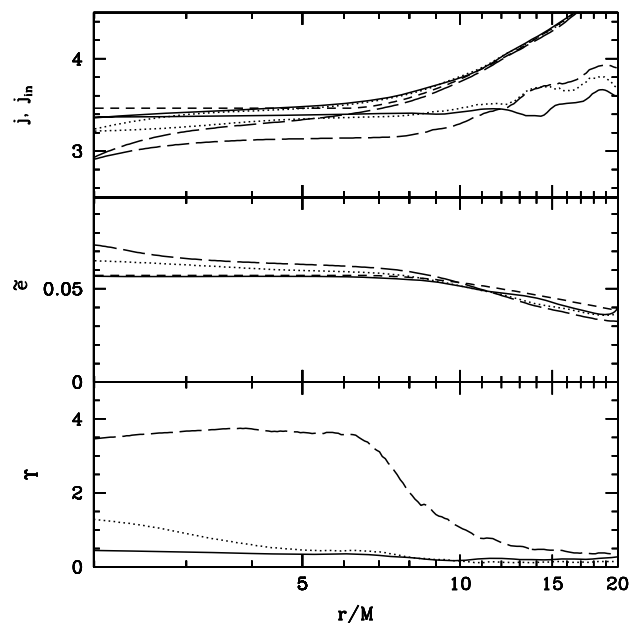

Figure 21. Radial profiles of $_{J}$ and $_{J{\rm in}}$ (top panel), $\tilde{e}$ (middle panel) and Υ (bottom panel) are shown for two different initial field geometries. Results for the fiducial four-loop field geometry (model A0HR07) integrated over $\pm 2|h/r|$ around the midplane are shown by solid lines, for the one-loop field geometry (model A0HR07LOOP1) integrated over $\pm 2|h/r|$ around the midplane by dotted lines and the one-loop model integrated over all angles by long-dashed lines. The short-dashed lines in the top two panels show the NT result. We see that the one-loop field geometry shows larger deviations from NT in $_{J}$ and Υ compared to the four-loop geometry. The panels also reemphasize the point that including all θ angles in the angular integration leads to considerable changes in $_{J}$ and Υ due to the presence of magnetic field in the corona-wind-jet.

impact on the specific angular momentum profile and the stress inside the ISCO. This also indicates that the saturated state is only reached after approximately $17000M$, and it is possible that the one-loop model may never properly converge because magnetic flux of the same sign (how much flux is initially available is arbitrary due to the arbitrary position of the initial gas pressure maximum) may continue to accrete on to the BH and lead to a qualitatively different accretion state [as seen in Igumenshchev, Narayan & Abramowicz (2003a) and McKinney & Gammie (2004) for their vertical field model]. At early times, the nominal efficiency, $\tilde{e}$, shows no significant dependence on the field geometry, and remains near the NT value for both models. At late time in the one-loop model, $\tilde{e}$ rises somewhat, which may indicate the start of the formation of a qualitatively different accretion regime.

Fig. 22 shows the normalized luminosity. We see that the one-loop model produces more luminosity inside the ISCO. For times $12900M$ to $17300M$, $\tilde{L}_{\rm in} = 5.4$ per cent (integrated over all θ) compared to 3.5 per cent for the four-loop field geometry. Thus there is 50 per cent more radiation coming from inside the ISCO in this model. At late time during the saturated state, $\tilde{L}_{\rm in} = 4.6$ per cent (integrated over all θ). Thus there is approximately 31 per cent more radiation coming from inside the ISCO in this model during the late phase of accretion.

Table 4 also reports the results for thick ($|h/r| \approx 0.3$) disc models initialized with the multi-loop and one-loop field geometries. This again shows that the deviations from NT are influenced by the initial magnetic field geometry and scale with $|h/r|$ in a way expected by our scaling laws. The one-loop models show deviations from NT in
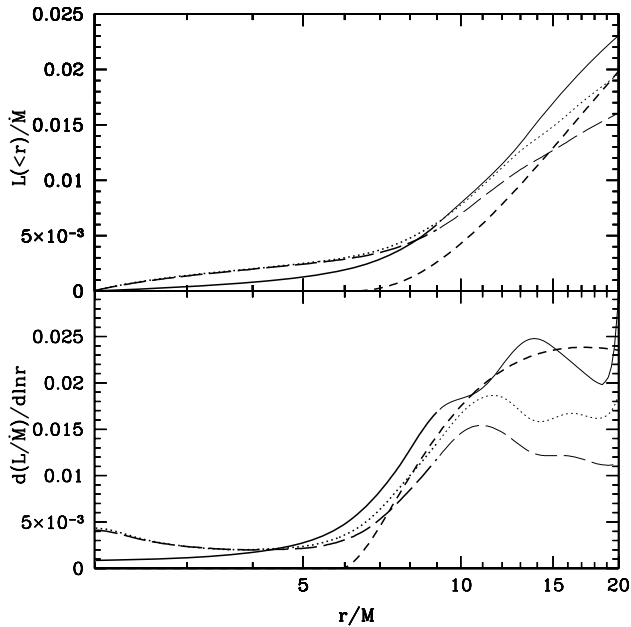
Figure 22. Similar to Fig. 21 for the initial four-loop and one-loop field geometries, but here we show the luminosity (top panel) and log-derivative of the luminosity (bottom panel). The luminosity is slightly higher for the one-loop model compared to the four-loop model.

J are larger as related to the larger value of Υ. The deviations from NT are less affected by the initial magnetic field geometry for thicker discs, because the deviations from NT are also driven by thermal effects and Reynolds stresses rather than primarily electromagnetic stresses as for thin discs.

These effects can be partially understood by looking at the specific electromagnetic stress, Υ, shown in Fig. 21. We find $\Upsilon \approx 0.45$ for the four-loop field geometry. For times $12900M$ to $17300M$, $\Upsilon \approx 0.71$ in the one-loop field geometry, and during the saturated state $\Upsilon \approx 1.28$. For times $12900M$ to $17300M$, the 50 per cent larger Υ appears to be the reason for the 50 per cent extra luminosity inside the ISCO in the one-loop model. The magnetized thin disc model of Gammie (1999) predicts that, for $a/M = 0$, specific magnetic fluxes of $\Upsilon = 0.45$, 0.71 should give deviations from NT of $-D[J] = 1.9$, 3.9, respectively. These are close to the deviations seen in the simulations, but they are not a perfect match for reasons we can explain. First, the details of how one spatially averages quantities (e.g. average of ratio versus ratio of averages) when computing Υ lead to moderate changes in its value, and, for integrations outside the midplane, comparisons to the Gammie model can require slightly

higher Υ than our diagnostic reports. Secondly, the finite thermal pressure at the ISCO leads to (on average over time) a deviation already at the ISCO that is non-negligible compared to the deviation introduced by electromagnetic stresses between the ISCO and horizon. This thermal component is not always important, e.g. see the comparison in Fig. 11. Still, as found in McKinney & Gammie (2004) for thick discs at least, the deviations from NT contributed by the thermal pressure are of the same order as the deviations predicted by the Gammie model. These results motivate extending the Gammie (1999) model to include a finite (but still small) thermal pressure such that the boundary conditions at the ISCO lead to a non-zero radial velocity.

Within the ISCO, we find that the time-averaged and volume-averaged comoving field strength for the four-loop geometry roughly follows $|b| \propto r^{-0.7}$ within $\pm 2|h/r|$ of the disc midplane, while at higher latitudes we have a slightly steeper scaling. For times $12900M$ to $17300M$, the one-loop geometry has $|b| \propto r^{-1.1}$ within $\pm 2|h/r|$ of the disc midplane, and again a slightly steeper scaling in the corona. Other than this scaling, there are no qualitative differences in the distribution of any comoving field component with height above the disc. While the Gammie (1999) solution does not predict a power-law dependence for $|b|$, for a range between $\Upsilon = 0.4$ and 0.8, the variation near the horizon is approximately $|b| \propto r^{-0.7} - r^{-0.9}$, which is roughly consistent with the simulation results. The slightly steeper slope we obtain for the one-loop geometry is consistent with a higher specific magnetic flux, although the variations in Υ for integration over different ranges of angle imply stratification and a non-radial flow which the Gammie (1999) model does not account for. This fact and the rise in Υ with decreasing radius seen in Fig. 21 indicate a non-trivial degree of angular compression as the flow moves towards the horizon. Overall, our results suggest that deviations from NT depend on the assumed field geometry, and that the Gammie (1999) model roughly fits the simulations.

Fig. 23 shows the same type of plot as in Fig. 7, but here we compare the fiducial four-loop model with the one-loop model. As mentioned above, the one-loop geometry has a larger deviation in J from the NT value, corresponding to larger stresses inside the ISCO. The absolute magnetic flux (per unit initial total absolute magnetic flux) on the BH $\tilde{\Phi}_r$ is of the order of $1/2$, suggesting that the inner half of the initial field bundle accreted on to the BH, while the other half was advected to larger radii. This is consistent with what is seen in simulations of thick tori (McKinney & Gammie 2004; Beckwith et al. 2008a). This suggests that using the one-loop geometry leads to results that are sensitive to the initial absolute magnetic flux, while the multiple-loop geometry leads to results that are insensitive to the initial absolute magnetic flux. Such dependence of the

Table 4. Field geometry study.

| Model name	$|h/r|$	$\dot{M}$	$\tilde{e}$	$D[\tilde{e}]$	J	$D[J]$	J_{in}	$D[J_{in}]$	s	$\tilde{L}_{in}$	$\tilde{L}_{eq}$	$100\tilde{\Phi}_r$	Υ
$\pm 2|h/r|$													
A0HR07	0.064	0.066	0.058	−0.829	3.363	−2.913	3.355	−3.153	3.363	0.035	0.080	1.355	0.450
A0HR07LOOP1	0.048	0.036	0.066	−14.846	3.215	−7.193	3.234	−6.637	3.215	0.049	0.059	6.198	1.281
A0HR3	0.350	44.066	−0.003	104.582	2.309	−33.331	2.408	−30.473	2.309	0.000	−0.049	3.039	1.182
A0HR3LOOP1	0.377	32.577	0.001	98.892	1.823	−47.389	1.984	−42.717	1.823	0.000	−0.049	7.599	2.246
All θ													
A0HR07	0.064	0.074	0.054	4.723	3.266	−5.717	3.281	−5.275	3.266	0.035	0.053	6.677	0.863
A0HR07LOOP1	0.048	0.040	0.075	−31.857	2.915	−15.847	2.928	−15.478	2.915	0.046	0.048	43.935	3.464
A0HR3	0.350	49.207	−0.004	106.180	2.128	−38.572	2.220	−35.919	2.128	0.000	−0.049	4.724	1.331
A0HR3LOOP1	0.377	39.382	−0.001	102.499	1.575	−54.526	1.734	−49.932	1.575	0.000	−0.049	11.444	2.523
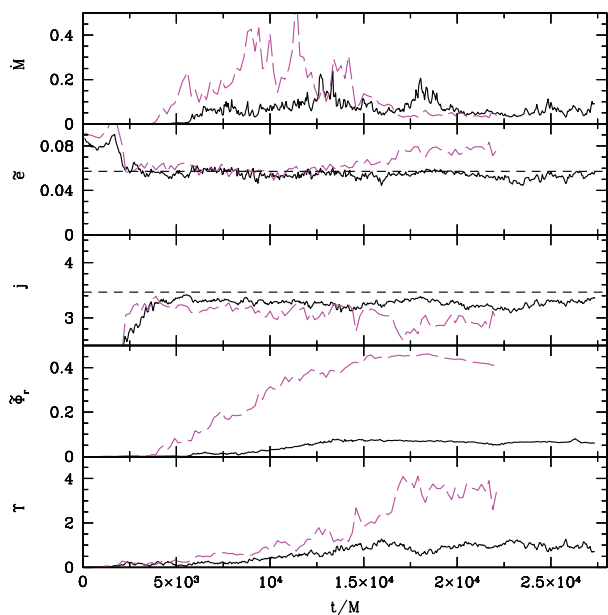
Figure 23. Similar to Fig. 7, but here we compare the initial four-loop fiducial model (black solid lines) and the one-loop model (dashed magenta lines). The horizontal black dashed lines in the second and third panels show the predictions of the NT model. The mass accretion rate, $\dot{M}$, has larger root-mean-squared fluctuations in the one-loop model, which is indicative of more vigorous turbulence. The nominal efficiency, $\tilde{e}$, shows no clear difference. The specific angular momentum, $\jmath$, is lower in the one-loop model compared to the four-loop model. This indicates that the one-loop field leads to larger stress within the ISCO. The absolute magnetic flux (per unit initial total absolute flux) on the BH is larger in the one-loop model than in the four-loop model. Since $\tilde{\Phi}_r \sim 1/2$ for the one-loop model, essentially half of the initial loop was advected on to the BH, while the other half gained angular momentum and has been advected away. This may indicate that the one-loop geometry is a poor choice for the initial field geometry, since the magnetic flux that ends up on the BH is determined by the initial conditions. The value of Υ is about twice higher in the one-loop model, which implies about twice greater electromagnetic stresses within the ISCO.

electromagnetic stress on initial magnetic field geometry has also been reported in 3D pseudo-Newtonian simulations by Reynolds & Armitage (2001) and in 3D GRMHD simulations by Beckwith et al. (2008a).

Fig. 24 shows the electromagnetic stress as computed by equation (27) for the multiple-loop fiducial model (A0HR07) and the otherwise identical one-loop model (A0HR07LOOP1). We only show the electromagnetic part of the stress, and within the ISCO this is to within a few per cent the same as the total stress obtained by including all terms in the stress-energy tensor. Outside the ISCO, the total stress agrees more with the NT model. The figure shows the full-angle integrated electromagnetic stress, the electromagnetic stress integrated over only $\pm 2|h/r|$, the NT stress and the Gammie (1999) electromagnetic stress for $\Upsilon = 0.60, 0.89, 0.90, 1.21$ (we choose Υ, the only free parameter of the model, such that the peak magnitude of the stress agrees with the simulation). The chosen Υ values are close to our diagnostic's value of Υ for these models, which demonstrates that the Gammie (1999) model is consistently predicting the simulation's results with a single free parameter. The stress is normalized by the radially dependent $\dot{M}(r)$ that is computed over the same θ integration range. We do not restrict the integration to bound material as done in S08 (in S08, the stress is integrated over $\pm 2|h/r|$ and only for bound material, while in N10 the
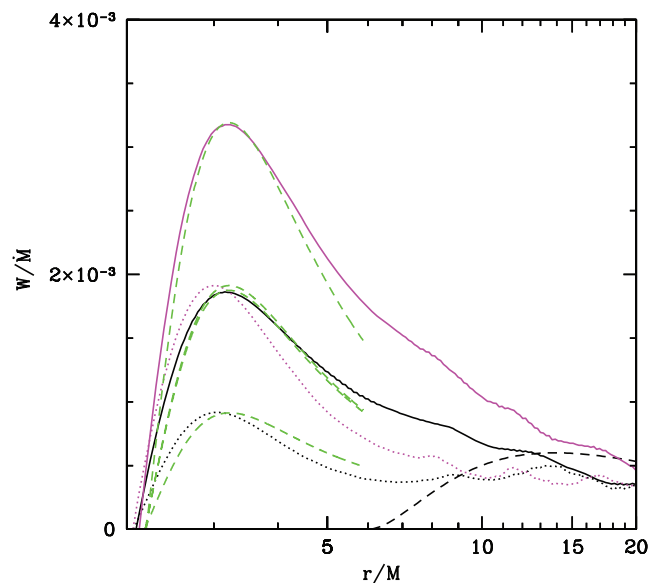
Figure 24. Normalized electromagnetic stress, $W/\dot{M}$, as a function of radius for the fiducial model (black lines) and the otherwise identical one-loop model (magenta lines). The solid lines correspond to a θ integration over all angles, while the dotted lines correspond to a θ integration over $\pm 2|h/r|$. The dashed black line shows the NT result, while the dashed green lines show the Gammie (1999) result for $\Upsilon = 0.60, 0.89, 0.90, 1.21$ for lines from the bottom to the top. The one-loop model shows about 50 per cent larger peak normalized stress (integrated over all angles) compared to the multi-loop model (integrated over all angles), which is consistent with the one-loop model leading to larger deviations from NT (about 50 per cent larger luminosity over the period used for time averaging). The large differences between the solid and dotted lines again highlight the fact that the stress within the disc is much smaller than the stress over all θ that includes the corona+wind+jet. As pointed out in S08, even though such a plot of the electromagnetic stress appears to indicate large deviations from NT within the ISCO, this is misleading because one has not specified the quantitative effect of the non-zero value of $W/\dot{M}$ on physical quantities within the ISCO. Apparently, large values of $W/\dot{M}$ do not necessarily correspond to large deviations from NT. For example, quantities such as $\jmath$, e and the luminosity only deviate by a few per cent from NT for the multi-loop model. The Gammie (1999) model gives a reasonable fit to the simulation's stress profile within the ISCO.

stress[12] is only over bound material). The stress for the fiducial model was time-averaged over the saturated state, while the one-loop model was time-averaged from time $12900M$ to $17300M$ in order to best compare with the early phase of accretion for the one-loop model studied in N10.

Fig. 24 shows that the simulation and NT stress do not agree well, and it suggests there is an *apparently* large stress within the ISCO. However, as first pointed out by S08 and discussed in Section 3.4, this stress does not actually correspond to a large deviation from NT in physically relevant quantities such as the specific angular momentum, specific energy and luminosity. This point is clarified by making a comparison to the Gammie (1999) model's stress, which agrees reasonably well with the simulation stress inside the ISCO. Even though the stress may appear large inside the ISCO, the stress corresponding to the Gammie model with (e.g.) $\Upsilon =$

---

[12] N10's figs 12 and 13 show stress versus radius, but some of the integrals they computed were not re-normalized to the full 2π when using their simulation ϕ-box size of $\pi/2$, so their stress curves are all a constant factor of four times larger than the actual stress (Noble, private communication).

0.60 only translates into a few per cent deviations from NT. This figure also demonstrates that the initial magnetic field geometry affects the amplitude of the stress in the same direction as it affects other quantities and is reasonably well predicted by the Gammie (1999) model. The initial magnetic field sets the saturated value of Υ, which is directly related to the electromagnetic stresses within the ISCO. The one-loop model leads to a peak stress (integrated over all angles) within the ISCO that is about 50 per cent larger than the multi-loop model (integrated over all angles), which is likely related to the extra 50 per cent luminosity in the one-loop model compared to the multi-loop model. The fact that the stress normalization changes with initial field geometry is consistent with other 3D GRMHD simulations of thick discs by Beckwith et al. (2008a). This figure again shows how the stress within the disc ($\pm 2|h/r|$) is much smaller than the total disc+corona+wind+jet (all θ).

Finally, we discuss previous results obtained for other field geometries using an energy-conserving 2D GRMHD code (McKinney & Gammie 2004). While such 2D simulations are unable to sustain turbulence, the period over which the simulations do show turbulence agrees quite well with the corresponding period in 3D simulations. This implies that the turbulent period in the 2D simulations may be qualitatively correct. The fiducial model of McKinney & Gammie (2004) was of a thick ($|h/r| \sim 0.2$–0.25) disc with a one-loop initial field geometry around an $a/M = 0.9375$ BH. This model had $\Upsilon \sim 1$ near the midplane within the ISCO and $\Upsilon \sim 2$ when integrated over all θ angles. Their measured value of $j \approx 1.46$ integrated over all angles, $|b| \propto r^{-1.3}$ within the ISCO within the disc midplane (McKinney & Narayan 2007b), along with $\Upsilon \sim 1$–2 are roughly consistent with the Gammie (1999) model prediction of $j \approx 1.5$. Similarly, the strong vertical field geometry model they studied had $\Upsilon \sim 2$ near the midplane within the ISCO and $\Upsilon \sim 6$ integrated over all θ angles. Their measurement of $j \approx -1$ integrated over all angles is again roughly consistent with the model prediction of $j \approx -1.2$ for $\Upsilon \sim 6$. Note that in this model, Υ rises (as usual to reach saturation) with time, but soon after $\Upsilon \gtrsim 2$ in the midplane, the disc is pushed away by the BH and then Υ is forced to be even larger. Evidently, the accumulated magnetic flux near the BH pushes the system into a force-free magnetosphere state – not an accretion state. This shows the potential danger of using strong-field initial conditions (like the one-loop field geometry), since the results are sensitive to the assumed initial flux that is placed on (or rapidly drops on to) the BH. Even while the disc is present, this particular model exhibits net angular momentum extraction from the BH. This interesting result needs to be confirmed using 3D simulations of both thick and thin discs.

9 COMPARISONS WITH OTHER RESULTS

The results we have obtained in the present work are consistent with those of Armitage, Reynolds & Chiang (2001) and Reynolds & Fabian (2008), who carried out pseudo-Newtonian studies, and with the results of S08, who did a full GRMHD simulation. These studies found only minor deviations from NT for thin accretion discs with a multi-loop initial field geometry. However, more recently, N09 and N10 report *apparently* inconsistent results, including factors of up to 5 larger deviations from NT in the specific angular momentum (2 per cent in S08 versus 10 per cent in N10) for the same disc thickness of $|h/r| \sim 0.07$. They also found a 50 per cent larger deviation from NT in the luminosity (4 per cent in S08 versus 6 per cent in N09). Furthermore, in N10 they concluded that the electromagnetic stresses have no dependence on disc thick-

ness or initial magnetic field geometry, whereas we find that the electromagnetic stresses have a statistically significant dependence on both disc thickness and magnetic field geometry.

We have considered several possible explanations for these differences, as we now describe. We attempt to be exhaustive in our comparison with the setup and results by N09 and N10, because our works and their works seek accuracies much better than order two in measuring deviations from NT. Thus, any deviations between our results by factors of 2 or more must be investigated further in order to ensure a properly understood and accurate result.

First, we briefly mention some explanations that N10 propose as possible reasons for the discrepant results, viz., differences in (1) numerical algorithm or resolution; (2) box size in ϕ-direction: $\Delta\phi$; (3) amplitude of initial perturbations; (4) accuracy of inflow equilibrium and (5) duration of the simulations. Our algorithms are similar except that their PPM interpolation scheme assumes primitive quantities are cell averages (standard PPM), while ours assumes they are point values (as required to be applied in a higher-order scheme). They used LAXF dissipative fluxes, while we used HLL fluxes that are about twice more accurate for shocks and may be more accurate in general. On the other hand, they used parabolic interpolation for the Toth electric field, while we use the standard Toth scheme. Given these facts, we expect that the accuracy of our algorithms is similar. Overall, our convergence testing and other diagnostics (see Section 6) confirm that none of their proposed issues can be the cause of differences between S08 and N10.

We have shown that inflow equilibrium must include saturation of the specific magnetic flux, Υ, which generally saturates later in time than other quantities. By running our fiducial model A0HR07 to a time of nearly $30000M$, we ensure that we have a long period of steady-state conditions to compute our diagnostic quantities. The fact that we need to run our fiducial thin disc simulation for such a long time to reach inflow equilibrium up to a radius $r \sim 9M$ is completely consistent with our analytical estimate of the time-scale calculated using equation (B7) of Appendix B (see the earlier discussion in Section 3.5 and Fig. 6). In the comparison between the numerical and analytical results shown in Fig. 6, we found agreement by setting $\alpha|h/r|^2 \approx 0.00033$ which, for our disc with $|h/r| \approx 0.064$, corresponds to $\alpha \approx 0.08$. With this value of $\alpha|h/r|^2$, we would have to run the simulation until $t \sim 83000M$, $160000M$, to reach inflow equilibrium out to $15M$, $20M$, respectively, corresponding to a couple viscous time-scales at each radius. N10 stated that they reach inflow equilibrium within $r \sim 15M$–$20M$ in a time of only $t \sim 10000M$. Since their disc thickness is $|h/r| \approx 0.06$, even a single viscous time-scale would require their simulations to have $\alpha \sim 0.38$ to reach an inflow equilibrium up to $r \sim 15M$, and an even larger value of α for $r \sim 20M$. This seems unlikely. We can partially account for their result by considering our one-loop model, which up to $t \sim 17000M$ has $\alpha|h/r|^2$ twice as large and α about 70 per cent larger than in the fiducial four-loop run. However, this still falls far short by a factor of roughly 3 of what N10 would require for inflow equilibrium up to $15M$–$20M$. Further, our A0HR07LOOP1 model, which is similar to their model, only reaches a saturated state by $17000M$, and only the Υ quantity indicates that saturation has been reached. If we were to measure quantities from $10000M$ to $15000M$ as in N10, we would have underestimated the importance of magnetic field geometry on the electromagnetic stresses.

Since all these simulations are attempting to obtain accuracies better than the factors of 2 in the results, this inflow equilibrium issue should be explored further. A few possible resolutions include: (1) N10's higher resolution leads to a much larger α; (2) their disc

has a larger 'effective' thickness, e.g. $|h/r| \sim 0.13$, according to equation (5.9.8) in NT (see equation B7 of Appendix B); (3) some aspects of their solution have not yet reached inflow equilibrium within a radius much less than $r \sim 15M$, such as the value of Υ versus time that saturates much later than other quantities; or (4) they achieve constant fluxes versus radius due to transient non-viscous effects – although one should be concerned that the actual value of such fluxes continues to secularly evolve in time and one still requires evolution on the longer viscous (turbulent diffusion) time-scale to reach true inflow equilibrium.

Secondly, we considered various physical setup issues, including differences in: (1) range of BH spins considered; (2) range of disc thicknesses studied; (3) ad hoc cooling function and (4) equation of state. We span the range of BH spins and disc thicknesses studied by N10, so this is unlikely to explain any of the differences. Some differences could be due to the disc thickness versus radius profiles established by the ad hoc cooling functions in the two studies. N10's cooling function is temperature-based and allows cooling even in the absence of any dissipation, while ours is based upon the specific entropy and cools the gas only when there is dissipation. Both models avoid cooling unbound gas. In S08 and in the present paper, we use an ideal gas equation of state with $\Gamma = 4/3$, while N09 and N10 used $\Gamma = 5/3$. The properties of the turbulence do appear to depend on the equation of state (Mignone & McKinney 2007), so it is important to investigate further the role of Γ in thin discs.

Thirdly, the assumed initial field geometry may introduce critical differences in the results. Issues with the initial field geometry include how many field reversals are present, how isotropic the field loops are in the initial disc, how the electromagnetic field energy is distributed in the initial disc and how the magnetic field is normalized. In S08 and here, we have used a multi-loop geometry in the initial torus consisting of alternating polarity poloidal field bundles stacked radially. We ensure that the field loops are roughly isotropic within the initial torus. We set the ratio of maximum gas pressure to maximum magnetic pressure to $\beta_{\mathrm{maxes}} = 100$, which gives us a volume-averaged mean β within the dense part of the torus ($\rho_0/\rho_{0,\mathrm{max}} \geq 0.2$) of $\bar{\beta} \sim 800$. Our procedure ensures that all initial local values of β within the disc are much larger than the values in the evolved disc, i.e. there is plenty of room for the magnetic field to be amplified by the MRI.

We have also studied a one-loop geometry that is similar to the one-loop geometry used in N09 and N10. Their initial ϕ-component of the vector potential is $A_\phi \propto \mathrm{MAX}(\rho_0/\rho_{0,\mathrm{max}} - 0.25, 0)$ (Noble, private communication). They initialize the magnetic field geometry by ensuring that the volume-averaged gas pressure divided by the volume-averaged magnetic pressure is $\beta_{\mathrm{averages}} = 100$ (Noble, private communication). (They stated that the mean initial plasma β is $\bar{\beta} = 100$.) For their thin disc torus model parameters, this normalization procedure leads to a portion of the inner radial region of the torus to have a local value of $\beta \sim 3\text{–}8$, which may be a source of differences in our results since such a small β is lower than present in the saturated disc. N10 make use of an older set of simulations from a different non-energy-conserving code (Hawley & Krolik 2006; Beckwith et al. 2008a) to investigate the effect of other field geometries. The results from this other code have strong outliers, e.g. the KD0c model, and so we are unsure if these other simulations can be used for such a study.

N10 state that they find no clear differences in the electromagnetic stresses for different initial field geometries. As shown in their figs 12 and 13, the Agol & Krolik (2000) model captures the smoothing of the stress outside the ISCO, but it is not a model for the behaviour of the stress inside the ISCO. We find that electromagnetic stresses have a clear dependence on both disc thickness and the initial magnetic field geometry, with a trend that agrees with the Gammie (1999) model of a magnetized thin disc. Our Fig. 24 shows that the stress within the ISCO is reasonably well modelled by the Gammie (1999) model. Our one-loop thin disc model gives a peak normalized stress (integrated over all angles) of about 3.2×10^{-3} for times $12900M$ to $17300M$, which is comparable to the one-loop thin disc model in N10 with peak normalized stress (integrated over all angles) of about 2.5×10^{-3} (after correcting for their ϕ-box size). Hence, we are able to account for the results of their one-loop model.

In addition, we used the specific magnetic flux, Υ, an ideal MHD invariant that is conserved within the ISCO, to identify how electromagnetic stresses scale with disc thickness and magnetic field geometry. In the saturated state, the value of Υ, which controls the electromagnetic stresses, is different for different initial magnetic field geometries. The larger the value of Υ, the larger the deviations from NT in $\jmath$. We find that $\jmath$ within the disc ($\pm 2|h/r|$ from the midplane) deviates from NT by -3 per cent in our four-loop model and -6 per cent in our one-loop model for times $12900M$ to $17300M$. Integrating over all angles, $\jmath$ deviates by -6 per cent for the four-loop model and -11 per cent for the one-loop model for times $12900M$ to $17300M$. Thus, we find a clear factor of 2 change, depending on the assumed initial field geometry and the range of integration. The excess luminosity is 3.5 per cent for the four-loop model and 5.4 per cent for the one-loop model for times $12900M$ to $17300M$. Recalling that N10 find a deviation from NT of about -10 per cent in $\jmath$ (integrated over all angles) and a luminosity excess beyond NT of about 6%, this shows we can completely account for the *apparent* inconsistencies mentioned by N10 by invoking dependence of the results on the initial field geometry and the presence of extra stress beyond the disk component of the accretion flow.

Fourth, let us consider measurement and interpretation differences. Our ultimate goal is to test how well the NT model describes a magnetized thin accretion disc. The primary quantity that is used to measure this effect in S08 and N10 is the specific angular momentum $\jmath$. However, the measurements are done differently in the two studies. In S08 as well as in this paper, we focus on the disc gas by limiting the range of θ over which we compute the averaging integrals ($\pm 2|h/r|$ from the midplane). In contrast, N10 compute their integrals over a much wider range of θ which includes both the disc and the corona-wind-jet (Noble, 2010, private communications). We have shown in Section 5.7 that the disc and corona-wind-jet contribute roughly equally to deviations of $\jmath$ from the NT value. In principle, the luminosity from the corona-wind-jet could be important, but we have shown that the excess luminosity of bound gas within the ISCO is dominated by the disc. This means that the measure used by N10, consisting of integrating over all gas to obtain $\jmath$, cannot be used to infer the excess luminosity of bound gas within the ISCO. Further, the corona would largely emit non-thermal radiation, so for applications in which one is primarily interested in the thermal component of the emitted radiation, one should evaluate the accuracy of the NT model by restricting the angular integration range to the disc component within $\pm 2|h/r|$.

Fifth, let us consider how the results from N10 scale with disc thickness for the specific case of a non-spinning ($a/M = 0$) BH. We have performed a linear least-squares fit of their simulation results, omitting model KD0c which is a strong outlier. For $\jmath$ integrated over all θ, their relative difference follows $D[\jmath] \approx -7 - 45|h/r|$ with confidence of 95 per cent that these coefficients, respectively, only deviate by ± 67 per cent and ± 89 per cent. These fits imply that, as

$|h/r| \to 0$, the relative deviation of $\jmath$ from the NT value is about -7 per cent, but they could easily be as low as -2 per cent. Their results do not indicate a statistically significant large deviation from NT as $|h/r| \to 0$. Since the total deviation in $\jmath$ from NT includes the effects of electromagnetic (and all other) stresses, this implies that their models are consistent with weak electromagnetic stresses as $|h/r| \to 0$.

Further, we have already established that the one-loop geometry gives (at least) twice the deviation from NT compared to the four-loop geometry, plus there is another factor of 2 arising from including the corona-wind-jet versus not including it. This net factor of 4 applied to N10's results implies that $\jmath$ would deviate by about -2 per cent or even as low as -0.5 per cent from NT in the limit $|h/r| \to 0$ if they were to consider a four-loop field geometry and focus only on the disc gas. Thus, their models show no statistically significant large deviations from NT. In addition, our results in Section 7.1 show that, whether we consider an integral over all angles or only over the disc, there is no statistically significant large deviation from NT as $|h/r| \to 0$.

In summary, we conclude that the apparent differences between the results obtained in S08 and the present paper on the one hand, and those reported in N09 and N10 on the other, are due to (1) dependence on initial magnetic field geometry (multi-loop versus one-loop); (2) dependence upon the initial magnetic field distribution and normalization and (3) measurement and interpretation differences (disc versus corona-wind-jet). Note in particular that the one-loop initial field geometry is severely squashed in the vertical direction and elongated in the radial direction for thin discs, and it is not clear that such a geometry would ever arise naturally. There are also indications from our simulation that the one-loop geometry may actually never reach a converged state due to the arbitrary amount of magnetic flux accreted on to the BH due to the single polarity of the initial magnetic field. Finally, if one is trying to test how well-simulated thin accretion discs compare with NT, then it is important to restrict the comparison to disc gas near the midplane. One should not expect the gas in the corona-wind-jet to agree with the NT model.

10 DISCUSSION

We now discuss some important consequences of our results and also consider issues to be addressed by future calculations. First, we discuss the relevance to BH spin measurements.

In recent years, BH spin parameters have been measured in several BH X-ray binaries by fitting their X-ray continuum spectra in the thermal (or high-soft) spectral state (Zhang, Cui & Chen 1997; Shafee et al. 2006; McClintock et al. 2006; Davis, Done & Blaes 2006; Liu et al. 2008; Gou et al. 2009, 2010). This method is based on several assumptions that require testing (Narayan, McClintock & Shafee 2008), the most critical being the assumption that an accretion disc in the radiatively efficient thermal state is well-described by the Novikov–Thorne model of a thin disc. More specifically, in analysing and fitting the spectral data, it is assumed that the radial profile of the radiative flux, or equivalently the effective temperature, in the accretion disc closely follows the prediction of the NT model.

Practitioners of the continuum-fitting method generally restrict their attention to relatively low-luminosity systems below 30 per cent of the Eddington luminosity. At these luminosities, the maximum height of the disc photosphere above the midplane is less than 10 per cent of the radius, i.e. $(h/r)_{\text{photosphere}} \leq 0.1$

(McClintock et al. 2006). For a typical disc, the photospheric disc thickness is approximately twice the mean absolute thickness $|h/r|$ that we consider in this paper. Therefore, the discs that observers consider for spin measurement have $|h/r| \lesssim 0.05$, i.e. they are thinner than the thinnest disc ($|h/r|_{\text{min}} \sim 0.06$) that we (S08, this paper) and others (N09, N10) have simulated.

The critical question then is the following. Do the flux profiles of very thin discs match the NT prediction? At large radii the two will obviously match very well since the flux profile is determined simply by energy conservation.[13] However, in the region near and inside the ISCO, analytic models have to apply a boundary condition, and the calculated flux profile in the inner region of the disc depends on this choice. The conventional choice is a 'zero-torque' boundary condition at the ISCO. Unfortunately, there is disagreement on the validity of this assumption. Some authors have argued that the magnetic field strongly modifies the zero-torque condition and that, therefore, real discs might behave very differently from the NT model near the ISCO (Krolik 1999; Gammie 1999). Other authors, based either on heuristic arguments or on hydrodynamic calculations, find that the NT model is accurate even near the ISCO so long as the disc is geometrically thin (Paczyński 2000; Afshordi & Paczyński 2003; Abramowicz et al. 2010; S08). Investigating this question was the primary motivation behind the present study.

We described in this paper GRMHD simulations of geometrically thin ($|h/r| \sim 0.07$) accretion discs around BHs with a range of spins: $a/M = 0, 0.7, 0.9, 0.98$. In all cases, we find that the specific angular momentum $\jmath$ of the accreted gas as measured at the horizon (this quantity provides information on the dynamical importance of torques at the ISCO) shows only minor deviations at the level of $\sim$2–4 per cent from the NT model. Similarly, the luminosity emitted inside the ISCO is only $\sim$3–7 per cent of the total disc luminosity. When we allow for the fact that a large fraction of this radiation will probably be lost into the BH because of relativistic beaming as the gas plunges inward (an effect ignored in our luminosity estimates), we conclude that the region inside the ISCO is likely to be quite unimportant. Furthermore, our investigations indicate that deviations from the NT model decrease with decreasing $|h/r|$. Therefore, since the discs of interest to observers are generally thinner than the thinnest discs we have simulated, the NT model appears to be an excellent approximation for modelling the spectra of BH discs in the thermal state.

One caveat needs to be mentioned. Whether or not the total luminosity of the disc agrees with the NT model is not important since, in spectral modelling of data, one invariably fits a normalization (e.g. the accretion rate $\dot{M}$ in the model KERRBB; Li et al. 2005) which absorbs any deviations in this quantity. What is important is the *shape* of the flux profile versus radius. In particular, one is interested in the radius at which the flux or effective temperature is maximum (Narayan et al. 2008; McClintock et al. 2009). Qualitatively, one imagines that the fractional shift in this radius will be of the order of the fractional torque at the ISCO, which is likely to be of the order of the fractional error in $\jmath$. We thus guess that, in the systems of interest, the shift is nearly always below 10 per cent. We plan to explore this question quantitatively in a future study.

Another issue is the role of the initial magnetic field topology. We find that, for $a/M = 0$, starting with a one-loop field geometry gives an absolute relative deviation in $\jmath$ of 7.1 per cent, and

---

[13] This is why the formula for the flux as a function of radius in the standard thin disc model does not depend on details like the viscosity parameter α (Frank et al. 1992).

an excess luminosity inside the ISCO of 4.9 per cent, compared to 2.9 per cent and 3.5 per cent for our standard four-loop geometry. Thus, having a magnetic field distribution with long-range correlation in the radial direction seems to increase deviations from the NT model, though even the larger effects we find in this case are probably not a serious concern for BH spin measurement. Two comments are in order on this issue. First, the four-loop geometry is more consistent with nearly isotropic turbulence in the poloidal plane and, therefore, in our view a more natural initial condition. Secondly, the one-loop model develops a stronger field inside the ISCO and around the BH and might therefore be expected to produce a relativistic jet with measurable radio emission. However, it is well-known that BH X-ray binaries in the thermal state have no detectable radio emission. This suggests that the magnetic field is probably weak, i.e. more consistent with our four-loop geometry.

Next, we discuss the role of electromagnetic stresses on the dynamics of the gas in the plunging region inside the ISCO. In order to better understand this issue, we have extracted for each of our simulations the radial profile of the specific magnetic flux, Υ. This quantity appears as a dimensionless free parameter (called $F_{\theta\phi}$) in the simple MHD model of the plunging region developed by Gammie (1999). The virtues of the specific magnetic flux are its well-defined normalization and its constancy with radius for stationary flows (Takahashi et al. 1990). In contrast, quantities like the stress W or the viscosity parameter α have no well-defined normalization; W can be normalized by any quantity that has an energy scale, such as ρ_0, $\dot{M}$ or b^2, while α could be defined with respect to the total pressure, the gas pressure or the magnetic pressure. The numerical values of W or α inside the ISCO can thus vary widely, depending on which definition one chooses. For instance, although S08 found $\alpha \sim 1$ inside the ISCO, the specific angular momentum flux, $_J$, deviated from NT by no more than a few per cent. Further, Fig. 24 shows that (even for the multi-loop model) the stress appears quite large within the ISCO, but this is misleading because the effects of the stress are manifested in the specific angular momentum, specific energy and luminosity – all of which agree with NT to within less than 10 per cent for the multi-loop model. Since W and α do not have a single value within the ISCO or a unique normalization, we conclude that they are not useful for readily quantifying the effects of the electromagnetic stresses within the ISCO.

Gammie's (1999) model shows how the value of Υ is directly related to the electromagnetic stresses within the ISCO. Unfortunately, the actual value of Υ is a free parameter which cannot be easily determined from first principles. It is possible that accretion discs might have $\Upsilon \gg 1$, in which case, the model predicts large deviations from NT. For example, if $\Upsilon = 6$, then for an $a/M = 0$ BH $_J$ is lowered by 56 per cent relative to the NT model. We have used our 3D GRMHD simulations which include self-consistent MRI-driven turbulence to determine the value of Υ for various BH spins, disc thicknesses and field geometries. For the multiple-loop field geometry, we find that the specific magnetic flux varies with disc thickness and spin as

$$\Upsilon \approx 0.7 + \left|\frac{h}{r}\right| - 0.6\frac{a}{M}, \tag{41}$$

within the disc component, which indicates that electromagnetic stresses are weak and cause less than 8 per cent deviations in $_J$ in the limit $|h/r| \to 0$ for all BH spins. Our rough analytical arguments for how Υ should scale with $|h/r|$ and a/M are consistent with the above formula. Even for the one-loop field geometry, $\Upsilon \lesssim 1$ for thin discs, so electromagnetic stresses cause only minor deviations from NT for all BH spins (for $\Upsilon \lesssim 1$, less than 12 per cent in $_J$). Not all

aspects of the Gammie (1999) model agree with our simulations. As found in McKinney & Gammie (2004), the nominal efficiency, $\tilde{e}$, does not match well and for thin discs is quite close to NT. Since the true radiative efficiency is limited to no more than $\tilde{e}$, this predicts only weak deviations from NT in the total luminosity even if $_J$ has non-negligible deviations from NT. Also, this highlights that the deviations from NT in $_J$ are due to non-dissipated electromagnetic stresses and cannot be used to directly predict the excess luminosity within the ISCO. The assumption of a radial flow in a split-monopole field is approximately valid, but the simulations do show some non-radial flow and vertical stratification, a non-zero radial velocity at the ISCO and thermal energy densities comparable to magnetic energy densities. Inclusion of these effects is required for better consistency with simulation results inside the ISCO.

Next, we consider how our results lend some insight into the spin evolution of BHs. Standard thin disc theory with photon capture predicts that an accreting BH spins up until it reaches spin equilibrium at $a_{eq}/M \approx 0.998$ (Thorne 1974). On the other hand, thick non-radiative accretion flows deviate significantly from NT and reach equilibrium at $a_{eq}/M \sim 0.8$ for a model with $\alpha \sim 0.3$ and $|h/r| \sim 0.4$ near the horizon (Popham & Gammie 1998). GRMHD simulations of moderately thick ($|h/r| \sim 0.2$–0.25) magnetized accretion flows give $a_{eq}/M \approx 0.9$ (Gammie et al. 2004). In this paper, we find from our multi-loop field geometry models that spin equilibrium scales as

$$\frac{a_{eq}}{M} \approx 1.1 - 0.8\left|\frac{h}{r}\right|, \tag{42}$$

where one should set $a_{eq}/M = 1$ if the above formula gives $a_{eq}/M > 1$. This gives a result consistent with the above-mentioned studies of thick discs, and it is also consistent with our rough analytical prediction based upon our scaling of Υ and using the Gammie model prediction for the spin equilibrium. This result also agrees with the NT result in the limit $|h/r| \to 0$ within our statistical errors, and shows that magnetized thin discs can approach the theoretical limit of $a_{eq}/M \approx 1$, at least in the multi-loop case. In the single-loop field geometry, because of the presence of a more radially elongated initial poloidal field, we find a slightly stronger torque on the BH. However, before a time of order $17000M$, the deviations in the equilibrium spin parameter, a_{eq}/M, between the four-loop and one-loop field geometries appear to be minor, so during that time the scaling given above roughly holds. Of course, it is possible (even likely) that radically different field geometries or anomalously large initial field strengths will lead to a different scaling.

Lastly, we mention a number of issues which we have neglected but are potentially important. A tilt between the angular momentum vector of the disc and the BH rotation axis might significantly affect the accretion flow (Fragile et al. 2007). We have not accounted for any radiative transfer physics, nor have we attempted to trace photon trajectories (see e.g. N09 and Noble & Krolik 2009). In principle, one may require the simulation to be evolved for hundreds of orbital times at a given radius in order to completely erase the initial conditions (Sorathia, Reynolds & Armitage 2010), whereas we only run the model for a couple of viscous time-scales. New pseudo-Newtonian simulations show that convergence may require resolving several disc scaleheights with high resolution (Sorathia et al. 2010), and a similar result has been found also for shearing box calculations with no net flux and no stratification (Stone 2010, private communication). In contrast, we resolve only a couple of scaleheights. Also, we have only studied two different types of initial

field geometries. Future studies should consider whether alternative field geometries change our results.

11 CONCLUSIONS

We set out in this study to test the standard model of thin accretion discs around rotating BHs as developed by NT. We studied a range of disc thicknesses and BH spins and found that magnetized discs are consistent with NT to within a few per cent when the disc thickness $|h/r| \lesssim 0.07$. In addition, we noted that deviations from the NT model decrease as $|h/r|$ goes down. These results suggest that BH spin measurements via the X-ray continuum-fitting method (Zhang et al. 1997; Shafee et al. 2006; McClintock et al. 2006; Davis et al. 2006; Liu et al. 2008; Gou et al. 2009, 2010), which are based on the NT model, are robust to model uncertainties so long as $|h/r| \lesssim 0.07$. At luminosities below 30 per cent of Eddington, we estimate disc thicknesses to be $|h/r| \lesssim 0.05$, so the NT model is perfectly adequate.

These results were obtained by performing global 3D GRMHD simulations of accreting BHs with a variety of disc thicknesses, BH spins and initial magnetic field geometries in order to test how these affect the accretion disc structure, angular momentum transport, luminosity and the saturated magnetic field. We explicitly tested the convergence of our numerical models by considering a range of resolutions, box sizes and amplitude of initial perturbations. As with all numerical studies, future calculations should continue to clarify what aspects of such simulations are converged by performing more parameter space studies and running the simulations at much higher resolutions. For example, it is possible that models with different BH spins require more or less resolution than the $a = 0$ models, while we fixed the resolution for all models and only tested convergence for the $a = 0$ models.

We confirmed previous results by S08 for a non-spinning ($a/M = 0$) BH, which showed that thin ($|h/r| \lesssim 0.07$) discs initialized with multiple poloidal field loops agree well with the NT solution once they reach steady state. For the fiducial model described in the present paper, which has similar parameters as the S08 model, we find 2.9 per cent relative deviation in the specific angular momentum accreted through the disc, and 3.5 per cent excess luminosity from inside the ISCO. Across all BH spins that we have considered, viz., $a/M = 0, 0.7, 0.9, 0.98$, the relative deviation from NT in the specific angular momentum is less than 4.5 per cent, and the luminosity from inside the ISCO is less than 7 per cent (typically smaller, and much of it is likely lost to the hole). In addition, all deviations from NT appear to be roughly proportional to $|h/r|$.

We found that the assumed initial field geometry modifies the accretion flow. We investigated this effect by considering two different field geometries and quantified it by measuring the specific magnetic flux, Υ, which is an ideal MHD invariant (like the specific angular momentum or specific energy). The specific magnetic flux can be written as a dimensionless free parameter that enters the magnetized thin disc model of Gammie (1999). This parameter determines how much the flow deviates from NT as a result of electromagnetic stresses. We found that Υ allows a quantitative understanding of the flow within the ISCO, while the electromagnetic stress (W) has no well-defined normalization and varies widely within the ISCO. While a plot of the stress may appear to show large stresses within the ISCO, the actual deviations from NT can be small. This demonstrates that simply plotting W is not a useful diagnostic for measuring deviations from NT. We found that the

specific magnetic flux of the gas inside the ISCO was substantially larger when we used a single poloidal magnetic loop to initialize the simulation compared to our fiducial four-loop run. For $a/M = 0$ and $|h/r| \lesssim 0.07$, the early saturated phase (times $12900M$ to $17300M$) of the evolution for the one-loop geometry gave 5.6 per cent relative deviation in the specific angular momentum and 5.8 per cent excess luminosity inside the ISCO. These deviations are approximately twice as large as the ones we found for the four-loop simulation. At late times, the one-loop model generates significant deviations from NT, which is a result similar to that found in a vertical field model in McKinney & Gammie (2004). However, we argued that the multiple-loop geometry we used is more natural than the single-loop geometry, since for a geometrically thin disc the magnetic field in the one-loop model is severely squashed vertically and highly elongated radially. The one-loop model is also likely to produce a strong radio jet.

More significant deviations from NT probably occur for discs with strong ordered magnetic field, as found in 2D GRMHD simulations by McKinney & Gammie (2004). Of course, in the limit that the magnetic field energy density near the BH exceeds the local rest-mass density, a force-free magnetosphere will develop and deviations from the NT model will become extreme. We argued that this corresponds to when the specific magnetic flux $\Upsilon \gtrsim 1$ near the disc midplane. Our one-loop model appears to be entering such a phase at late time after accumulation of a significant amount of magnetic flux. Such situations likely produce powerful jets that are not observed in BH X-ray binaries in the thermal state. However, transition between the thermal state and other states with a strong power-law component (Fender et al. 2004; Remillard & McClintock 2006) may be partially controlled by the accumulation of magnetic flux causing the disc midplane (or perhaps just the corona) to breach the $\Upsilon \sim 1$ barrier. Such a behaviour has been studied in the non-relativistic regime (Narayan, Igumenshchev & Abramowicz 2003; Igumenshchev, Narayan & Abramowicz 2003b; Igumenshchev 2009), but more work using GRMHD simulations is required to validate the behaviour.

We also found that the apparently different results obtained by N10 were mostly due to measurement and interpretation differences. We found that both the disc and the corona-wind-jet contribute nearly equally to deviations in the total specific angular momentum relative to the NT model. However, the corona-wind-jet contributes much less to the luminosity than the disc component. Therefore, if one is interested in comparing the luminous portion of the disc in the simulations against the NT model, the only fair procedure is to consider only the disc gas, i.e. gas within a couple of scaleheights of the midplane. This is the approach we took in this study (also in S08). N10 on the other hand included the corona-wind-jet gas in their calculation of the specific angular momentum. The dynamics of the coronal gas differs considerably from the NT model. Therefore, while it does not contribute to the luminosity of bound gas, it doubles the deviation of the specific angular momentum from the NT model. In addition, N10 used a one-loop initial field geometry for their work which, as discussed above, further enhanced deviations.

REFERENCES

Abramowicz M., Jaroszynski M., Sikora M., 1978, A&A, 63, 221

Abramowicz M. A., Jaroszynski M., Kato S., Lasota J.-P., Rozanska A., Sadowski A., 2010, A&A, in press (arXiv:1003.3887)

Afshordi N., Paczyński B., 2003, ApJ, 592, 354

Agol E., Krolik J. H., 2000, ApJ, 528, 161

Armitage P. J., Reynolds C. S., Chiang J., 2001, ApJ, 548, 868

Balbus S. A., Hawley J. F., 1991, ApJ, 376, 214

Balbus S. A., Hawley J. F., 1998, Rev. Mod. Phys., 70, 1

Bardeen J. M., 1970, ApJ, 161, 103

Beckwith K., Hawley J. F., Krolik J. H., 2008a, ApJ, 678, 1180

Beckwith K., Hawley J. F., Krolik J. H., 2008b, MNRAS, 390, 21

Bekenstein J. D., Oron E., 1978, Phys. Rev. D, 18, 1809

Berti E., Volonteri M., 2008, ApJ, 684, 822

Blandford R. D., 1976, MNRAS, 176, 465

Blandford R. D., Znajek R. L., 1977, MNRAS, 179, 433

Chakrabarti S. K., 1985a, ApJ, 288, 1

Chakrabarti S. K., 1985b, ApJ, 294, 383

Colella P., Woodward P. R., 1984, J. Comp. Phys., 54, 174

Davis S. W., Done C., Blaes O. M., 2006, ApJ, 647, 525

De Villiers J.-P., Hawley J. F., Krolik J. H., 2003, ApJ, 599, 1238

Fender R. P., Belloni T. M., Gallo E., 2004, MNRAS, 355, 1105

Font J. A., Ibáñez J. M., Papadopoulos P., 1998, ApJ, 507, L67

Fragile P. C., Blaes O. M., Anninos P., Salmonson J. D., 2007, ApJ, 668, 417

Frank J., King A., Raine D., 1992, Accretion power in astrophysics. Cambridge Univ. Press, Cambridge, UK

Gammie C. F., 1999, ApJ, 522, L57

Gammie C. F., McKinney J. C., Tóth G., 2003, ApJ, 589, 444

Gammie C. F., Shapiro S. L., McKinney J. C., 2004, ApJ, 602, 312

Gou L. et al., 2009, ApJ, 701, 1076

Gou L., McClintock J. E., Steiner J. F., Narayan R., Cantrell A. G., Bailyn C. D., Orosz J. A., 2010, ApJ, 718, L122

Hawley J. F., Krolik J. H., 2006, ApJ, 641, 103

Hughes S. A., Blandford R. D., 2003, ApJ, 585, L101

Igumenshchev I. V., 2009, ApJ, 702, L72

Igumenshchev I. V., Narayan R., Abramowicz M. A., 2003a, ApJ, 592, 1042

Igumenshchev I. V., Narayan R., Abramowicz M. A., 2003b, ApJ, 592, 1042

Komissarov S. S., Barkov M. V., 2009, MNRAS, 397, 1153

Komissarov S. S., McKinney J. C., 2007, MNRAS, 377, L49

Komissarov S. S., Barkov M. V., Vlahakis N., Königl A., 2007, MNRAS, 380, 51

Krolik J. H., 1999, ApJ, 515, L73

Krolik J. H., Hawley J. F., 2002, ApJ, 573, 754

Krolik J. H., Hawley J. F., Hirose S., 2005, ApJ, 622, 1008

Li L., 2002, Phys. Rev. D, 65, 084047

Li L., Zimmerman E. R., Narayan R., McClintock J. E., 2005, ApJS, 157, 335

Liu J., McClintock J. E., Narayan R., Davis S. W., Orosz J. A., 2008, ApJ, 679, L37

MacDonald D. A., 1984, MNRAS, 211, 313

McClintock J. E., Shafee R., Narayan R., Remillard R. A., Davis S. W., Li L., 2006, ApJ, 652, 518

McClintock J. E., Narayan R., Gou L., Liu J., Penna R. F., Steiner J. F., 2009, in Comastri A., Angelini L., Cappi M., eds, AIP Conf. Proc. Vol. 1248, X-ray Astronomy 2009: Present Status, Multi-Wavelength Approach and Future Perspectives. Am. Inst. Phys., New York, p. 101

McKinney J. C., 2005, ApJ, 630, L5

McKinney J. C., 2006a, MNRAS, 367, 1797

McKinney J. C., 2006b, MNRAS, 368, 1561

McKinney J. C., Blandford R. D., 2009, MNRAS, 394, L126

McKinney J. C., Gammie C. F., 2004, ApJ, 611, 977

McKinney J. C., Narayan R., 2007a, MNRAS, 375, 513

McKinney J. C., Narayan R., 2007b, MNRAS, 375, 531

Meier D. L., 2001, ApJ, 548, L9

Mignone A., McKinney J. C., 2007, MNRAS, 378, 1118

Narayan R., Kato S., Honma F., 1997, ApJ, 476, 49

Narayan R., Igumenshchev I. V., Abramowicz M. A., 2003, PASJ, 55, L69

Narayan R., McClintock J. E., Shafee R., 2008, in Yuan Y.-F., Li X.-D., Lai D., eds, AIP Conf. Ser. Vol. 968, Astrophysics of Compact Objects. Am. Inst. Phys., New York, p. 265

Noble S. C., Krolik J. H., 2009, ApJ, 703, 964

Noble S. C., Gammie C. F., McKinney J. C., Del Zanna L., 2006, ApJ, 641, 626

Noble S. C., Krolik J. H., Hawley J. F., 2009, ApJ, 692, 411 (N09)

Noble S. C., Krolik J. H., Hawley J. F., 2010, ApJ, 711, 959 (N10)

Novikov I. D., Thorne K. S., 1973, in DeWitt C., DeWitt B. S., eds, Black Holes. Les astres occlus. Gordon and Breach, New York, p. 343 (NT)

Paczyński B., 2000, preprint (astro-ph/0004129)

Page D. N., Thorne K. S., 1974, ApJ, 191, 499

Papadopoulos P., Font J. A., 1998, Phys. Rev. D, 58, 024005

Popham R., Gammie C. F., 1998, ApJ, 504, 419

Remillard R. A., McClintock J. E., 2006, ARA&A, 44, 49

Reynolds C. S., Armitage P. J., 2001, ApJ, 561, L81

Reynolds C. S., Fabian A. C., 2008, ApJ, 675, 1048

Sano T., Inutsuka S., Turner N. J., Stone J. M., 2004, ApJ, 605, 321

Sądowski A., 2009, ApJS, 183, 171

Schnittman J. D., Krolik J. H., Hawley J. F., 2006, ApJ, 651, 1031

Shafee R., McClintock J. E., Narayan R., Davis S. W., Li L.-X., Remillard R. A., 2006, ApJ, 636, L113

Shafee R., McKinney J. C., Narayan R., Tchekhovskoy A., Gammie C. F., McClintock J. E., 2008a, ApJ, 687, L25 (S08)

Shafee R., Narayan R., McClintock J. E., 2008b, ApJ, 676, 549

Shakura N. I., Sunyaev R. A., 1973, A&A, 24, 337

Shapiro S. L., 2010, Phys. Rev. D, 81, 024019

Shapiro S. L., Teukolsky S. A., 1983, Black Holes, White Dwarfs, and Neutron Stars: The Physics of Compact Objects. Research supported by the National Science Foundation. Wiley-Interscience, New York, p. 663

Sorathia K. A., Reynolds C. S., Armitage P. J., 2010, ApJ, 712, 1241

Takahashi M., Nitta S., Tatematsu Y., Tomimatsu A., 1990, ApJ, 363, 206

Tchekhovskoy A., McKinney J. C., Narayan R., 2007, MNRAS, 379, 469

Tchekhovskoy A., McKinney J. C., Narayan R., 2008, MNRAS, 388, 551

Tchekhovskoy A., McKinney J. C., Narayan R., 2009a, ApJ, 699, 1789

Tchekhovskoy A., Narayan R., McKinney J. C., 2009b, New Astron., 15, 749

Tchekhovskoy A., Narayan R., McKinney J. C., 2010, ApJ, 711, 50

Thorne K. S., 1974, ApJ, 191, 507

Zhang S. N., Cui W., Chen W., 1997, ApJ, 482, L155

APPENDIX A: EXAMPLE SOLUTIONS AND SCALINGS FOR THE GAMMIE (1999) MODEL

Table A1 gives representative solutions for the Gammie (1999) model of a magnetized thin accretion flow. The columns correspond to the BH spin, a; the specific magnetic flux, Υ; the nominal efficiency, $\tilde{e}$; per cent deviation of $\tilde{e}$ from the NT value; the specific angular momentum, $\jmath$; per cent deviation of $\jmath$ from NT; and the normalized rate of change of the dimensionless BH spin, s (see equation 15). For $\Upsilon \lesssim 0.5$ and across all BH spins, the relative change in the specific angular momentum is less than 5 per cent and the relative change in the efficiency is less than 9 per cent. For small values of $\Upsilon \lesssim 1$, the deviations of $\jmath$ and $\tilde{e}$ from NT behave

Table A1. Thin magnetized inflow solutions.

$\frac{a}{M}$	Υ	$\tilde{e}$	$D[\tilde{e}]$	J	$D[J]$	s
0	0.1	0.0576	0.709	3.46	−0.172	3.46
0	0.2	0.0584	2.14	3.45	−0.52	3.45
0	0.3	0.0595	4.08	3.43	−0.991	3.43
0	0.5	0.0624	9.17	3.39	−2.23	3.39
0	1	0.0727	27.1	3.24	−6.57	3.24
0	1.5	0.0859	50.2	3.04	−12.2	3.04
0	6	0.19	232	1.51	−56.4	1.51
0.7	0.1	0.105	1.03	2.58	−0.286	1.33
0.7	0.2	0.107	3.07	2.56	−0.853	1.31
0.7	0.3	0.11	5.8	2.54	−1.61	1.3
0.7	0.5	0.117	12.8	2.49	−3.57	1.26
0.7	1	0.142	36.7	2.32	−10.2	1.12
0.7	1.5	0.172	66.3	2.11	−18.5	0.95
0.7	6	0.477	360	−0.00714	−100	−0.74
0.9	0.1	0.157	1.17	2.09	−0.386	0.576
0.9	0.2	0.161	3.37	2.08	−1.11	0.567
0.9	0.3	0.165	6.29	2.06	−2.07	0.555
0.9	0.5	0.177	13.7	2.01	−4.5	0.524
0.9	1	0.215	38.3	1.84	−12.6	0.423
0.9	1.5	0.262	68.3	1.63	−22.5	0.3
0.9	6	0.845	443	−0.958	−146	−1.24
0.98	0.1	0.236	0.949	1.68	−0.397	0.179
0.98	0.2	0.241	2.86	1.66	−1.2	0.174
0.98	0.3	0.246	5.36	1.64	−2.25	0.168
0.98	0.5	0.261	11.6	1.6	−4.9	0.152
0.98	1	0.309	32.2	1.45	−13.6	0.1
0.98	1.5	0.368	57.1	1.28	−24.1	0.0379
0.98	6	1.21	416	−1.27	−175	−0.862
0.998	0.1	0.319	−0.63	1.4	0.344	0.0374
0.998	0.2	0.327	2.02	1.38	−1.11	0.0342
0.998	0.3	0.332	3.66	1.36	−2	0.0322
0.998	0.5	0.345	7.73	1.33	−4.22	0.0273
0.998	1	0.388	20.9	1.23	−11.4	0.0113
0.998	1.5	0.439	37	1.11	−20.2	−0.00819
0.998	6	1.19	272	−0.675	−148	−0.292

systematically and one can derive simple fitting functions. For J we find

$$\log_{10}\left[-D[J]\right]$$

$$\approx 0.79 + 0.37(a/M) + 1.60\log_{10}\Upsilon \tag{A1}$$

$$\sim (4/5) + (1/3)(a/M) + (8/5)\log_{10}\Upsilon, \tag{A2}$$

with an L2 error norm of 0.7 per cent, 0.7 per cent, respectively, for the first and second relations, while for $\tilde{e}$ we find

$$\log_{10}\left[D[\tilde{e}]\right]$$

$$\approx 1.44 + 0.12(a/M) + 1.60\log_{10}\Upsilon \tag{A3}$$

$$\sim (3/2) + (1/10)(a/M) + (8/5)\log_{10}\Upsilon, \tag{A4}$$

with an L2 error norm of 0.9 per cent, 1 per cent, respectively, for the first and second relations. These results indicate that the deviations

from NT scale as $\Upsilon^{8/5}$ for $\Upsilon \lesssim 1$. For $\Upsilon \gtrsim 1$, the index on Υ depends on the spin parameter. In the span from $\Upsilon \sim 0.2$ to $\Upsilon \sim 1$, a linear fit across all BH spins gives $-D[J] \sim -1 + 11\Upsilon$ and $D[\tilde{e}] \sim -4 + 33\Upsilon$, which are rough, though reasonable looking, fits.

APPENDIX B: INFLOW EQUILIBRIUM TIME-SCALE IN THE NOVIKOV–THORNE MODEL

The radius out to which inflow equilibrium is achieved in a given time may be estimated by calculating the mean radial velocity v_r and then deriving from it a viscous time-scale $-r/v_r$.

When the flow has achieved a steady state, the accretion rate,

$$\dot{M} = -2\pi r \Sigma v_r \mathcal{D}^{1/2}, \tag{B1}$$

is a constant independent of time and position. Here, we derive an expression for v_r corresponding to the general relativistic NT thin disc model. In what follows, capital script letters denote standard functions of r and a (cf. equations 14 and 35 in Page & Thorne 1974) which appear as relativistic corrections in otherwise Newtonian expressions. They reduce to unity in the limit $r/M \to \infty$.

The vertically integrated surface density may be defined as $\Sigma = 2h\rho$, where h is the disc scaleheight and ρ is the rest-mass density at the midplane. In equilibrium, density is related to pressure by

$$\frac{dp}{dz} = \rho \times (\text{'acceleration of gravity'}) \tag{B2}$$

$$= \rho \frac{Mz}{r^3} \frac{\mathcal{B}^2 \mathcal{D} \mathcal{E}}{\mathcal{A}^2 \mathcal{C}}, \tag{B3}$$

the vertically integrated solution of which is

$$h = (p/\rho)^{1/2}/|\Omega| \mathcal{A}\mathcal{B}^{-1}\mathcal{C}^{1/2}\mathcal{D}^{-1/2}\mathcal{E}^{-1/2}. \tag{B4}$$

The pressure may be parametrized in terms of the viscous stress, $|t_{\hat{r}\hat{\phi}}| = \alpha p$, which is a known function of r and a:

$$W = 2h t_{\hat{r}\hat{\phi}} = \frac{\dot{M}}{2\pi}\Omega\frac{\mathcal{C}^{1/2}\mathcal{Q}}{\mathcal{B}\mathcal{D}}. \tag{B5}$$

The surface density is then

$$\Sigma = \frac{1}{2\pi}\frac{\dot{M}}{\alpha h^2|\Omega|}\mathcal{A}^2\mathcal{B}^{-3}\mathcal{C}^{3/2}\mathcal{D}^{-2}\mathcal{E}^{-1}\mathcal{Q}. \tag{B6}$$

Substituting this in equation (B1), the radial velocity is

$$v_r = -\alpha|h/r|^2|\Omega|r\mathcal{A}^{-2}\mathcal{B}^3\mathcal{C}^{-3/2}\mathcal{D}^{3/2}\mathcal{E}\mathcal{Q}^{-1}. \tag{B7}$$

This result is independent of the exact form of the pressure and opacity and so is valid in all regions of the disc. The inflow equilibrium time may be estimated as $t_{ie} \sim -2r/v_r$.

This paper has been typeset from a TₑX/LᴬTₑX file prepared by the author.